RARE CELL ENRICHMENT FROM BLOOD BY USING DIELECTROPHORESIS

A THESIS SUBMITTED TO
THE GRADUATE SCHOOL OF NATURAL AND APPLIED SCIENCES
OF
MIDDLE EAST TECHNICAL UNIVERSITY

BY

GÜRHAN ÖZKAYAR

IN PARTIAL FULFILLMENT OF THE REQUIREMENTS
FOR
THE DEGREE OF MASTER OF SCIENCE
IN
BIOMEDICAL ENGINEERING

SEPTEMBER 2015

Approval of the thesis:

RARE CELL ENRICHMENT FROM BLOOD BY USING DIELECTROPHORESIS

submitted by **GÜRHAN ÖZKAYAR** in partial fulfillment of the requirements for the degree of **Master of Science in Biomedical Engineering Department, Middle East Technical University** by,

Prof. Dr. Gülbin Dural Ünver
Dean, Graduate School of **Natural and Applied Sciences** _____

Prof. Dr. Hakan Işık Tarman
Head of Department, **Biomedical Engineering** _____

Prof. Dr. Haluk Külah
Supervisor, **Electrical and Electronics Eng. Dept., METU** _____

Dr. Ebru Özgür
Coadvisor, **MEMS Research and Application Center, METU** _____

Examining Committee Members:

Prof. Dr. Tayfun Akın
Electrical and Electronics Engineering Dept., METU _____

Prof. Dr. Haluk Külah
Electrical and Electronics Engineering Dept., METU _____

Prof. Dr. Nevzat Güneri Gencer
Electrical and Electronics Engineering Dept., METU _____

Prof. Dr. Ufuk Gündüz
Biology Dept., METU _____

Asst. Prof. Dr. Mahmud Yusuf Tanrıkulu
Electrical and Electronics Engineering Dept., Adana STU _____

Date: *07.09.2015*

I hereby declare that all information in this document has been obtained and presented in accordance with academic rules and ethical conduct. I also declare that, as required by these rules and conduct, I have fully cited and referenced all material and results that are not original to this work.

Name, Lastname: Gürhan Özkayar

Signature:

ABSTRACT

RARE CELL ENRICHMENT FROM BLOOD BY USING DIELECTROPHORESIS

Özkayar, Gürhan
M. S., Department of Biomedical Engineering
Supervisor: Prof. Dr. Haluk Külah

September 2015, 150 pages

Dielectrophoresis (DEP) is a technique used for separating particles with different sizes and/or dielectric properties. Fabrication of microelectrodes, thanks to MEMS technology, allows DEP to be applied in biomedical applications such as manipulation, separation, and enrichment of targeted cells from untargeted ones without any labeling. Especially, rare cell detection from blood occupies an important place in diagnostics of fatal diseases such as cancer. Circulating tumor cells (CTCs) that are shed into circulatory system has been considered as an important biomarker for the metastatic progression in cancer. Early detection of CTCs has the uttermost importance for the success of the therapy. However, it cannot be used as a diagnostic tool due to difficulties in detecting only a few

CTCs in milieu of billions of blood cells. The objective of this thesis is to develop a MEMS-based dielectrophoretic device for the enrichment of cancer cells from blood with a high throughput, sensitivity, and selectivity.

To achieve this goal, a wide (1000 μm), parylene-based microchannel with V-shaped planar microelectrodes arranged in parallel throughout the channel has been developed. Throughout the thesis, three generations of DEP devices with different electrode and microchannel geometries have been developed. The first and second generation devices contained two consecutive DEP areas, one for focusing of all cells towards the channel walls via negative DEP (nDEP) force, and the other for selective manipulation of red blood cells (RBCs), where their separation from cancer cells and redirection into the waste outlet take place. However, these devices could manipulate cells at low flow rates (up to 1 μl/min), which results in low throughput. To increase the throughput, electrode and channel geometries has been revised so that the cells are manipulated via positive DEP force (pDEP) and slide through the electrodes to the side channels. Also, parylene filters have been included to filter the RBCs due to their size difference, while keeping the large cancer cells inside the main channel. By this way, the flow rate could be increased up to 30 μl/min, and the working potential has been decreased from 20 V_{pp} to 10 V_{pp}. Fabricated 3rd generation DEP devices are capable of working with up to 6 million cells/ml cell concentrations including 5 million RBCs/ml and 1 million cancer cells/ml (K562 human leukemia cancer cell lines and MCF7 human breast adenoma cancer cell lines, separately). Cell enrichment factor for rare cells were calculated as 1.3, which means the desired rare cell percentage was increased to 1.3 fold at the output relative to the input. Further improvements in the design and operational conditions would increase enrichment ratio to the ultimate goal, which is enrichment of rare cells from whole blood of real cancer patients.

Keywords: Dielectrophoresis (DEP), rare cell enrichment, asymmetric planar electrodes, blood, and cell slide.

ÖZ

DİELEKTROFOREZ YÖNTEMİ İLE KANDAN ENDER HÜCRE ZENGİNLEŞTİRİLMESİ

Özkayar, Gürhan
Yüksek Lisans, Biyomedikal Mühendisliği Bölümü
Tez Yöneticisi: Prof. Dr. Haluk Külah

Eylül 2015, 150 sayfa

Dielektroforez, boyutları ve/veya dielektrik özellikleri farklı parçacıkları ayrıştırmakta kullanılan temel bir tekniktir. MEMS teknolojisi sayesinde üretilebilen mikroelektrotlar, hedeflenen hücrelerin etiketleme olmaksızın yönlendirilmesi, hedeflenmeyen hücrelerden ayrıştırılması ve zenginleştirilmesi gibi biyomedikal uygulamalarda dielektroforezin uygulanmasına olanak sağlar. Özellikle, kanser gibi ölümcül hastalıkların tanısında kandan ender hücre tespiti önemli bir yere sahiptir. Dolaşım sistemine yayılan gezici kanser hücreleri, kanserin metastatik ilerlemesinde önemli bir biyo-işaret olarak görülmektedir.Bu hücrelerin erken tespiti tedavinin başarısı açısından son derece önemlidir. Bununla birlikte, milyarlarca kan hücresi arasından sadece bir kaç adet gezici kanser

hücresinin tespitinin zorlukları nedeniyle, bir tanı aracı olarak kullanılamamaktadırlar. Bu tezin amacı, kandan kanser hücrelerinin zenginleştirilmesini yüksek verimlilikte, hassasiyette ve seçicilikte sağlayan bir MEMS tabanlı bir dielektroforetik cihaz yapımıdır.

Bu hedefe ulaşmak için, V-şekilli mikroelektrotların kanal boyunca parallel yerleştirildiği, 1000 μm genişliğinde olan, parilen temelli bir mikrokanal geliştirilmiştir.Tez süreci boyunca, farklı mikroelektrot ve kanal yapıları içeren üç cihaz nesli geliştirilmiştir. Birinci ve ikinci nesil cihazlar, ardışık iki DEF alanı içermekte ve bu alanlardan ilki negatif DEF kuvveti sayesinde tüm hücreleri duvarlara doğru iterken, diğeri sadece kırmızı kan hücrelerinin seçilip tekrar kanalın ortasına yönlendirilerek kanser hücrelerinden ayrılmasını sağlamakta ve atık çıkışına ilerlemelerini sağlamaktadır. Bununla birlikte, bu cihazlar 1μl/dak gibi düşük akış hızlarında çalışabilmişlerdir ve bu verimliliği düşürmüştür. Verimliliğin artırılması için elektrot ve kanal yapıları değiştirilerek, hücreler pozitif DEF kuvveti ile elektrotların üzerinde kayarak yan kanallara yönlendirilmişlerdir. Ayrıca, boyutlarının kanser hücrelerine oranla küçük olması nedeniyle alyuvarları geçiren, kanser hücrelerini ana kanalda tutan parilen filtreler oluşturulmuştur. Bu yöntemle akış hızı 30 μl/dak seviyesine kadar çıkarılmış olup, uygulanan gerilim 20 V_{pp} seviyelerinden 10 V_{pp} seviyelerine çekilmiştir. Üretilen üçüncü nesil DEF cihazları, beş milyonu alyuvar ve bir milyonu kanser hücresi (ayrı ayrı K562 ve MCF7 hücre hatları) olmak üzere, toplam altı milyon hücre/ml konsantrasyonu ile çalışabilme kapasitesine sahiptir. Ender hücreler için hücre zenginleştirme faktörü 1.3 olarak hesaplanmış olup, bu değer çıkıştan elde edilen ender hücre yüzdesinin girişe göre 1.3 kat artırıldığı anlamına gelmektedir. Zenginleştirme yüzdesinin iyileştirilmesi ve daha yüksek hücre konsantrasyonlarına ulaşılması, bu çalışmaya asıl hedef olan gerçek kanser hastalarının tam kanından ender hücre zenginleştirme konusunda öncülük edebilir.

Anahtar Kelimeler: Dielektroforez (DEF), ender hücre zenginleştirme, asimetrik yüzeysel elektrotlar, kan, ve hücre kayması.

To My Family and "Perim"

ACKNOWLEDGEMENTS

After holding a degree in biomedical engineering, it was an essential aim for me to join the grand MEMS family. Because of giving me this chance, I would like to thank to Prof. Dr. Tayfun Akın and Prof. Dr. Haluk Külah. I would also like to express my sincere gratitude to my thesis advisor, Prof. Dr. Haluk Külah for his support, optimism and positive reinforcement during my graduate study. Many thanks to my coadvisor, Dr. Ebru Özgür, for all her help and guidance during my thesis work. I am also grateful to Prof. Dr. Ufuk Gündüz for collaborating us with providing biological laboratory and cancer cell lines.

I would like to thank to my colleagues; Mrs. Yağmur Demircan Yalçın for her guidance and patience during almost every step of my work and Mr. Taylan Töral for helping and guiding me during the fabrication of my devices.

I am especially grateful to all my lab friends in the BioMEMS and PowerMEMS groups for being such nice officemates.

I would also like to thank all METU-MEMS Center staff for their kind helps in cleanroom especially to Mr. Orhan Akar for sharing his knowledge.

I am thankful to The Scientific and Technological Research Council of Turkey (TÜBİTAK) for supporting me financially in 111E194 project.

My special gratitude to my mother, Mrs. Bedriye Özkayar, my father, Mr. Orhan Özkayar, my brother, Dr. Özgür Özkayar, and sister-in-law, Dr. Nihal Özkayar, for their never ending belief in me for achieving all my dreams. Besides, many thanks to my one and only niece, Miss Çağla Özkayar for establishing me her hero.

Finally, I owe my deepest thanks to the keystone of my life, Ms. Parinaz Ashrafi for her unconditional support, marvelous love and having endless faith in me.

TABLE OF CONTENTS

LIST OF TABLES

TABLES

LIST OF FIGURES

FIGURES

CHAPTER 1

INTRODUCTION

Over the course of many years, the standard way to diagnose cancer was an open surgical biopsy [1]. Compared with surgical biopsies, which are applied on the original tissues, blood examination is less invasive and easier for routine screening analyses. In addition, rare cells, such as leukemic cells and circulating tumor cells (CTCs) are found in the peripheral blood of cancer patients. 90% of all cancer-related deaths are caused by cancer metastasis and the presence and quantity of rare cells are highly correlated with cancer metastasis. However, processing and analyzing rare cells from peripheral blood (~1 to 100 rare cells per 10^9 blood cells) is a challenge, because target cells are rare and blood has a complex nature. Thus, a significant enrichment step is needed for collecting rare cells in high-purity and viability for further analyses [2].

With the rapid progress of promising microfluidic technologies, much attention in the field of blood analysis has been directed to microfluidic devices due to their small scale, ease of fabrication, and high performance in controlling the blood microenvironment, and processing complex blood cells [2].

1.1 Microfluidics

Microfluidics is a technology characterized by the engineered manipulation of fluids at microscales, which improves diagnostics and biological research substantially. Developing technologies by the semiconductor industry and micro-

electro mechanical systems (MEMS) field make it possible to produce microscale devices, so fluids can be manipulated by these devices. These microscale devices are generally referred as miniaturized total analysis systems (μTASs) or lab-on-a-chip (LOC) technologies. The fluid phenomena which dominate liquids at microscale are measurably different from those that dominate at the macroscale and important concepts such as laminar flow, surface tension, and capillary forces should be evaluated according to microscale level [3].

Microfluidic platforms enable the miniaturization, integration, automation, and parallelization of biochemical assays in an easy and consistent manner. According to their dominating main liquid propulsion principle, microfluidic platforms can be divided into five groups: capillary, pressure driven, centrifugal, electrokinetic, and acoustic systems [4].

Most of the microfluidic processes on a LOC are electrokinetic processes and interfacial electrokinetic phenomena dominate these microscale transport processes [5]. Thus, electrokinetic systems are explained in more details below.

1.2 Electrokinetics

Electrically controlled dynamics of fluids and particles at microscales is a mesmerizing research area in microfluidic applications such as sorting of biomolecules [6].

Electric fields acting on electric charges or electric field gradients acting on electric dipoles control the microfluidic unit operations in electrokinetic platforms. The simple setup of electrokinetic systems consists microfluidic channels and electrodes. Depending on buffers and/or samples used, electrokinetic effects can be classified as electroosmosis, electrophoresis, and dielectrophoresis [4].

1.2.1 Electroosmosis

Electroosmosis (EO) is defined as electrically driven motion of bulk fluids [6]. The velocity of this motion is linearly proportional to the applied electric field,

and dependent on both the microchannel material and the fluid. A thin layer of ions is located near a wall exposed to a fluid and it is named as electrical double layer (Figure 1.1) [7].

An important application of the electroosmotic flow is micropumps. Traditional electroosmotic micropumps generally require the use of a high potential (>1 kV) and/or complex channel structures [8]. It was proven that these systems can also be driven at a low ac potential, since fluid is driven by the local electric field, not the voltage applied [9]**.** 290 μm/s pumping velocity and 26.1 μl/h flow rate was observed in 5 mM buffer solution with the 10 V_{pp} applied potential in the designed ac electrokinetic micropumping system [8].

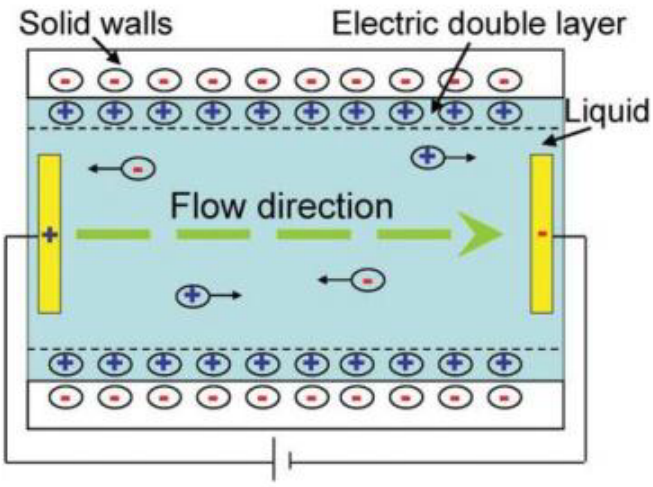

Figure 1.1 Depiction of traditional electroosmosic flow [8].

1.2.2 Electrophoresis

Electrophoresis (EP) is defined as the migration of charged ions in an electric field. EP requires the maintenance of a direct current (DC) or steady electric field in an electrolyte. This is traditionally accomplished through Faradaic reactions occurring at the interface where each electrode (anode and cathode) contacts the electrolyte [10]. Charged particles such as nucleic acids or proteins can be separated and the rate of the migration is related with the net charges on the

particles, mass and shape of the particles, properties of the supporting medium and strength of the electric field. EP can be categorized due to used supporting media such as paper electrophoresis, cellulose acetate membrane electrophoresis, gel electrophoresis (agarose gel, starch gel, and polyacrylamide gel) [11]. These systems do not lend themselves to straightforward miniaturization to ‘‘lab-on-a-chip’’ systems [10]. To overcome this problem, chip-based capillary electrophoresis (CE) systems are developed for separation of charged particles. Over the last 5–10 years there has been a strong push towards portable CE systems which has led to a variety of successful devices [12]. μChemLab™ instrument was developed as a CE system with a 2 cm x 2 cm low fluorescing fused-silica microseparation chip including 10 cm separation column. Figure 1.2 presents the CE system and separation chip.

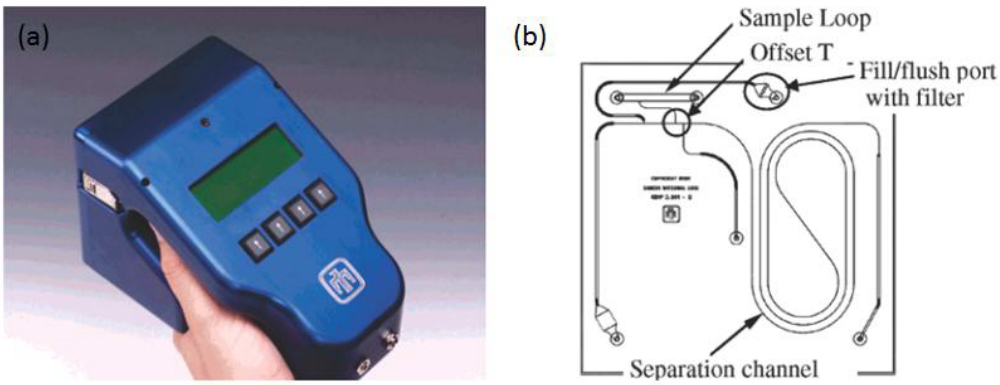

Figure 1.2 (a) μChemLab™ instrument (b) microseparation chip [13].

1.2.3 Dielectrophoresis

Whereas EP arises from the interaction of a particle’s charge and an electric field, DEP (in its simplest form) is due to the interaction of a particle’s dipole and the spatial gradient of the electric field. DEP can be used to characterize the polarizability aspect of electrical phenotype. The polarizability of cells is

primarily due to the cell wall (if present), membrane, and/or cytoplasmic electrical properties, depending on the applied field frequency [14].

A dielectrophoretic microsystem, consisting of a microchannel with an array of specially designed microelectrodes generates a high gradient electric field, thus can drive the selective movement of various particles, such as microbeads [15]–[19], yeasts [20], [21], bacteria [22], [23], viruses [24], [25], blood cells [26]–[29], and rare cells [30]–[49]. Because of the relevance with the thesis objectives, manipulations of blood cells and rare cells were investigated particularly.

1.2.3.1 Manipulation of Blood Cells

The possibility of focusing and separating blood cells based on their conductivity and shape characteristics has a great potential in studying fundamental cell properties as well as in the medical diagnostics field [26].

The motion of a suspension of erythrocytes (RBCs) in response to a high-frequency alternating current (AC) field in a microfluidic device was examined with parallel and orthogonal electrode configurations. Pearl chain formation occurs rapidly after the RBCs are focused by electrode repulsion in both configurations [26]. Figure 1.3 shows the device schematic and the frequency dependence of aggregation is quantified for human blood cells.

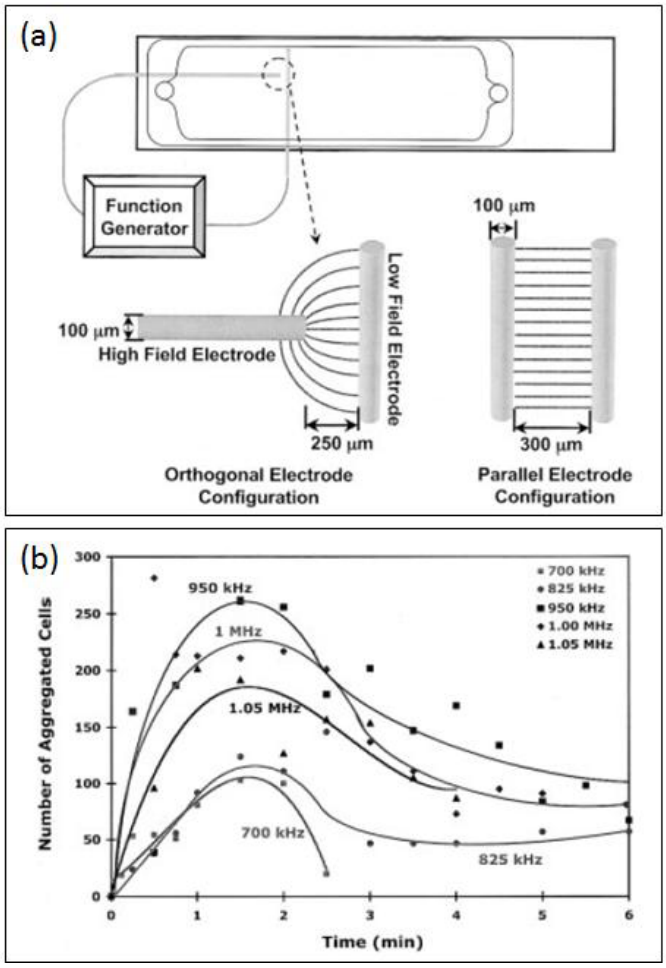

Figure 1.3 (a) Microchip schematic and (b) frequency dependence of aggregation of RBCs [26].

Gordon *et al*. used DEP for the analysis and discrimination of RBC starvation ages. The research was based on bovine RBCs and their crossover frequency changes due to glutaraldehyde concentration during starvation ages. It is known that glutaraldehyde addition to the cells removes positive amino groups which are found on the surface of the cells and destroys lipid the membrane. Crosslinking of the membrane and interior proteins produce a polyelectrolyte network to enhance the stability of the cells. [27]. For the utilizing the pDEP and nDEP forces on RBCs, quadrupole electrode array was chosen and the cells were observed in their different starvation ages (1 week, 2 weeks, and 4 weeks) as shown in Figure 1.4.

The square dots illustrate the 1 week starvation age, circular dots illustrate the 2 weeks starvation age, and triangular dots illustrate the 4 weeks starvation age of RBCs as shown in Figure 1.4b. The glutaraldehyde concentration differences do not cause any important changes in the low frequency cof of RBCs with different starvation ages, but an increase can be seen in the high frequency cof intervals of RBCs at the same starvation ages. According to Gordon *et al*. electrical properties of cells can be changed in different starvation ages with the treatment of glutaraldehyde as a result of crosslinking of the membrane and interior proteins of the cells.

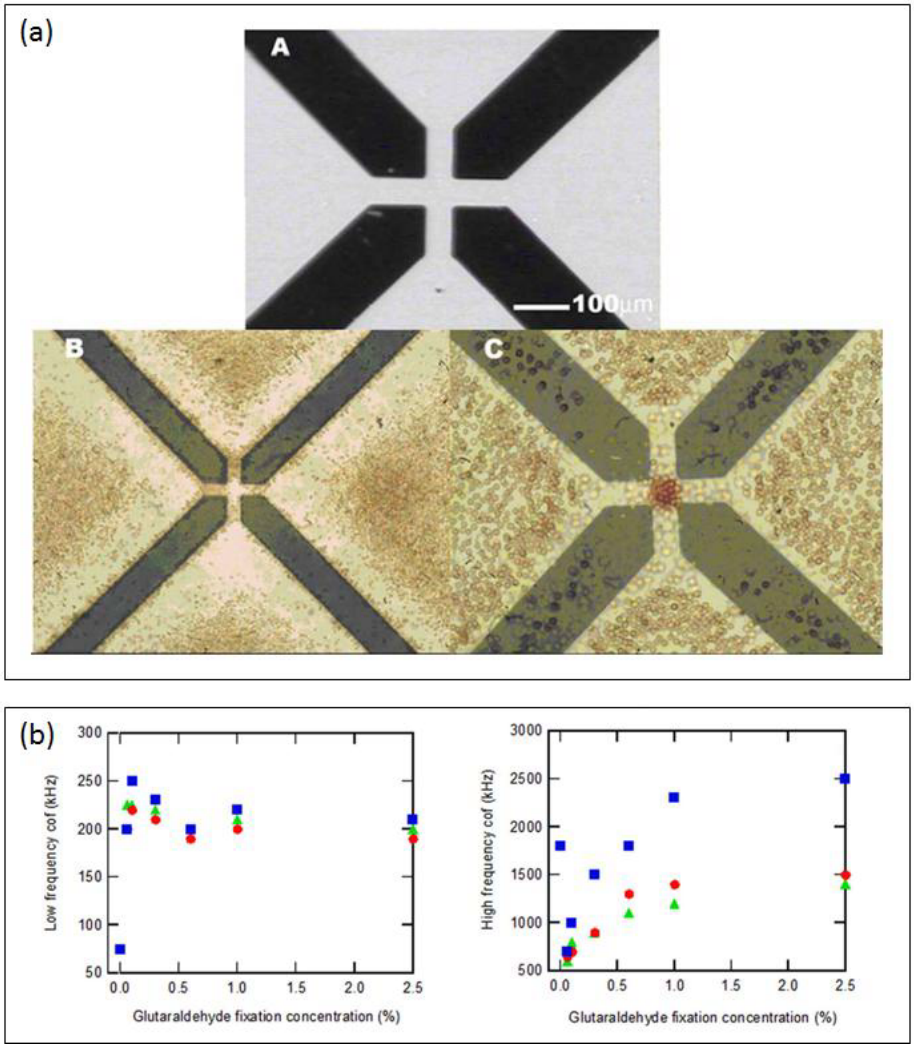

Figure 1.4 (a) Fabricated quadrupole electrodes and pDEP & nDEP responses and, (b) crossover frequency changes due to different starvation ages [27].

Blood serum analyses are crucial for diagnosing various diseases and blood serum has unique physical and chemical properties compared with blood cells. Thus, blood serum and blood cells can be separated from each other in dielectrophoretic applications (Figure 1.5) [28].

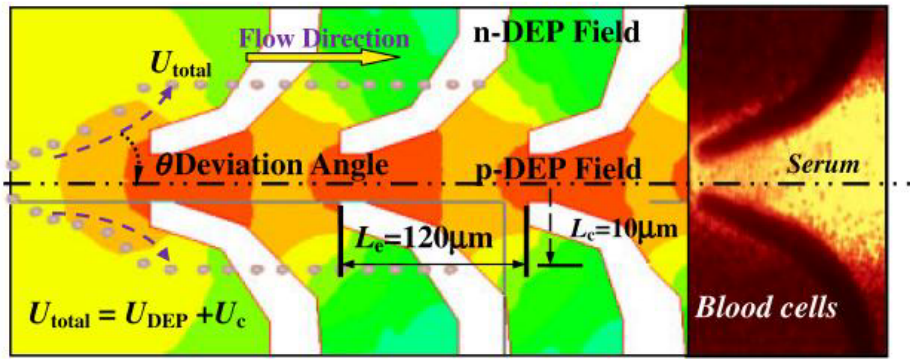

Figure 1.5 Electrode configuration and experimental results for blood serum and blood cell seperation [28].

Due to the need for high-purity, low-stress platelet separation technology, purification of platelet rich plasma (PRP) can be performed to eliminate red and white blood cells using dielectrophoretic and flow-induced shear force (Figure 1.6) [29].

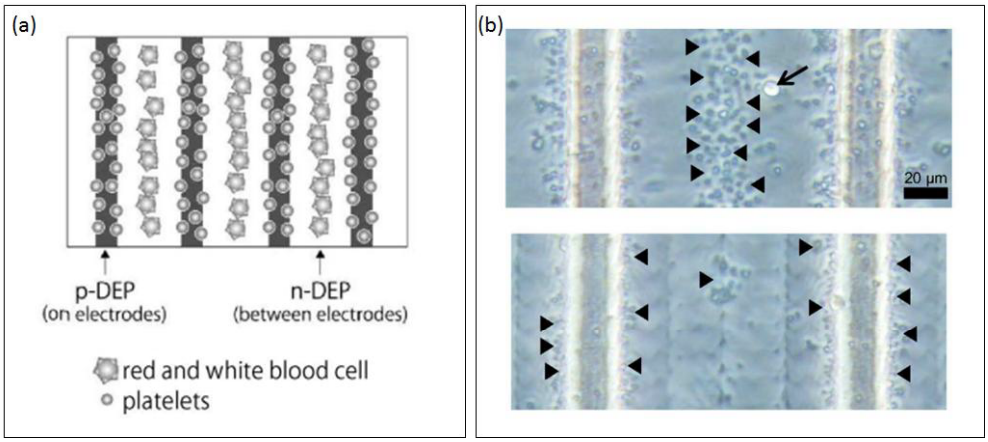

Figure 1.6 (a) Electrode configuration, and (b) applying 20 V_{pp} & 75 kHz and 20 V_{pp} & 100 kHz for platelets, respectively. Vector arrow indicates a blood cell and arrowheads indicate platelets [29].

1.2.3.2 Manipulation of Rare Cells

For early cancer detection and monitoring the progress of treatment, it is essential to isolate cancer cells from blood cells. Due to differences in size and dielectric properties of cancer cells, DEP can be used to isolate cancer cells from blood cells [30]. DEP has been used for the manipulation and isolation of several rare cell types including human leukemia cells [31]–[34], human breast cancer cells [35]–[41], cervical carcinoma cells from red blood cells [42], human oral squamous cell carcinoma cells from human HPV-16 transformed keratinocyte cells [43], human breast cancer cells from normal T-lymphocytes [44], human colon cancer cells from red blood cells [45], prostate cancer cells from colorectal cancer cells [46], malaria infected RBCs from healthy RBCs [47], [48], and human mesenchymal stem cells (hMSC) [49].

Live human leukemia cells can be selectively isolated from dead cells utilizing their electrical signatures (Figure 1.7) [33]. Because of no contact between electrodes and the medium, problems including contamination, electrochemical effects, bubble formation, and the harmful effects of joule heating is prevented [50].

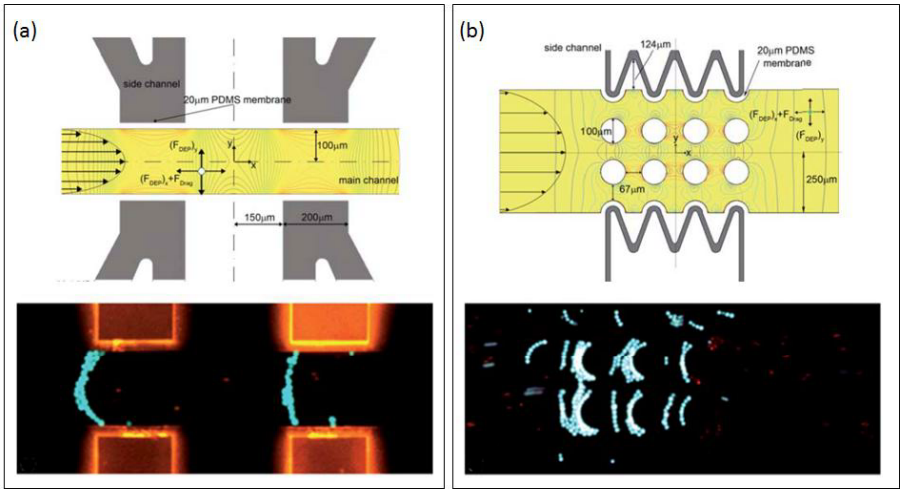

Figure 1.7 (a) cDEP device1 schematic and experimental result with cell trapping at $V_1 = V_2 = 100\ V_{rms}$ at 152 kHz and $V_3 = V_4$ = Ground (b) cDEP device2 schematic and experimental result with cell trapping at $V_1 = 40\ V_{rms}$ at 500 kHz and V_2 = Ground [33].

Besides the separation of cancer cells from non-cancer ones, DEP can be used to separate differentiated cancer cells from each other. Demircan *et al.* utilized DEP for separation of multidrug resistant cancer cells and sensitive cancer cells, on a continuous flow microfluidic channel with 3D electrodes. Trapping of K562AR cells on the electrodes were observed in a medium with flow rate of 6.67 µl/min (Figure 1.8) [34].

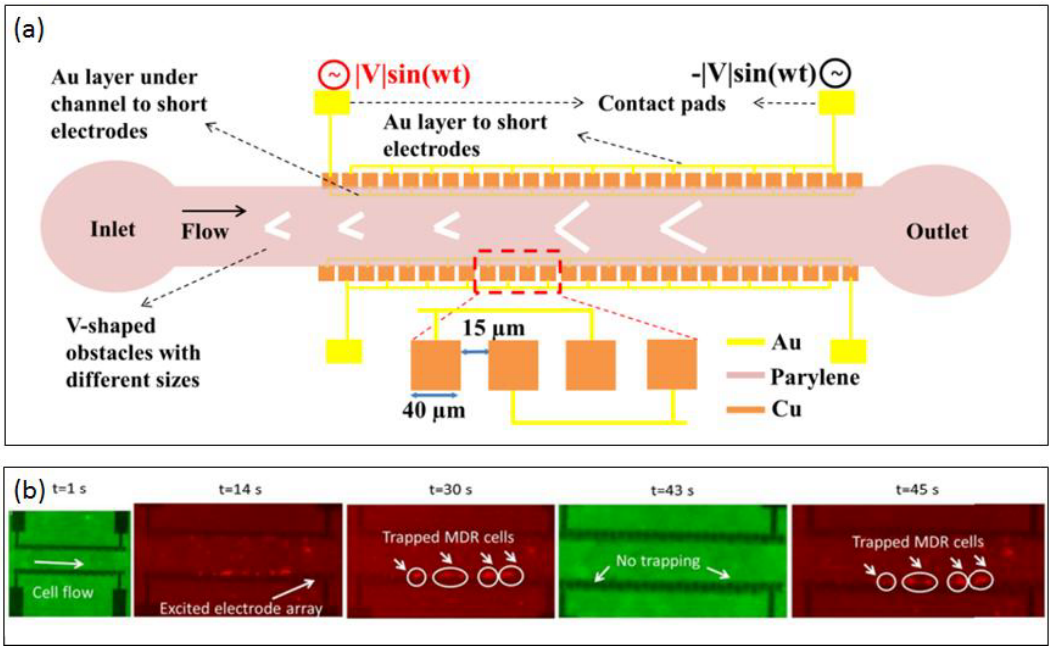

Figure 1.8 (a) Device schematic, (b) experimental results for sensitive K562 & K562AR cells at 48.64 MHz, V = 9 V_{pp} [34].

For the rapid isolation of HeLa cells from RBCs, a microdevice including circular microelectrodes was fabricated and tested. It was shown that HeLa cells were selectively concentrated at the center pair of microelectrodes from RBCs with a recovery rate of around 64.5% (Figure 1.9) [42].

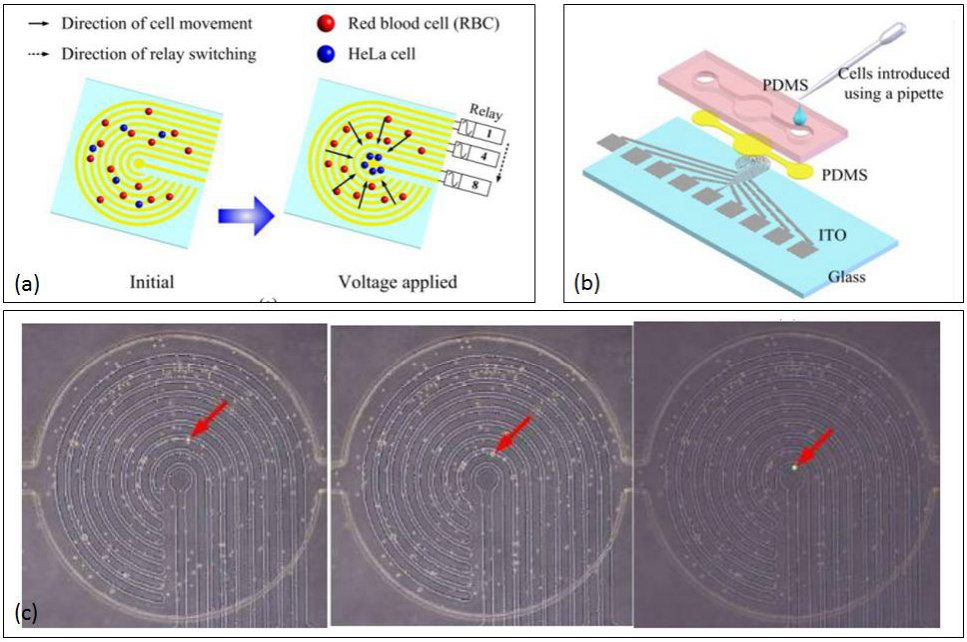

Figure 1.9 (a) Circular electrodes and cell movements schematic, (b) Device schematic (c) experimental results for HeLa cells and RBCs at 1 MHz, V = 16 V_{pp} [42].

Another dielectrophoretic cell separation device was made to fractionate cells according to their cell cycle phases. MDA-MB-231 cells in two different cell cycle phases (G_1/S and G_2/M) were applied to the device and separation was done at 20 V_{pp} & 800 kHz as shown in Figure 1.10 [39].

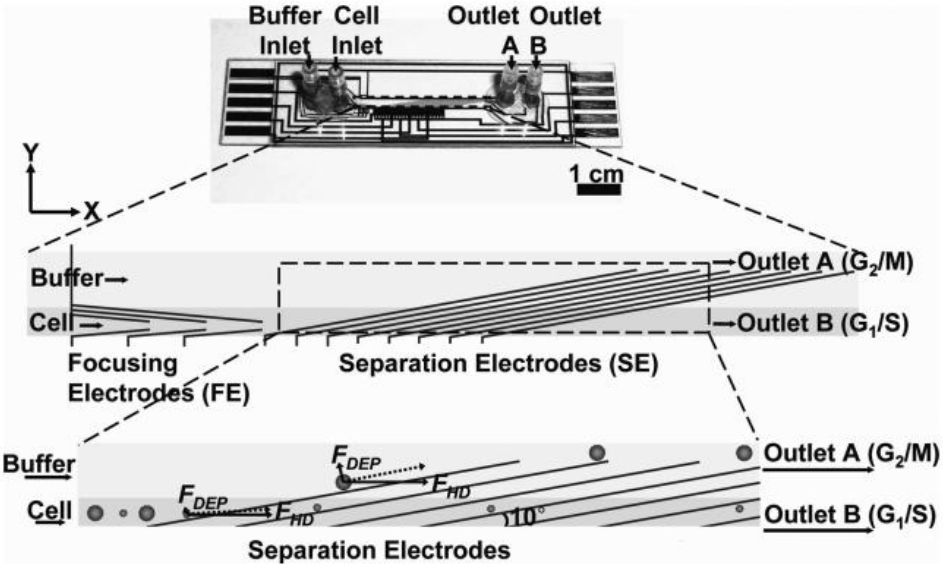

Figure 1.10 The physics of separation for cells in difference phases in their cell cycle [39].

DEP was used to separate prostate cancer cells from colorectal cancer cells, which have the same sizes and shapes. 12 V_{pp} and 2.5 MHz were applied to both cell types and prostate cancer cells (LNCaP) were manipulated under nDEP, but no manipulation was observed on colorectal cancer cells (HCT116). Enrichment factor was calculated as 96% at the flow rates less than 0.4 µl/min (Figure 1.11) [46].

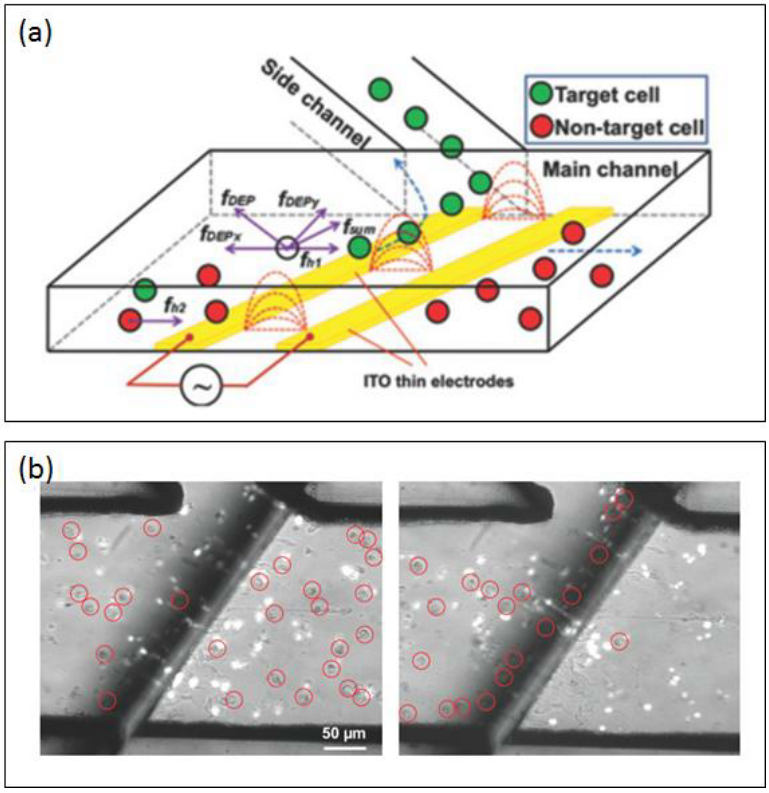

Figure 1.11 (a) Device schematic and (b) experimental results for nDEP on prostate cancer cells, passive electrodes and active electrodes, respectively [46].

Gascoyne *et al.* showed that DEP can be used for the detection and isolation of malarial RBCs from healthy ones. Plasmodium falciparum-infected red cells were used and investigated in mixtures with healthy RBCs and they exhibit a non-linear DEP crossover frequency response to increasing cell suspension conductivity, where healthy RBCs exhibit a linear response as shown in Figure 1.12. It was seen that transmembrane conductances of the infected RBCs were very high in comparison to healthy RBCs because of having modifiable pores on their plasma membranes. Permeation pathways begin to appear about 6h after infection of the RBCs and parasites synthesize protein channels on the plasma membrane of RBCs. Thus, transport of wide range of solutes into RBCs occurs and this changes the ion balance of the infected RBCs. Because of these differences,

dielectrophoretic responses of the infected RBCs differ from healthy ones and isolation can be done by DEP [47].

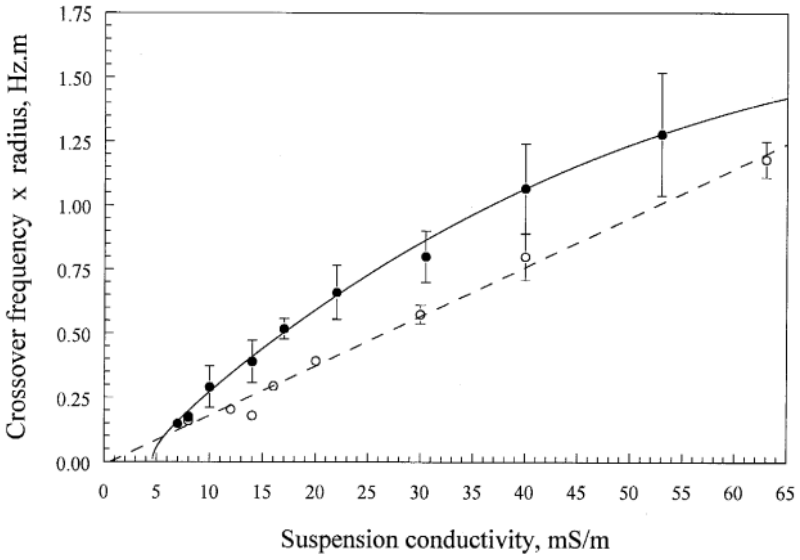

Figure 1.12 Dielectrophoretic crossover frequency characteristics of healthy RBCs and malarial RBCs [47].

1.3 Research Objectives and Thesis Organization

Especially in the early stages of cancer, only a few tumor cells are present in blood (1-100 cancer cells/$5x10^9$ blood cell/ml blood). For every rare tumor cell in blood there are almost billion more RBCs with it [51]. Thus, enrichment of rare cells is crucial before detection.

The primary research objective of this thesis is to develop a MEMS-based DEP device for rare cell enrichment from blood with high selectivity, sensitivity, and throughput.

To achieve this objective, following studies are aimed:

- Designing a microchannel, which satisfies dielectrophoretic manipulation of different cell types according to their dielectric properties. The system should operate without any hydrodynamic focusing and labeling.

- Dielectric modeling of RBCs and rare cells (K562 human leukemia cells and MCF7 human breast adenocarcinoma cells) using MATLAB, according to their dielectric properties reported in literature.
- Hydrodynamic and electrical analysis of the design with COMSOL software utilizing finite element model (FEM) simulations.
- Development of the fabrication flow and fabrication of the DEP devices.
- Testing of DEP devices with RBC and rare cells mixtures.
- Cell counting and calculating the enrichment factor of the DEP devices.

Thesis has been organized in six chapters as follows:

Chapter 2 provides the necessary background information and significant analysis parameters about DEP in microfluidics. Moreover, literature survey for applications of DEP for particle/cell manipulation is given.

Chapter 3 presents the dielectric properties of cells, including dielectric modeling techniques, dielectric modeling of red blood cells, K562 cancer cells and MCF7 cancer cells.

Chapter 4 includes the design and FEM simulations of the DEP devices with detailed structural explanations.

Chapter 5 presents the microfabrication process of the DEP devices.

In chapter 6, experimental analyses of the DEP devices are presented. The performances of the devices are assessed by applying the K562 cancer cell lines, MCF7 cancer cell lines and red blood cells, and analyzing their responses at different frequencies. In addition, rare cell enrichment factor is calculated and presented for the last generation devices.

Lastly, chapter 7 presents thesis conclusion and offers some recommendations for the further research.

CHAPTER 2

THEORY OF DIELECTROPHORESIS

2.1 Dielectrophoresis

In 1951, Pohl *et al.* introduced the term dielectrophoresis (DEP) for the first time and defined this effect as "the motion of suspensoid particles relative to that of the solvent resulting from polarization forces produced by an inhomogeneous electric field". The origin of the DEP is the Greek word *phorein*, an effect where a particle is carried as a result of its dielectric properties. [52]. First DEP-activated systems were developed by Pohl using tungsten wires and applying them to remove carbon-black fillers from polyvinyl chloride samples. Around 10 kV level voltages were needed to generate electric fields for manipulating target objects because of the large scale of the system [53]. After micro-scale electrodes were started to be used as nonuniform electric field generators, voltages which were used in the systems lowered and new opportunities were opened for DEP in biomedical microfluidic systems [54].

DEP force is determined by the magnitude and polarity of the charges induced on a particle by the applied field [55].

The DEP force is responsible for motion of polarizable particles, which is defined as below:

$$F_{DEP} = (P.\nabla)E \tag{2.1}$$

The dipole moment depends on the geometry of particle and for a homogeneous sphere is defined as:

$$P = 4\pi r^3 \varepsilon_m f_{CM} E \tag{2.2}$$

where r is radius of the particle, ε_m is the absolute permittivity of the surrounding medium which is defined as $\varepsilon_0 \varepsilon_r$ (ε_0 =8.85x10^{-12} F/m is the permittivity of the vacuum and ε_r is dielectric constant of the medium), f_{CM} is a complex variable known as Clausius-Mossotti factor related to the effective polarizability of the particle, and E is the amplitude (rms) of the electric field. Combining equations (2.1) and (2.2) gives the time-averaged DEP force applied on a spherical particle as:

$$F_{DEP} = 2\pi\varepsilon_0\varepsilon_m r^3 Re(f_{CM})\ \nabla E_{rms}^2\ +\ 4\pi\varepsilon_0\varepsilon_m r^3 Im(f_{CM}) \Sigma_{x,y,z}\ E_{rms}^2\ \nabla\varphi \tag{2.3}$$

This equation includes two independent terms for DEP force. First term is called as *classical DEP force* which is proportional to the real part of the f_{CM} and spatial nonuniformity of electric field magnitude. Second term is called *travelling wave DEP force* which is proportional to the imaginary part of the f_{CM} and spatial nonuniformity of the phase component. ∇ represents the gradient operator for electric field.

The expression for the time-average DEP force (acting on a spherical particle) is:

$$F_{DEP} = 2\pi\varepsilon_m r^3 Re(f_{CM})(\nabla E^2) \tag{2.4}$$

Clausius-Mossotti factor is represented as:

$$f_{CM} = \left(\frac{\varepsilon_p - \varepsilon_m}{\varepsilon_p + 2\varepsilon_m}\right) \tag{2.5}$$

The term f_{CM} denotes the real component of the function of complex permittivities within the parentheses. This term may vary between -0.5 and +1, determined by the properties of the medium and the moving particle. If this is positive, the force exerted upon the particle will be positive and the particle will move towards areas of high electric field gradient - positive dielectrophoresis (pDEP). If this is negative, the force exerted upon the particle will also be negative, and the particle

will move towards areas of lowest electric field gradient - negative dielectrophoresis (nDEP).

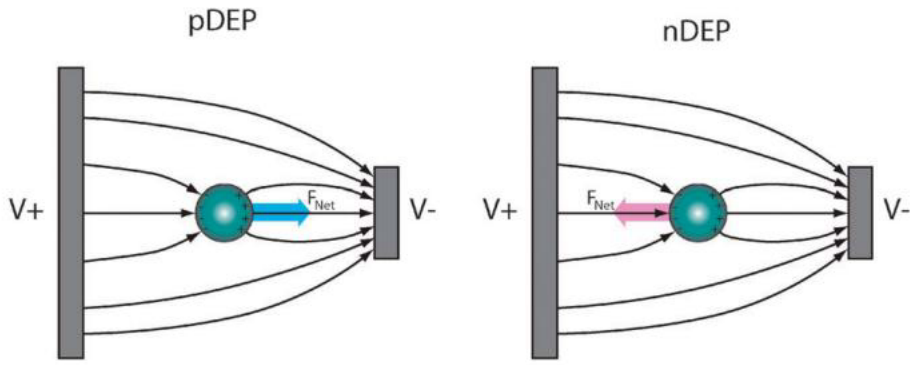

Figure 2.1 Positive and negative DEP effects on a polarizable particle [56].

From equations (2.4) and (2.5), it can be understood that:

- The DEP force is zero if the field is uniform (i.e., for $\nabla E=0$).
- If particle radius gets larger, then the DEP force acting on the particle increases when the other parameters remain constant.
- The induced dipole moment depends on whether the particle's permittivity is greater or less than that of the medium.
- Square of the applied electric field gradient acts on the DEP force, so that DEP can be observed using either dc or ac field.
- $(E\cdot\nabla E)$ with a factor of 10^{12} V^2 / m^3 can induce a significant DEP force on biological cells, thus the electrode geometry in the design is important to reach this level [52].

2.2 Microscale Electrode Materials for DEP Devices

In DEP, the microelectrodes define the nonuniform electric field distribution and the subsequent force field map, thus it is crucial to decide on the appropriate material for microelectrodes [57].

2.2.1 Metal Microelectrodes

Metal microelectrodes are preferred to generate electric fields by wide majority in BioMEMS applications [58]. Metals such as Gold (Au), Titanium (Ti), Chromium (Cr), Platinum (Pt), Silver (Ag), Copper (Cu), Nickel (Ni), Aluminum (Al), are generally chosen as microelectrode materials, because of having high electrical conductivities and planar and 3D microelectrode configurations can be fabricated with techniques such as sputtering [59], [60], [61] evaporation [62], [63], [64], electroplating [34], [65] and inkjet printing [66], [67].

2.2.2 Silicon Microelectrodes

Microelectrodes made of silicon ensure relatively low-cost and simple fabrication in comparison to metal microelectrodes. Besides, silicon microelectrodes can be oxygenated into SiO_2. Thus, microelectrodes are insulated from the solution and possible cell damages caused by direct contact between cells and microelectrodes can be avoided [68].

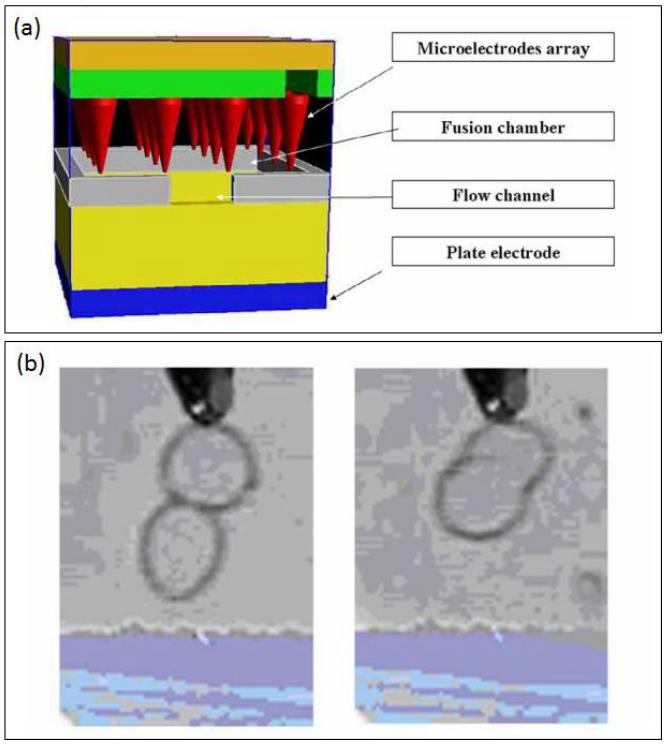

Figure 2.2 (a) Device schematic and (b) cell trapping and fusion on the tips of the microelectrodes [68].

Silicon microelectrodes can be fabricated using DRIE process through a silicon oxide mask on thin heavy doped silicon wafer which is anodically bonded to the glass substrate. After DRIE, glass substrate can be wet etched from bottom. Electrical contacts for silicon microelectrodes are provided with the metallization of the bottom glass wafer [69]. Figure 2.3 presents the device schematic and experimental results of the system.

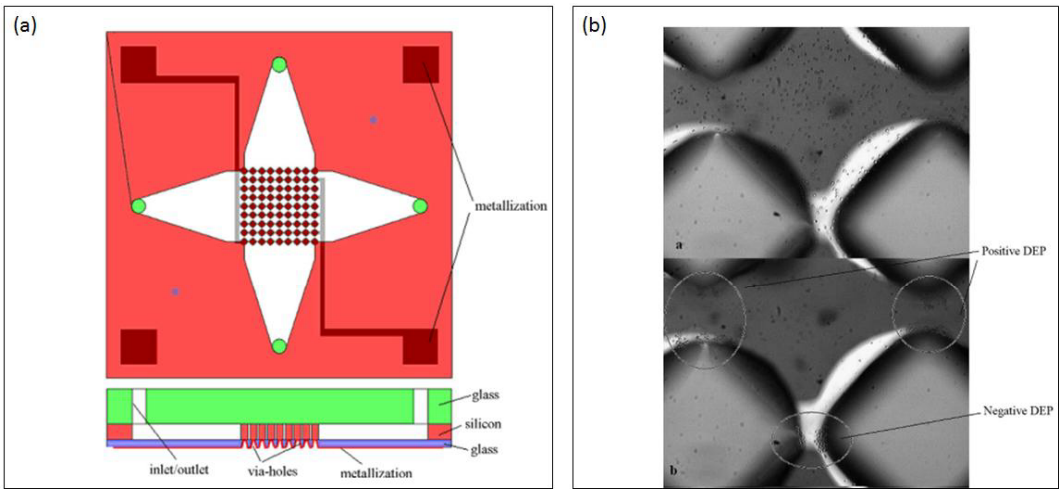

Figure 2.3 (a) Device schematic having silicon microelectrodes (b) experimental results on live and dead cells [69].

2.2.3 Carbon Microelectrodes

Carbon is very inert to most solvents and electrolytes, has excellent biocompatibility and its electrochemical stability is wider than gold and platinum [70].

Carbon microelectrodes only require polymer photolithography and heat treatment, thus fabrication of these microelectrode types are relatively simple and inexpensive in comparison to metal microelectrodes [71]. Carbon electrode structures are shown in Figure 2.4.

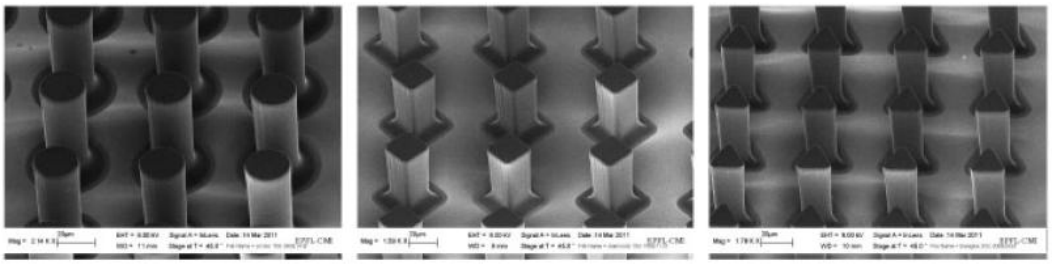

Figure 2.4 SEM images of carbon electrode examples [72].

Even in nanoscale, fabricated carbon nanotube electrodes apply relatively low trapping voltages and still high enough field gradients for trapping nanoscale objects can be achieved [73]. A device schematic and the results of the applied different frequencies on the electrodes are shown in Figure 2.5.

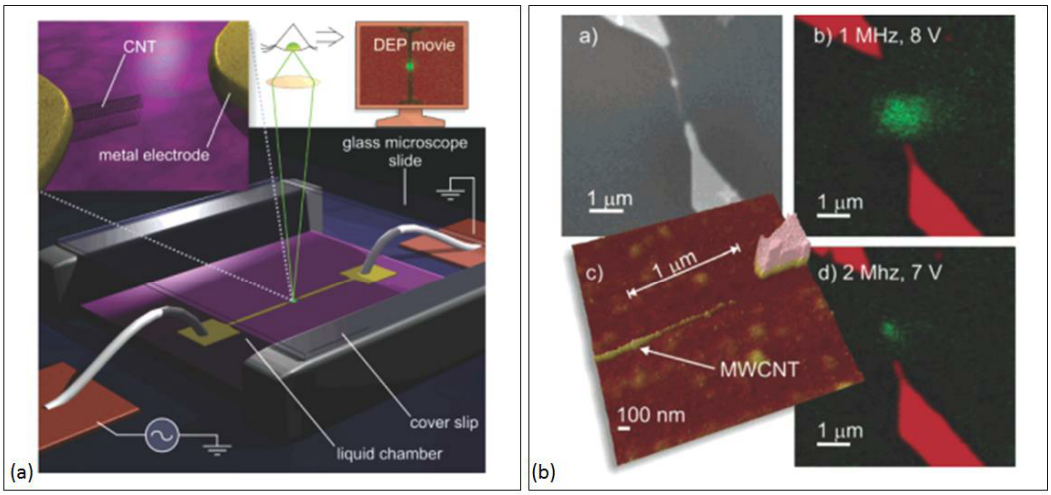

Figure 2.5 (a) Device schematic and (b) SEM & AFM images of carbon nanotube electrodes and experimental results for DNA trapping in different frequencies and voltages [73].

2.2.4 Polymer-based Microelectrodes

Polymer based microelectrodes are used in microparticle manipulations because of having wider range of electrode shapes and topologies. Electrodeposited polypyrrole (PPy) which is a conductive electroactive polymer can be used as microelectrode and produced with electropolymerization technique as shown in Figure 2.6 [70].

Entrapment of polystyrene beads (5 μm, 2 μm and 1 μm) was proven by using electrodeposited polypyrrole (PPy). 6 V_{pp} and 500 Hz was applied to induce DEP in the beads [74].

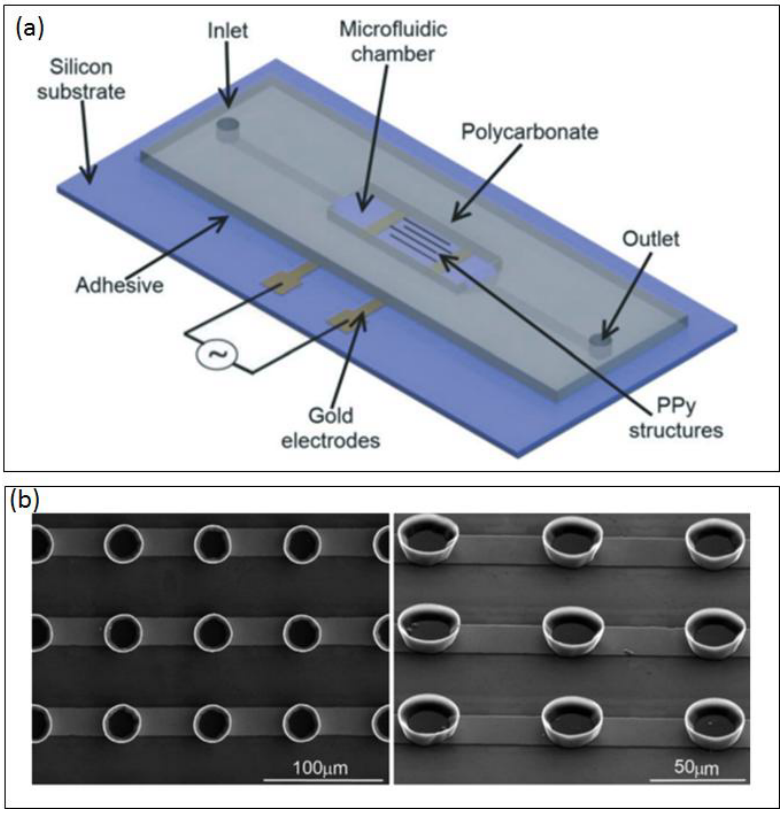

Figure 2.6 (a) Device schematic and (b) SEM images of 3D polymer-based electrodes [70].

PDMS can be made conductive by adding Ag. Composite AgPDMS electrodes embedded to the sidewalls of the microchannel were designed and fabricated to separate microparticles with diameters 0.5 μm and 5 μm as shown in Figure 2.7 [75].

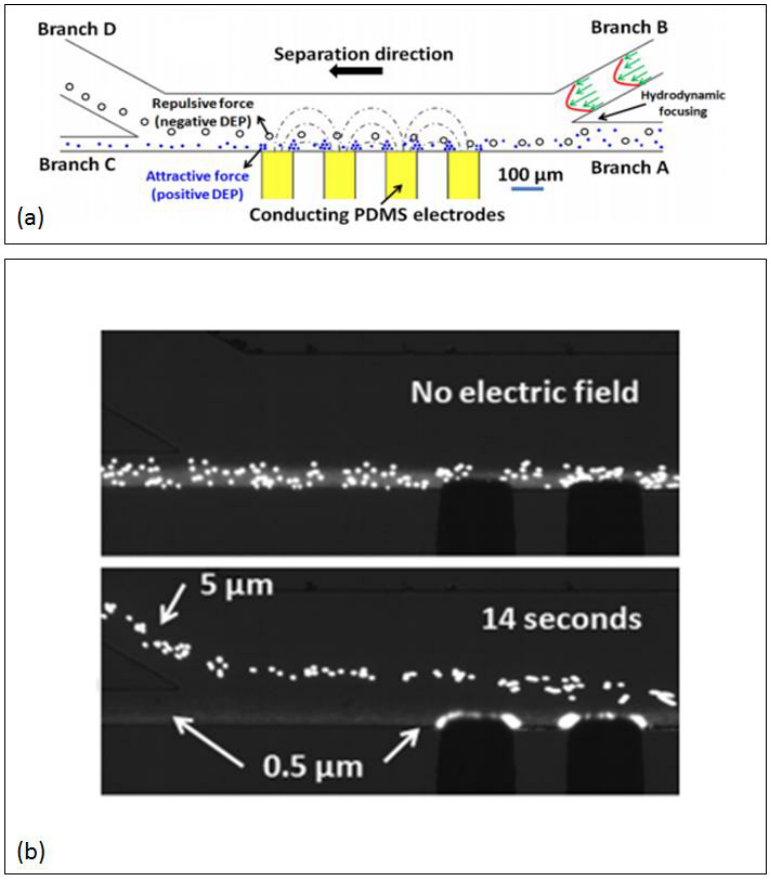

Figure 2.7 (a) Device schematic of a device with conductive AgPDMS microelectrodes and (b) experimental results for different sized microparticles at 30 V & 1 MHz [75].

2.2.5 Liquid Microelectrodes

Liquid electrodes avoid the real estate loss due to reservoirs containing macroscopic electrodes, allowing for potentially massive integration on chip. The term ‘‘liquid electrode’’ refers to a vertical equipotential surface located at the junction of the main and access channels [58].

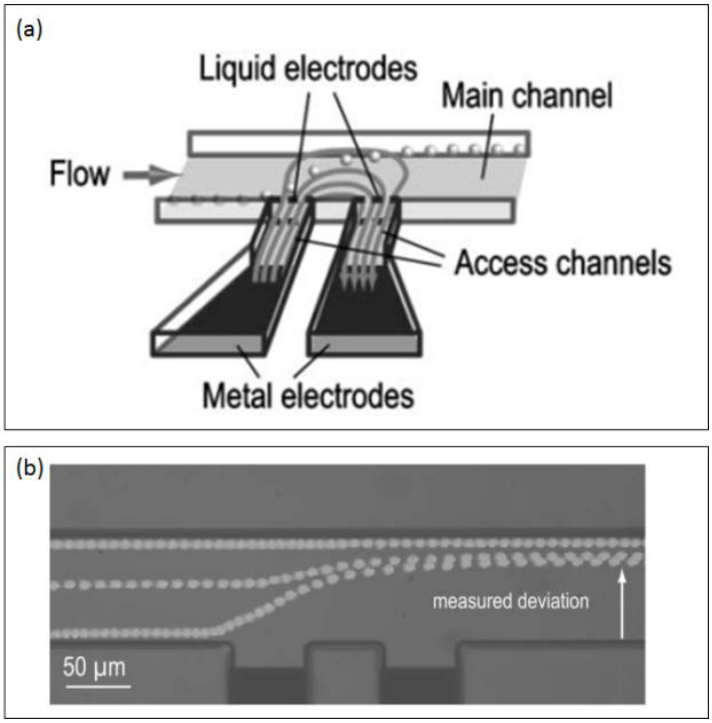

Figure 2.8 (a) Device schematic and (b) experimental results of manipulation of beads via liquid electrode implemented microfiluidic DEP device [58].

According to another study, liquid electrode concept had large metal electrodes which were situated in lateral chambers. The electric field was then conducted to the main microchannel by narrow access channels as shown in Figure 2.9 [76].

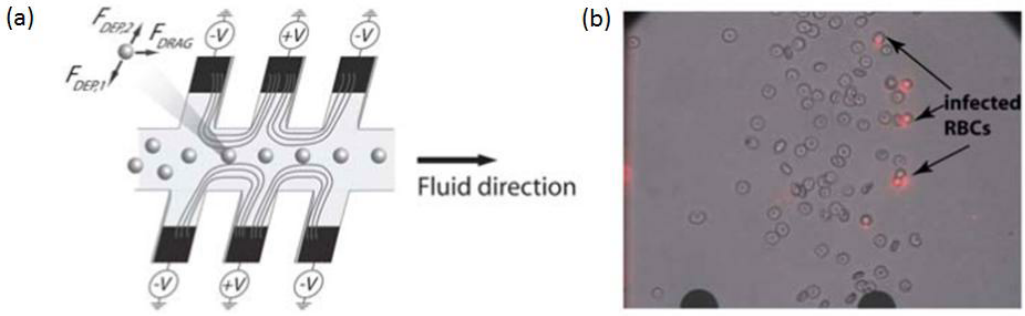

Figure 2.9 (a) Device schematic of DEP device with liquid electrodes and (b) experimental results for healthy and infected RBCs [76].

Mercury droplets can be used as liquid electrodes in the side channels of microchannels. Particles in the main microchannel can be manipulated by these droplets which are controlled by syringe pumps when activated. Yeast cells were manipulated by this method with applying voltages between 100 V – 800 V and frequencies between 1 kHz - 1 MHz as shown in Figure 2.10 [77].

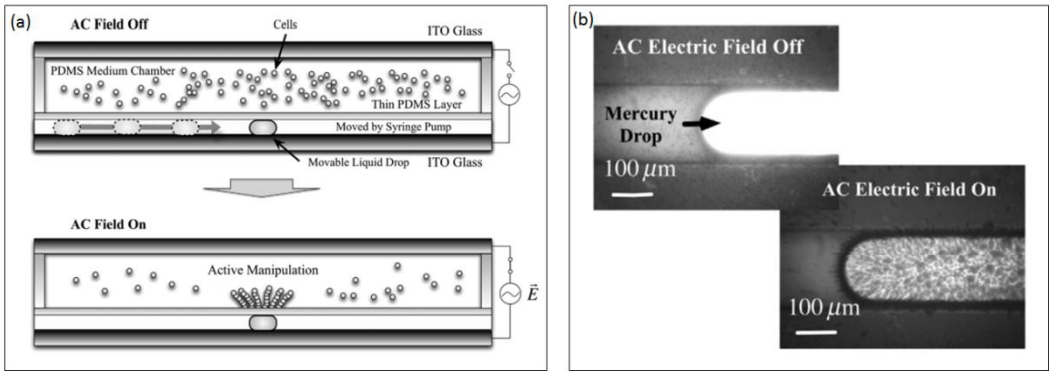

Figure 2.10 (a) Microchannel schematic of a DEP device with liquid mercury electrodes and (b) liquid electrode activation results [77].

2.3 Microscale Electrode Configurations Used for DEP Devices

To be able to produce desired nonuniform electric field in dielectrophoretic systems, decision of the most appropriate microelectrode configuration is essential. Many microelectrode configurations were designed and tested till now and can be divided into two main categories as planar microelectrodes and 3D microelectrodes.

2.3.1 Planar Microelectrodes

Planar electrodes are generally patterned at the bottom of the microchannels [78]. Some of the studied planar microelectrode configurations are interdigitated [79], oblique [80], castellated [81], spiral [82] and dot type [78] microelectrodes.

Interdigitated microelectrodes (Figure 2.11a) are activated with sinusoidal voltages having 180° phase difference and the positioned in arrays. Strong electric fields are formed on the edges of the electrodes and weak electric fields occur at interior parts of the electrodes.

Oblique configuration (Figure 2.11b) has two opposite electrodes activated with 180 phase difference and the straight arms of these electrodes incline at small angles. The tips of these straight arms are close to opposite straight arms and have the strong electric field. Other regions have weak electric fields in comparison to the tips.

Castellated microelectrode configuration (Figure 2.11c) consists of opposite castellation arrays and these arrays are activated with sinusoidal voltages having 180° phase difference. Strong electric fields occur at the sharp corners of the opposite arrays and weak electric fields occur between opposite electrode pairs.

Spiral configuration (Figure 2.11d) for microelectrodes is designed for manipulation of particles and cells selectively moving to either the center or periphery of the array.

Dot type microelectrode configuration (Figure 2.11e) is used for cell trapping and isolation. The electric field is higher at the dot edges than the dot centers. The electric field strength can be increased by adding ground planes between neighbor dot electrodes.

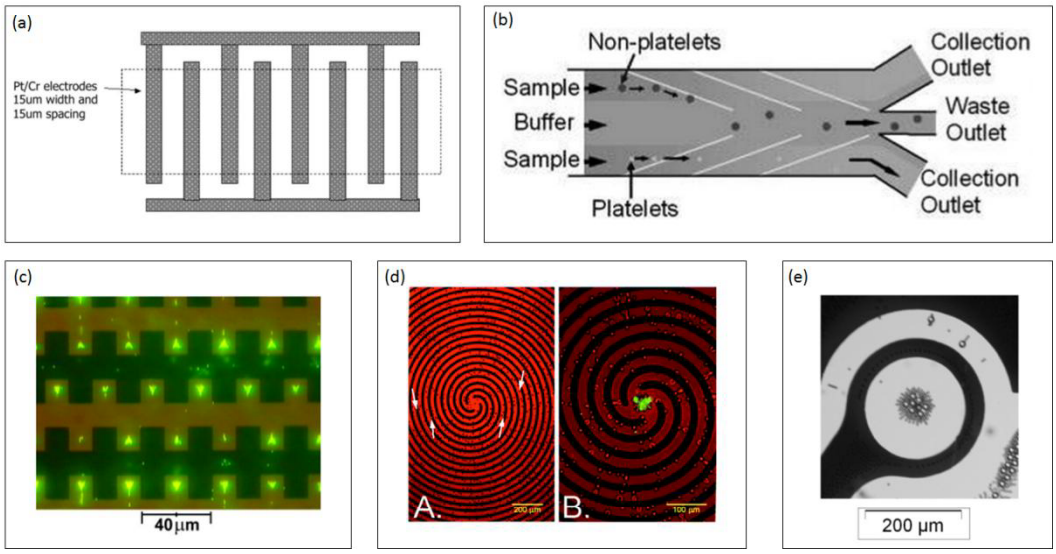

Figure 2.11 Planar electrode configuration examples (a) interdigitated [78] (b) oblique [80] (c) castellated [81] (d) spiral [82], and (e) dot type [78].

2.3.2 3D Microelectrodes

3D electrodes are developed to perform characterization studies on large populations of particles [78]. Some types of 3D microelectrode configurations include sidewall patterned [83], extruded [84] and contactless [85] microelectrodes.

Sidewall patterned configuration (Figure 2.12a) is comprised of vertically embedded 3D electrodes in the sidewalls of the microchannels. Uniform DEP field can be generated along the height of the microchannels. That makes an advantage for manipulating large populations of particles in the microchannel. In contrary, weak DEP fields are generated in the microchannel center and that limits the flow rate and microchannel width.

Extruded configuration (Figure 2.12b) is made to lower the Joule effect and increase the DEP force. Any planar electrode configuration can be used for fabricating extruded microelectrodes. Energizing the extruded electrodes are the same with planar electrodes. Neighbor electrodes are activated with the voltages of the same frequency but with 180° phase difference.

In contactless configuration (Figure 2.12c), 3D electrodes are inserted in a highly conductive solution isolated from the microchannel. Because of the microchannel wall, a capacitance and an electric field are created by applying AC signal to the electrodes. Strong electric field occurs at the interface between conductive solution and microchannel (on the microchannel walls) and weak electric field occurs in the centerline of the microchannel similar to the sidewall patterned configuration.

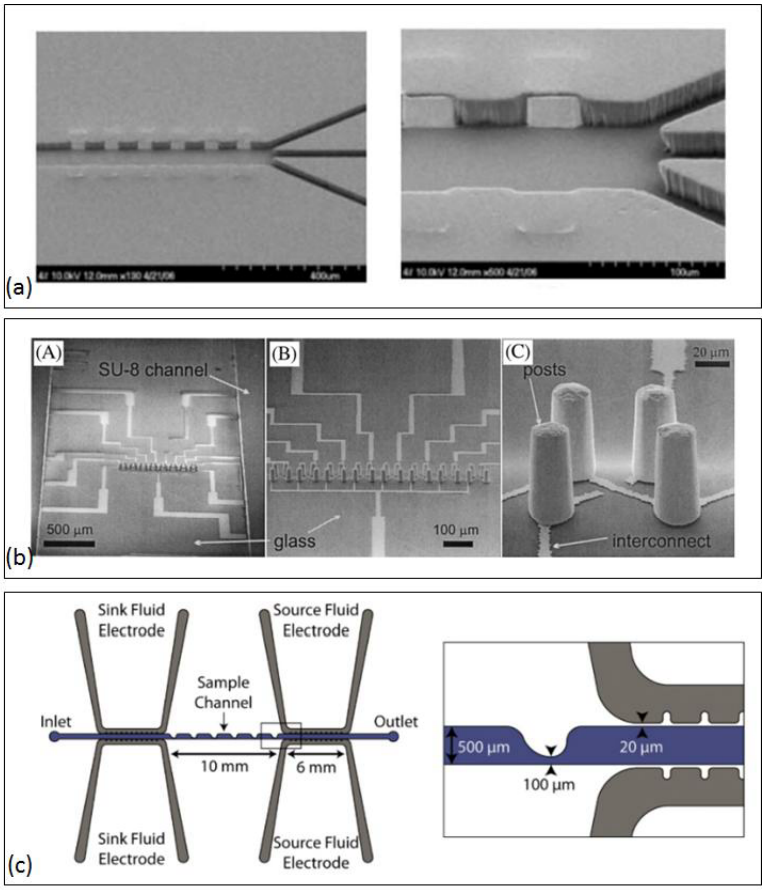

Figure 2.12 3D electrode configuration examples (a) sidewall [83] (b) extruded [84], and (c) castellated [85].

CHAPTER 3

CELLS AND DIELECTRIC MODELING

Dielectric modelling of particles is considerably important in DEP based microfluidic designs. Before applying cells into the DEP system, dielectric properties of the cells and medium should be known to understand the Re (F_{CM}) effect on the dielectrophoretic manipulation of the cells. Dielectric properties of the cells are used as input data during FEM simulations in microfluidic DEP systems. In this chapter, firstly blood and its content is presented and then, cell dielectric modeling ideas and dielectric modeling of cells within the scope of this thesis are explained.

3.1 Structure of Blood

Blood is the principal vehicle and medium that serves to provide nutrients and remove waste products throughout the complex multi-cellular constituents of the body organs. It consists of a plasma fluid with a number of formed elements [86].

Blood accounts for 6-8% of body weight in normal, healthy humans. The density of blood (1060 kg/m^3) is slightly greater than the density of water, mostly because of the high density of RBCs [87].

3.1.1 Blood Plasma

55-60% of blood volume consists of plasma. Plasma is the transparent, amber-colored liquid in which the cellular components are suspended [87]. Blood plasma is about 90-95% water and contains numerous dissolved materials including proteins, lipids, carbohydrates, electrolytes, hormones, and pigments [86].

3.1.2 Blood Cells

Blood consists of 40-45% formed elements. Those formed elements include red blood cells (erythrocytes), white blood cells (leukocytes) and platelets (thrombocytes) [87].

Mammalian red blood cells (RBCs) contain no nucleus or subcellular metabolic structures. They travel as individual cells in blood vessels to deliver oxygen to the tissues. They contain hemoglobin, the oxygen carrier and survive for 3 to 7 months within the blood stream [88]. Because of containing no DNA or RNA, RBCs are unable to synthesize proteins [89]. RBCs are biconcave discs with a diameter of approximate 7 μm [90] and total count of RBCs in blood is 4.3-5.9x10^9 cells/ml for males and 3.5-5.5x10^9 cells/ml for females [91].

White blood cells (WBCs), derived from the common myeloid progenitor cell, are the main components of the innate immune system, which mediates the first-line defense against microbial attack. In general, WBCs can be categorized as neutrophils, eosinophils, basophils, monocytes and lymphocytes [89]. WBCs are spherical with a diameter range of approximately 7-20 μm [90] and total count of WBCs in blood is 4.5-11x10^6 cells/ml [91].

Platelets come from megakaryocytes, which are giant (30 μm) cells from bone marrow. The mean diameter of a platelet is about 1-2 μm [87] and total count of platelets in blood is 150-400x10^6 cells/ml [91].

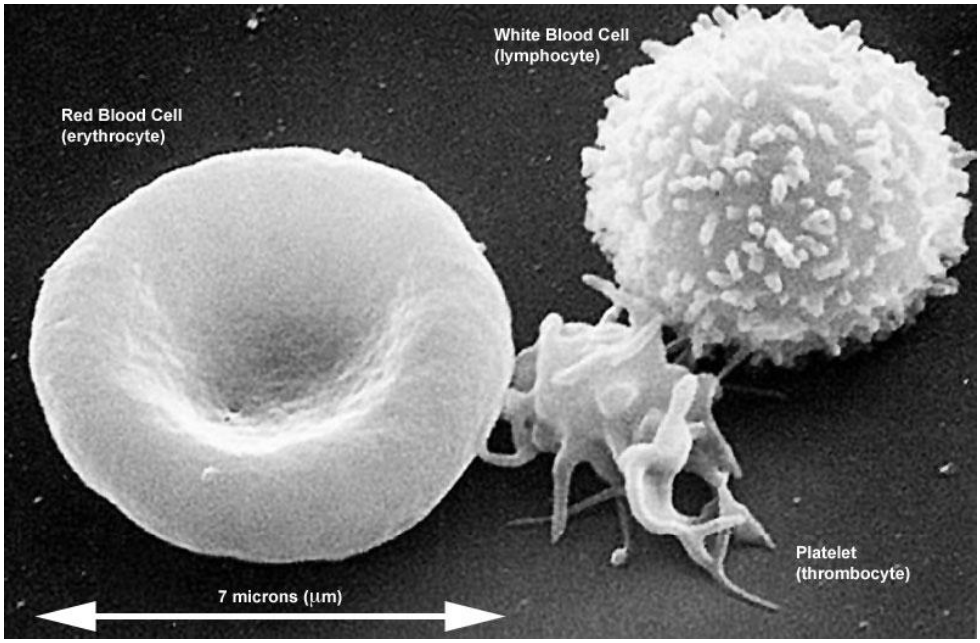

Figure 3.1 SEM image of blood cells [92].

3.1.3 Rare Cells in Blood

Rare cells can be classified as circulating tumor cells (CTCs), antigen-specific T cells, endothelial progenitor cells and hematopoietic stem cells [93].

In metastatic stage of cancer, cancer cells are released from primary cancerous tumor site, enter to the bloodstream and colonize other organs. These cells are named as circulating tumor cells (CTCs) [94].

Various methods have been described for their detection and an initial enrichment step is required, since CTCs are very rare in blood [93]. When using DEP for rare cell enrichment, firstly modeling of the cells should be performed.

3.2 Cell Dielectric Modeling

Cell membrane, which is composed of a phospholipid bilayer with structural proteins embedded in it, acts like a capacitor parallel with a resistor since phosphate groups are conductive and lipid backbone layers in between acts as dielectric structure. Impedance of the cell membrane is calculated utilizing the following formulas for its resistance and capacitance, respectively.

$$R = \frac{L}{\sigma . A} \tag{3.1}$$

$$C = \varepsilon \frac{A}{d} \tag{3.2}$$

In equations above, R and C are used for describing the resistance and capacitance, respectively. σ and ε denote conductivity and permittivity, respectively, and L and A determine perimeter and crossectional area, respectively. d is the thickness of cell membrane. L is calculated as $2\pi r$ and A is calculated as πr^2. After the necessary cancellation, L/A becomes $2/r$ (r is the radius of the cell). Figure 3.2 presents the electrical circuit projection of the cell.

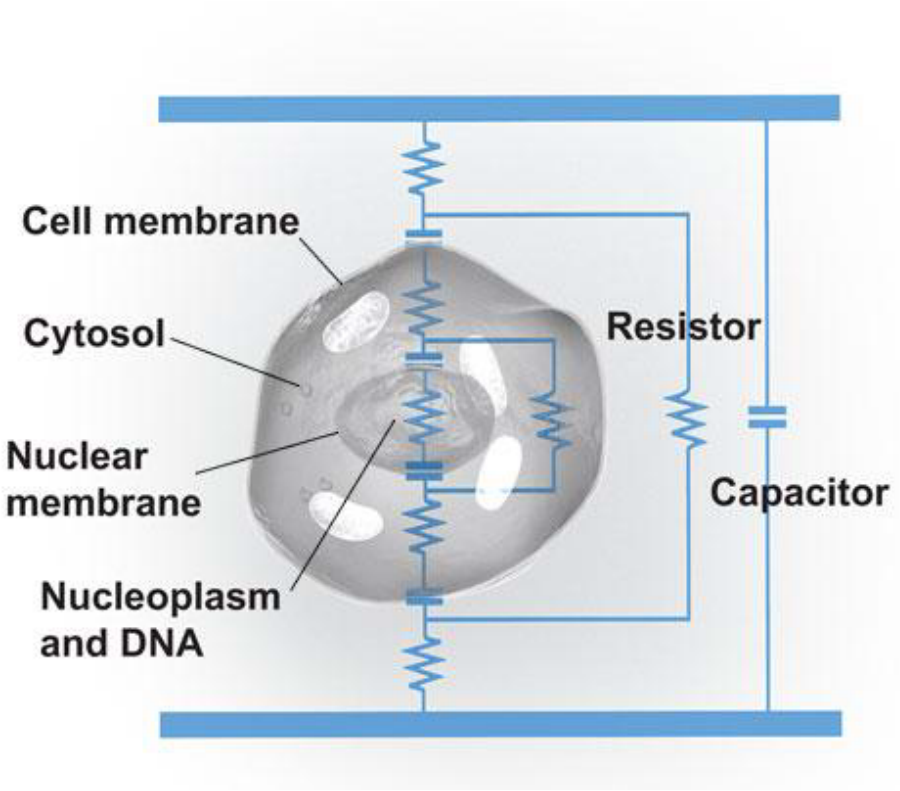

Figure 3.2 The biological cell and electrical circuit projection [95].

The cytoplasm of a biological cell consists of cytosol and organelles (for eukaryotic cells). Cytosol is composed of mostly water and also includes proteins, ions etc. Cytoplasm is more conductive than the cell membrane because of ions and it can be modeled with its impedance like the cell membrane.

To be able to use electrical circuit elements of cells in DEP based microfluidic designs, these parameters should be converted into single complex permittivity formula for membrane and cytoplasm of the cell.

Some cell models have been developed to apply right conversion. General models for cells are spherical and ellipsoidal models. Because of nonhomogeneous structures of cells (for most of them), cell modeling techniques are based on shell numbers around cells, such as single shell modeling, double shell modeling. For the single shell modeling the Claussius–Mossotti factor (f_{CM}) of the cell, which characterizes its dielectric response, is given by:

$$f_{CM} = \frac{\varepsilon^*_{cell} - \varepsilon^*_{med}}{\varepsilon^*_{cell} + 2.\varepsilon^*_{med}} \tag{3.3}$$

where, ε^*_{cell} and ε^*_{med} are the complex permittivity of the cell and the medium, respectively. The real part of the Claussius–Mossotti factor describes the dielectrophoretic force on a cell, whereas the imaginary part gives the electrorotational torque on the cell. The cell interior is regarded as a smooth sphere and the membrane as a smooth, concentric shell. The cell complex permittivity is given by:

$$\varepsilon^*_{cell} = \varepsilon^*_{mem,eff} \cdot \frac{(\frac{r}{r-d})^3 + 2.\frac{\varepsilon^*_{int} - \varepsilon^*_{mem,eff}}{\varepsilon^*_{int} + 2.\varepsilon^*_{mem,eff}}}{(\frac{r}{r-d})^3 - \frac{\varepsilon^*_{int} - \varepsilon^*_{mem,eff}}{\varepsilon^*_{int} + 2.\varepsilon^*_{mem,eff}}} \tag{3.4}$$

where, r is the cell radius, d is the membrane thickness, and $\varepsilon^*_{mem,eff}$ and ε^*_{int} are the effective complex permittivities of cell membrane and cell interior, respectively [96].

3.2.1 Dielectric Modeling of Red Blood Cells (RBCs)

Red blood cells (RBCs) or erythrocytes are continually formed in the bone marrow. RBCs originate from nucleated stem cells, which mature into nucleated erythroblasts, then differentiate into anuclear reticulocytes, and finally into RBC. RBCs are terminally differentiated cells (they cannot divide anymore) and are shed from the bone marrow into the blood circulation [97]. Figure 3.3 presents the enucleation of RBCs.

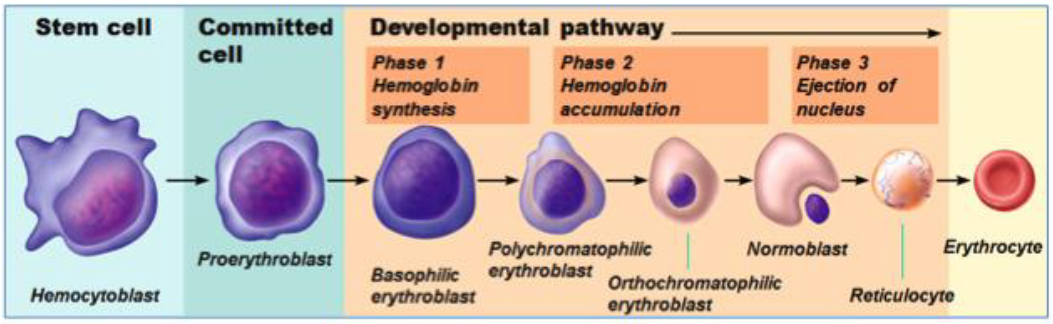

Figure 3.3. Erythropoiesis steps and enucleation of red blood cells.

The presence of a nucleus may prevent big nucleated RBC to squeeze through these small capillaries. Therefore, during the evolutionary development, nature has found that it was better to extrude the nucleus and also other cell organelles, such as endoplasmic reticulum for protein synthesis, which are not needed for their actual function as oxygen carrier [98].

As first shown by the dielectric measurements of Hober et al [99]**,** a red blood cell appears electrically as a conducting sphere (the cytoplasm) surrounded by a resistive membrane. If, negatively charged neuraminic acid residues projecting from their membranes are neglected, then red blood cells can be modeled as a conducting sphere surrounded by a resistive shell [100]**.**

Table 3.1 shows the dielectric parameters of RBCs which are arranged from literature.

Table 3.1 The dielectric parameters of RBCs (N/A: not avaliable).

r_{cell} (μm)	C_{mem} (mF/m^2)	σ_{cyto}(S/m)	ε_{cyto}	**Reference**
2.80	9.00	N/A	N/A	[44]
3.20	10.89	0.40	212	[101]
3.30	8.20	0.54	N/A	[102]
N/A	12.00	0.52	57	[47]
3.50	N/A	0.53	50	[103]
3.20	10.02	0.50	106	Average

According to the parameters in the Table 3.1, ε_{mem} of $RBCs_{average}$ value was calculated from equation (3.2) as 9.06. Cell membrane conductivity was taken as $1x10^{-6}$ S/m and cell membrane thickness was assumed as 8 nm [104]. Then, a MATLAB code [105] according to the single shell modeling was used to draw the $Re(f_{CM})$ – frequency graph (Figure 3.4). The medium conductivity was initially chosen as 2.5 mS/m in MATLAB code. This medium conductivity was reported in a study [106], while defining the dielectric properties of K562 cells. From this point of view, the crossover frequencies of RBCs at 2.5 mS/m medium conductivity were checked first. Then, another medium conductivity was chosen as 10 mS/m and crossover frequencies of RBCs were checked. Based on the graph, positive and negative DEP regions and crossover frequency of RBCs were determined in these two different medium conductivities (2.5 mS/m as reference and 10 mS/m) to compare the crossover frequencies of RBCs.

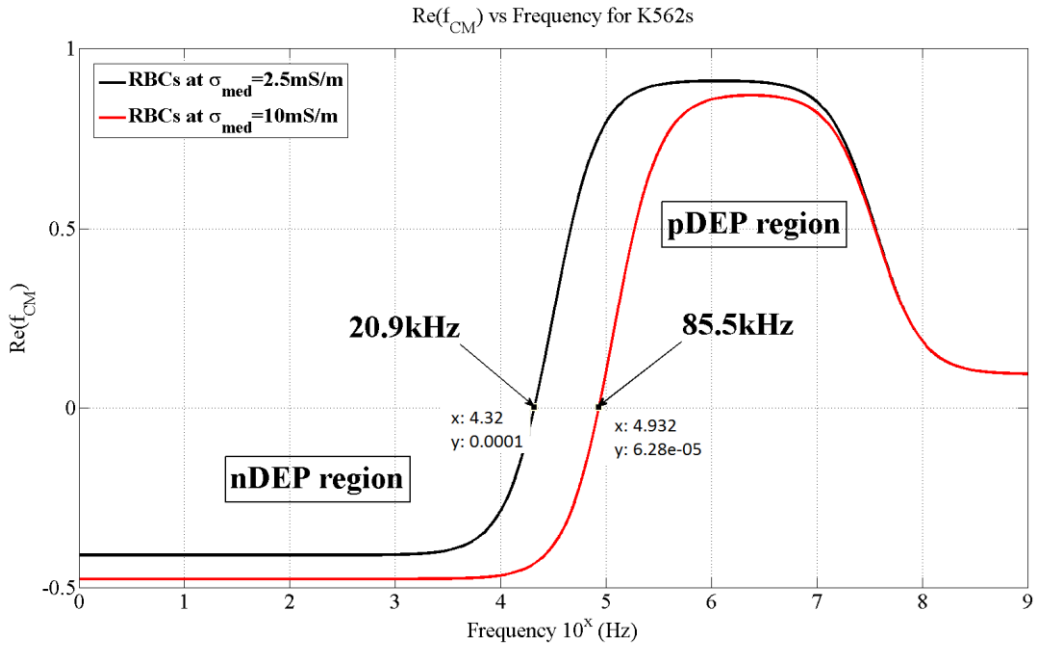

Figure 3.4 $Re(f_{CM})$ vs frequency graph for RBCs at σ_{med} = 2.5 mS/m & 10 mS/m and ε_{med} = 78.

As it can be seen in the Figure 3.4, there are three important regions. First one is nDEP region which contains negative values of $Re(f_{CM})$, second one is crossover frequency points (zeroDEP) where $Re(f_{CM})$ values are equal to zero and the last region is pDEP region which contains positive values of $Re(f_{CM})$. Due to the application of different medium conductivities, crossover frequency points differ. For 2.5 mS/m medium conductivity, crossover frequency of RBCs is 20.9 kHz while for 10 mS/m medium conductivity, crossover frequency of RBCs is 85.5 kHz. $Re(f_{CM})$ value remains positive at higher frequencies and there is no other crossover frequency point for RBCs.

3.2.2 Dielectric Modeling of K562 (Human Chronic Myeloid Leukemia) Cell Lines

Chronic Myeloid Leukemia (CML) is a malignant chronic disorder of hematopoietic stem cells that results in increased myeloid, erythroid and platelet cell count in peripheral blood. The natural history of this disease is a progression from a benign chronic phase to a rapidly fatal blast crisis. The human myeloid cell

line K562 was established by culturing leukemic cells from the pleural effusion of a patient in blastic transformation. K562 cells are arrested in very early stages of development and provide a unique population of primitive human leukemia cells that can be induced to differentiate along with erythroid, monocyte-macrophage, and megakaryocytic lineages in response to various stimuli [107].

Table 3.2 shows the dielectric parameters of K562 cells which are taken from various articles.

Table 3.2 The dielectric parameters of K562 cells (N/A: not avaliable).

r_{cell} (μm)	C_{mem} (mF/m^2)	σ_{cyto}(S/m)	ε_{cyto}	**Reference**
9.20	9.70	0.23	N/A	[31]
9.00	9.70	0.28	N/A	[108]
8.00	8.20	0.23	40	[106]
8.70	9.20	0.25	40	Average

According to the parameters in the Table 3.2, ε_{mem} of $K562s_{average}$ value was calculated from Equation 3.2 as 10.40. Cell membrane conductivity was taken as $1.8x10^{-6}$ S/m and cell membrane thickness was assumed as 10 nm [106]**.** Then, the same MATLAB code [105] which this time has different input parameters was used to draw the $Re(f_{CM})$ – frequency graph (Figure 3.5).

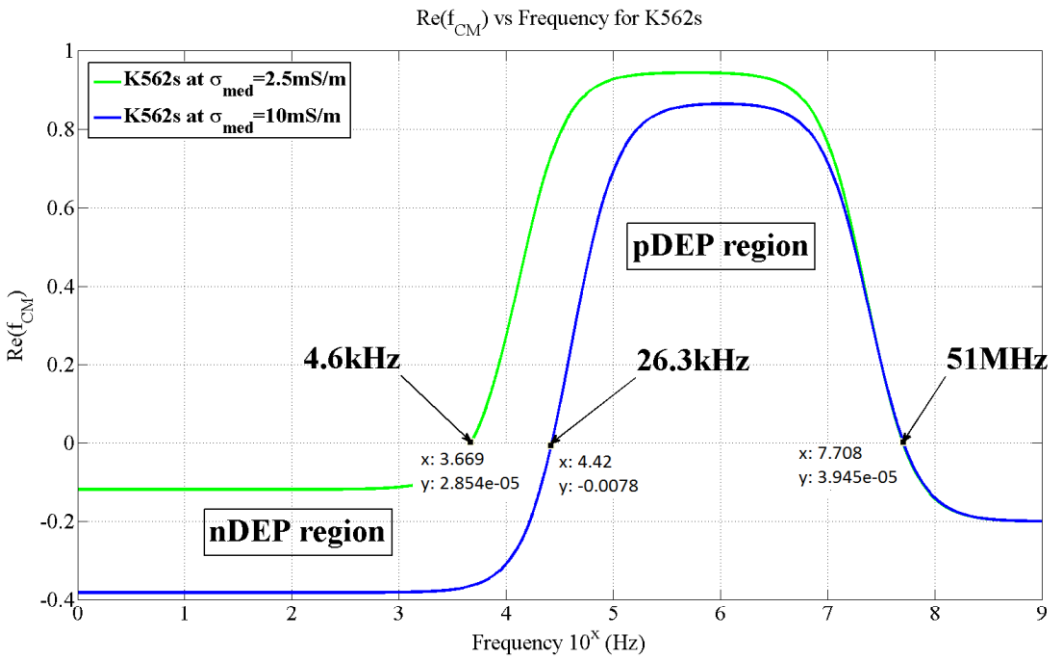

Figure 3.5 Re(f_{CM}) vs frequency graph for K562s at σ_{med} = 2.5 mS/m & 10 mS/m and ε_{med} = 78.

The nDEP region contains negative values of Re(f_{CM}) and pDEP region contains positive values of Re(f_{CM}). At crossover frequency, Re(f_{CM}) values are equal to zero. For K562 cell lines, there are two different crossover frequency points at the same medium conductivity. 4.6 kHz & 51 MHz are the crossover frequencies at 2.5 mS/m medium conductivity, and 26.3 kHz & 51 MHz are crossover frequencies at 10 mS/m medium conductivity. Above 51 MHz, Re(f_{CM}) level again gets negative and the cells observe nDEP force.

3.2.3 Dielectric Modeling of MCF7 (Human Breast Adenocarcinoma) Cell Lines

Breast cancer is a complex and heterogeneous disease. In the laboratory, breast cancer is often modelled using established cell lines. Tremendous advances in our understanding of the biology of breast cancer have been made over the past several decades using breast cancer cell lines [109].

Table 3.3 shows the dielectric parameters of MCF7 cells which are taken from various articles.

Table 3.3 The dielectric parameters of MCF7 cells (N/A: not avaliable).

r_{cell} (μm)	C_{mem} (mF/m^2)	σ_{cyto}(S/m)	ε_{cyto}	**Reference**
9.08	22.20	N/A	N/A	[110]
12.68	N/A	N/A	N/A	[36]
N/A	12.4	0.23	N/A	[38]
10.88	17.3	0.23	50*	Average

* As cytoplasmic permittivity is not available in the literature for MCF7 cells assumption was done based on the same value at similar breast cancer cell lines (MDA-MB231) [101] as 50 for $MCF7s_{average}$.

Because of the limited information about MCF7 cells, some important values were written as N/A in the table. According to the parameters in the Table.3.3, ε_{mem} of $MCF7s_{average}$ value was calculated from Equation 3.2 as 16.69. Cell membrane conductivity and cell membrane thickness was assumed $1.8x10^{-6}$ S/m and 10 nm, similar to K562s.

After that, positive and negative DEP regions and crossover frequency points of MCF7s were checked in the $Re(f_{CM})$ – frequency graph with the help of same MATLAB code used for RBCs and K562s before (Figure 3.6).

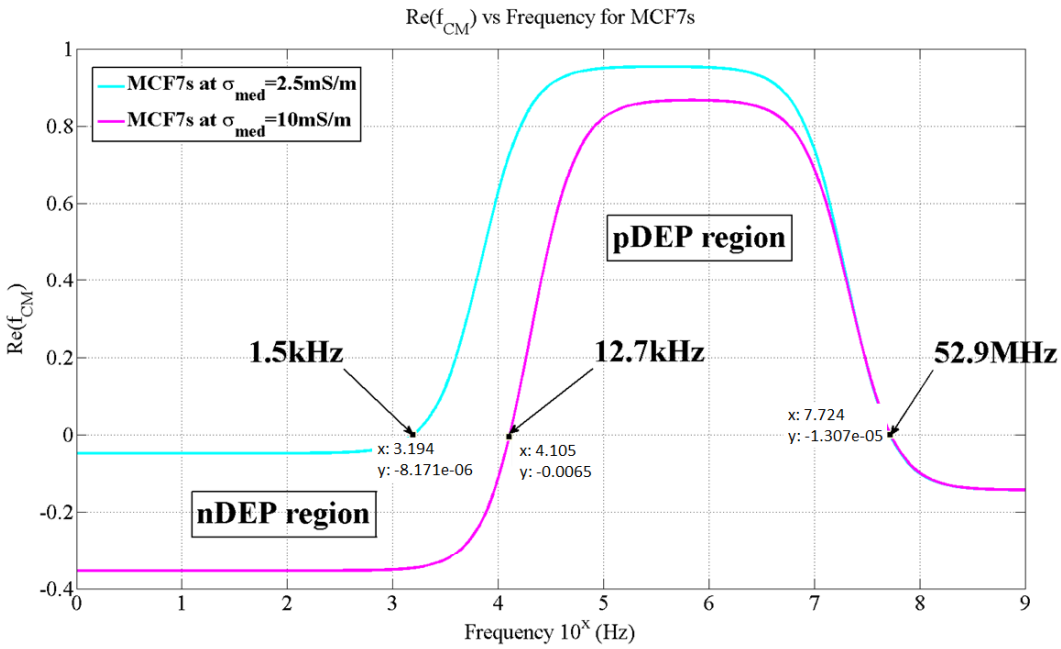

Figure 3.6 Re(f_{CM}) vs frequency graph for MCF7s at σ_{med} = 2.5 mS/m & 10 mS/m and ε_{med} = 78.

For MCF7 cells, there are two different crossover frequency points at the same medium conductivity. 1.5 kHz & 52.9 MHz are the crossover frequencies at the 2.5 mS/m medium conductivity, and 12.7 kHz & 52.9 MHz are the crossover frequencies at the 10 mS/m medium conductivity. Beyond 52.9 MHz frequency, Re(f_{CM}) value gets negative again and the cells observe nDEP force.

3.2.4 Dielectric Modeling of RBC & K562 Mixture

In order to apply different cell types in a mixture to the microchannel, Re(f_{CM}) responses due to frequency of these two cells should be drawn in the same graph and thus, the needed frequency points can be determined easily for the separation of the cells.

Figure 3.5 shows the needed frequency points of these two cell types in the same graph. Medium conductivity was chosen as 10 mS/m due to greater absolute Re(f_{CM}) values at the nDEP regions for both cell types (|-0.5| for RBCs and |-0.4| for K562s) in comparison to 2.5 mS/m medium conductivity.

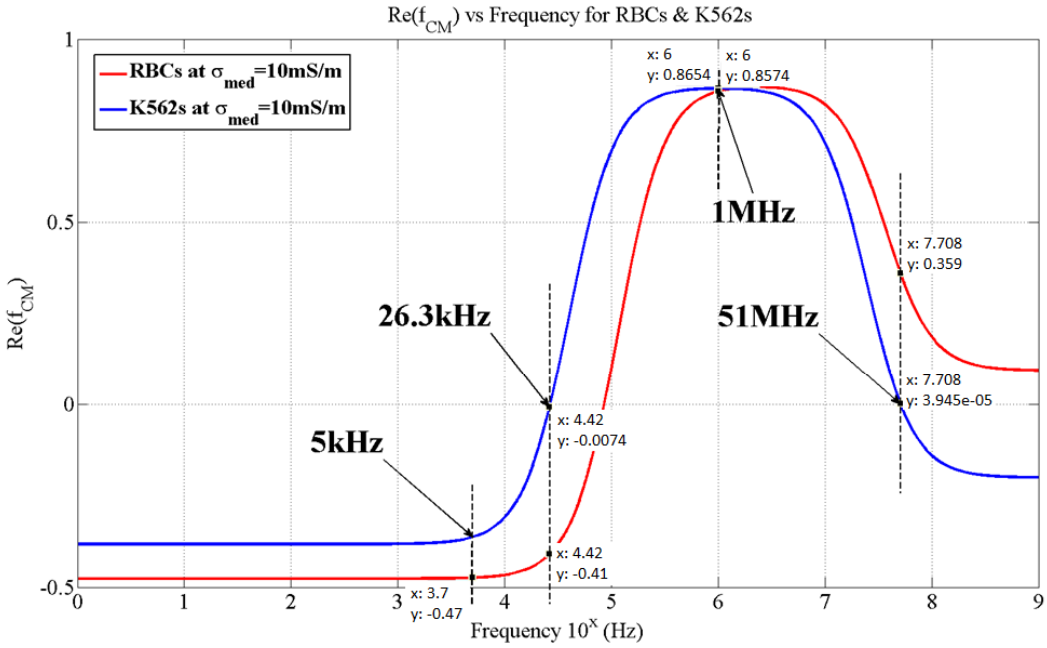

Figure 3.7 $Re(f_{CM})$ vs frequency graph for RBCs and K562s at σ_{med} = 10mS/m and ε_{med} = 78.

5 kHz frequency value can be used for manipulating both cell types by nDEP. 26.3 kHz is crossover frequency point for K562 cells. At this frequency separation of RBCs from K562 cells can be realized, because K562 cells observe no DEP force, while RBCs will be repelled by nDEP. 1 MHz frequency can be used for manipulation of both cell types by strong pDEP. 51 MHz is the other crossover frequency point for K562 cells and separation of RBCs from K562 cells can be realized, because K562 cells observe no DEP force, while RBCs observe pDEP.

3.2.5 Dielectric Modeling of RBC & MCF7 Mixture

The same study was done for RBC & MCF7 cell mixture and both cell types were drawn at the same graph as seen in Figure 3.8. Medium was again chosen as 10 mS/m for a better nDEP separation.

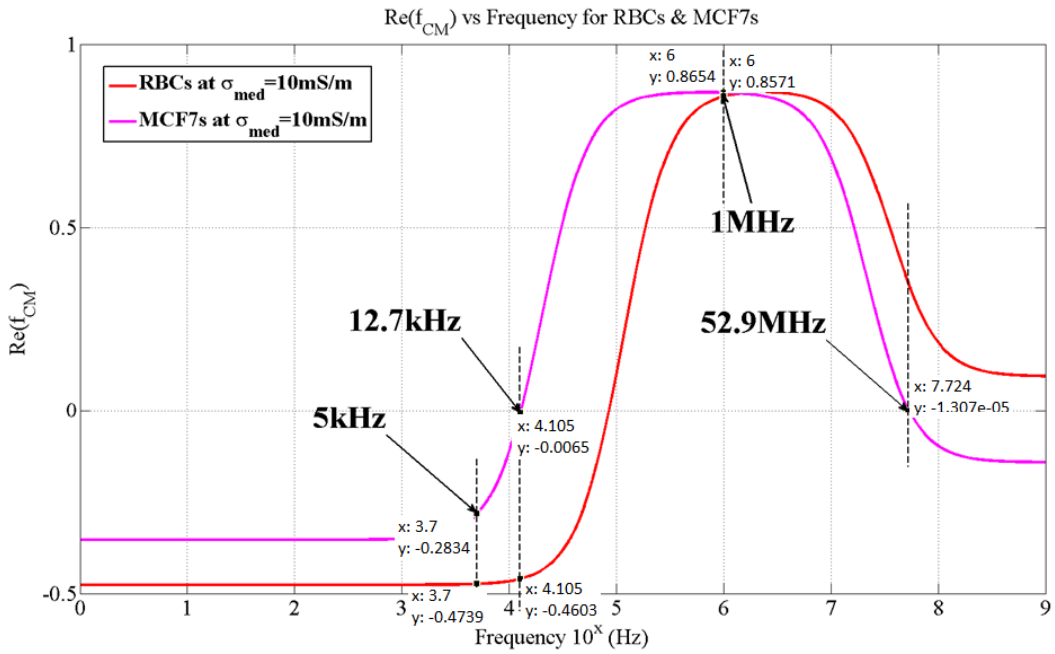

Figure 3.8 $Re(f_{CM})$ vs frequency graph for RBCs and MCF7s at σ_{med} = 10 mS/m and ε_{med} = 78.

5 kHz frequency value can again be used for manipulating both cell types by nDEP. 12.7 kHz is crossover frequency for MCF7 cells and separation of RBCs from MCF7 cells can be realized, only RBCs will observe nDEP force at this frequency. 1 MHz frequency can be used for manipulation of both cell types by strong pDEP. 52.9 MHz is the other crossover frequency point for MCF7 cells and separation of RBCs from MCF7 cells can be realized, as only RBCs observe pDEP at this frequency.

CHAPTER 4

DESIGN AND SIMULATION

In this chapter, the designs of the devices are presented. Firstly, the design of the 1st generation devices, used to apply negative dielectrophoresis (nDEP) for manipulation of cells, is given. Secondly, 2nd generation devices, used to prevent electrolysis effect on the electrodes during nDEP application are explained. Thirdly, two alternatives for 3rd generation device designs are given in details. The modifications in the design of 2nd generation devices to form 3rd generation devices with reasons are also discussed in detail. Finally, the FEM simulations of the designs are demonstrated with the explanation of simulation method in COMSOL Multiphysics® 3.4 software.

4.1 Design of the DEP Devices

4.1.1 The Design of 1st Generation DEP Devices

In the first generation DEP devices, two consecutive DEP regions composed of planar V-shaped electrodes were designed. The parylene-C based microfluidic channel was kept relatively wide (1 mm) in order to avoid channel clogging due to high number of RBCs (5-6x10^9 cells/ml), and to increase the throughput for shorter analysis times (at least 7.5 ml blood is needed to be processed for CTC detection in real samples). The device is designed to operate with nDEP principle. In the first DEP region, it is aimed to focus all cells (RBCs, K562 cells and MCF7 cells) towards the walls of the microchannel with nDEP. This eliminated the need for hydrodynamic focusing, which is done usually by using separate inlets or obstacles inside the microchannel, complicating the operation. Hence, the

proposed system has only one inlet, which is easier to operate. The second DEP region serves to pull only RBCs towards the center, leading to the separation of K562 human leukemia cells (or MCF7 cells) from RBCs. The device has two outlets for the collection of separated cells. Figure 4.1 shows the schematics of proposed device.

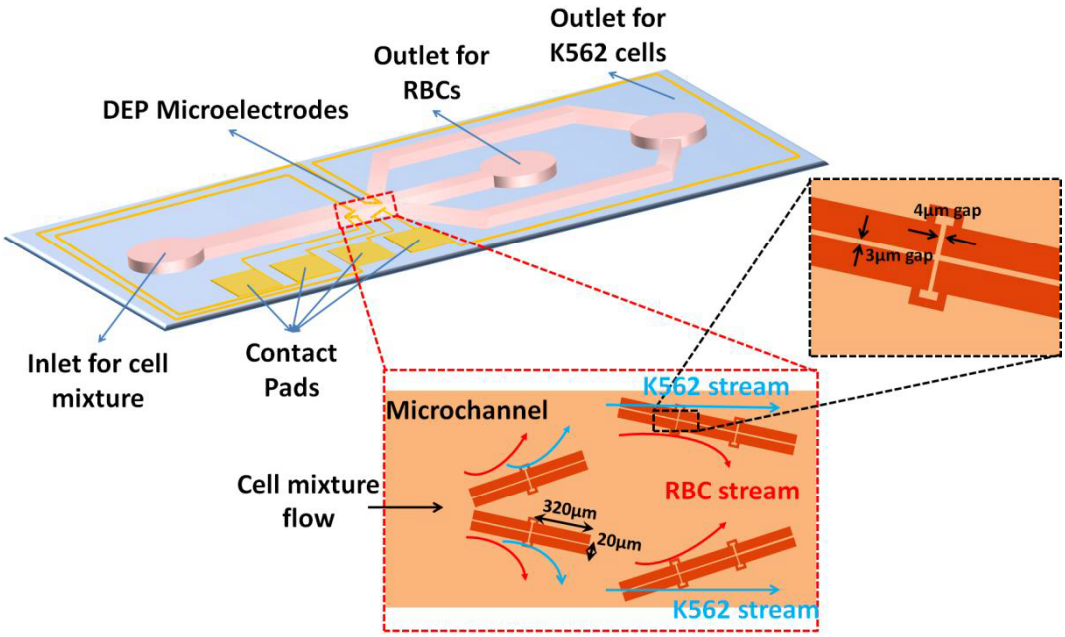

Figure 4.1 The illustration of the 1st generation DEP devices, with enlarged views of DEP area.

In continuous flow microfluidic DEP applications, there basically two forces acting on particles: DEP force and the hydrodynamic forces. While desgining the electrode geometries, these two forces should be considered together. Electrode anglesand spacing between electrodes were chosen carefully to manipulate cells under the continuous hydrodynamic force. To decide the electrode shapes, sizes, distances and angles, iterations should be tried with simulations. Planar electrodes can be easily placed to the bottom of the microchannel and thus large microchannels can be obtained without losing any DEP force in comparison to side-wall electrodes. Main microchannel width was decided as 1000 µm which is the highest limit for parylene-based microchannels to apply whole blood without

any channel clogging problems. Gaps between electrodes were chosen 3 μm between parallel electrodes and 4 μm between collateral electrodes. 3 μm gaps between parallel electrodes increase the DEP force enormously. Collateral electrodes were combined with arcs to make it easier to apply voltage on electrodes. Channel height was limited to 40 μm considering the cell diameter and the DEP force, which decreases in z-axis in planar electrode geometries. Hence, the channel height should be kept relatively small in order to ensure that all cells passing through the channel are affected by DEP force.

The magnitude of the voltage was determined as 20 V_{pp} and the frequency of the voltage was chosen 5 kHz for the first DEP region and 26.3 kHz for the second DEP region according to cell dielectric modeling in MATLAB.

Table 4.1 shows parameters, utilized in the design of 1st generation devices.

Table 4.1 Design parameters utilized for the 1st generation devices.

	Main Channel	**Electrodes**	**Outlet Channels**
Length	2200 μm	320 μm	-
Width	1000 μm	20 μm	500 μm
Height	40 μm	0.4 μm	40 μm
Type of Material	Parylene-C	Gold	Parylene-C
Material Thickness	20 μm	-	20 μm
Angles of outlet channels	-	-	45°
Electrode Type	-	Planar	-
Angles btw electrodes	-	15°	-

Table 4.1 (continued).

Gaps btw electrodes	-	3 μm (parallel) 4 μm (collateral)	-
Gaps btw walls and electrodes	5 μm	5 μm	-
Voltage magnitude	-	20 V_{pp}	-
Voltage frequencies	-	5 kHz & 26.3 kHz 5 kHz & 12.7 kHz	-

4.1.2 The Design of 2nd Generation DEP Devices

The aim of the 2nd generation DEP devices is to increase the cell manipulation efficiency by preventing electrolysis effect on electrodes.

After testing 1st generation devices, it was observed that bubbles were formed on the planar electrodes and expanding bubbles became huge obstacles for cells in continuous flow. Bubble formation was an unexpected issue due to inert properties of gold electrodes. After checking fabrication steps, it was found that 30 nm Titanium layer which is applied to hold gold layer tight to the glass substrate was directly connected to the medium in the microchannel because of undercut during gold etching process. Titanium reacted with water in medium and formed TiO_2. During the reaction, bubble formation observed in all 1st generation devices fabricated.

Fabrication flow of 1st generation devices was checked and it was decided to add an insulating Parylene-C layer coating step between metal etching and microchannel photolithography. Parylene-C layer thickness was decided as 0.5 μm due to uniformity ranges of parylene coating device (SCS PDS-2010 Labcoter).

After fabrication of 2nd generation devices, cell tests were repeated. Adding an extra step including Parylene-C coating prevented electrolysis on electrodes. The

design parameters for the 2nd generation devices are the same with 1st generation devices given in Table 4.1.

4.1.3 The Design of 3rd Generation DEP Devices

3rd generation devices include two different alternative designs, named as grounded version and gapped version.

The aim of the grounded version DEP devices is similar to the 1st and 2nd generation DEP devices, but applying pDEP and high flow rates this time. 1st DEP region in the devices focuses all cells in the mixture towards the walls and then 2nd DEP region selectively manipulates blood cells to the center of the microchannel while not affecting the rare cells. Grounds located between these two electrode regions prevent the crosstalk between two DEP regions, to which different frequencies are applied.

The aim of the gapped version DEP devices is to apply pDEP on flowing cells in high flow rates for manipulation and then filter the blood cells through the gaps on the walls. This system is a combination of electrical and mechanical separation methods.

nDEP idea was tested in 1st and 2nd generation devices, however successful manipulation of cells were observed only at very low flow rates (0.1-1 μl/min), which is not suitable for high throughput operation. Besides, cells escape from the open areas in the middle of the first DEP region electrodes, where the lines of V-electrodes are not physically connected. Besides, the number of the electrode pairs is insufficient for the effective manipulation under continuous flow, which decreases the efficiency of the enrichment.

Due to the drawbacks, 3rd generation DEP devices were designed to manipulate cells with pDEP by applying frequencies at MHz level. By this way, higher DEP forces can be generated, and hence, higher flow rates can be applied, increasing the throughput. Under pDEP force, cells are caught on planar electrodes and then slither on them. This slithering idea is novel in literature and high throughput can

be achieved due to successful slithering in high flow rates. Figure 4.2 and 4.3 show the schematics of proposed alternative designs.

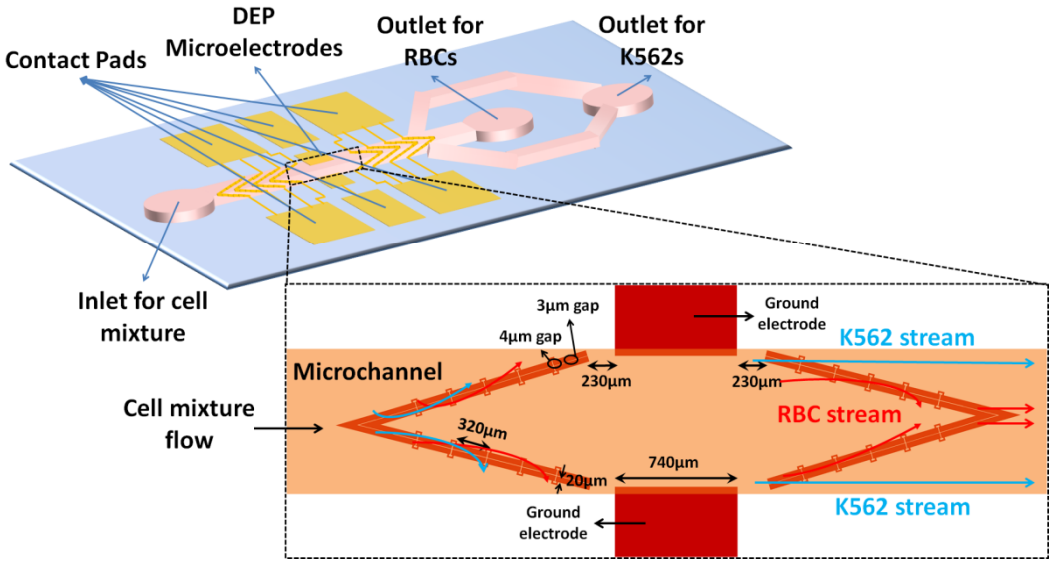

Figure 4.2 The illustration of the 3rd generation DEP devices – grounded version, with an enlarged view of DEP area.

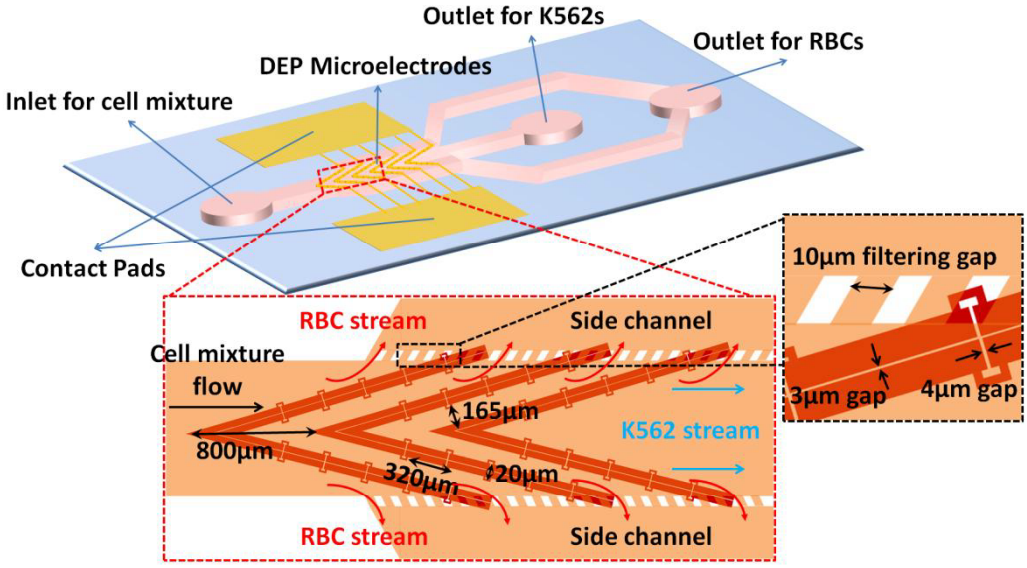

Figure 4.3 The illustration of the 3rd generation DEP devices, with enlarged views of DEP area.

Electrode angles and structures were chosen similar as in 1st and 2nd generation devices, but this time the number of electrode pairs and the lengths of electrodes were increased. To prevent the cell escape in the middle of the channel, the middle of the electrodes were combined to each other to make a closed V-shape structure for successful cell manipulation.

For the grounded version of the 3rd generation devices, pDEP is used for both focusing and selecting the cells in the applied mixture.

Table 4.2 shows parameters, utilized in the design of 3rd generation devices – grounded version.

Table 4.2 Design parameters utilized for the 3rd generation devices – grounded version.

	Main Channel	**Electrodes**	**Side Channels**
Length	13720 μm	320 μm	-
Width	1000 μm	20 μm	500 μm 2x300 μm
Height	20 μm	0.4 μm	20 μm
Type of Material	Parylene-C	Gold	Parylene-C
Material Thickness	20 μm	-	20 μm
Insulating Layer Thickness	-	0.5 μm	-
Angles of side channels	-	-	45°
Electrode Type	-	Planar	-

Table 4.2 (continued).

Angles btw electrodes	-	15°	-
Gaps btw electrodes	-	3 μm (parallel) 4 μm (collateral)	-
Number of electrode pairs	-	10	-
Voltage magnitude	-	>10 V_{pp}	-
Voltage frequency	-	1 MHz & 51 MHz 1 MHz &52.9 MHz	-

For the gapped version of 3rd generation devices, after successful manipulation of cells towards the main channel walls with pDEP, cells are filtrated through 10 μm wide gaps on the walls. Due to the comparison of size ranges of blood cells and K562 cells, it is decided to open 10 μm gaps on walls for optimum filtration in the case of preventing K562 cell escape.

Table 4.3 shows parameters, utilized in the design of 3rd generation devices – gapped version.

Table 4.3 Design parameters utilized for the 3rd generation devices – gapped version.

	Main Channel	**Electrodes**	**Side Channels**
Length	11650 μm	320 μm	-
Width	1000 μm	20 μm	1000 μm 2x500 μm

Table 4.3 (continued).

Height	20 μm	0.4 μm	20 μm
Type of Material	Parylene-C	Gold	Parylene-C
Material Thickness	20 μm	-	20 μm
Insulating Layer Thickness	-	0.5 μm	-
Angles of side channels	-	-	45°
Electrode Type	-	Planar	-
Angles btw electrodes	-	15°	-
Gaps btw electrodes	-	3 μm (parallel) 4 μm (collateral)	-
Number of electrode pairs	-	9	-
Voltage magnitude	-	20 V_{pp}	-
Voltage frequency	-	1 MHz	-

4.2 Simulation Method

After design parameters are determined, simulations were performed in COMSOL Multiphysics® 3.4.

Main idea of performing simulations before fabrication of devices was testing the DEP force distribution on planar electrodes in the microchannel and interaction between DEP force and hydrodynamic force.

Firstly, "*Electrostatics, Generalized"* module in "*Statics"* in "*AC/DC"* module was chosen for simulating DEP force created by planar electrodes. The walls of the microchannel are Parylene-C, thus Laplace equation inside the channel with insulating boundary conditions was solved. Sinusoidal voltage with 180° phase

difference was applied to the parallel electrodes and the electrode boundary conditions were decided according to ±|V| sin (ωt) formula. Electric field gradient term is not constant in DEP equation and it is needed to prove uniformity of DEP force on the electrodes. Equation below was utilized to achieve the simulation:

$$\nabla E^2 = \begin{matrix} \frac{\partial^3}{\partial x^3}+\frac{\partial^3}{\partial y^2 \partial x}+\frac{\partial^3}{\partial z^2 \partial x} & x \\ \frac{\partial^3}{\partial y^3}+\frac{\partial^3}{\partial x^2 \partial y}+\frac{\partial^3}{\partial z^2 \partial y} & y \\ \frac{\partial^3}{\partial z^3}+\frac{\partial^3}{\partial x^2 \partial z}+\frac{\partial^3}{\partial y^2 \partial z} & z \end{matrix} V^2 \qquad (4.1)$$

To apply this equation to COMSOL, an expression was written "*sqrt(((2*(Vx*Vxx+Vy*Vyx+Vz*Vzx))^2)+((2*(Vx*Vxy+Vy*Vyy+Vz*Vzy))^2)+((2*(Vx*Vxz+Vy*Vyz+Vz*Vzz))^2))*" in subdomain plot in post processing part as a plot parameter after solution of the simulation. 3D simulations were utilized, because of the need to track the cell manipulations on the planar electrodes.

For particle tracing simulations combined with electrostatics, *"Incompressible Navier Stokes, steady state analysis"* in *"Microfluidics"* in *"MEMS"* module was chosen. Because of the combination of electrostatics and microfluidics, the streamline plot in post processing part should be modified. In COMSOL, velocity field equations in x, y, and z directions are defined with *u*, *v*, and *w* for the given medium, respectively. Due to 3D manipulation, caused by planar electrodes, these velocity field components should be written as:

$$\begin{matrix} u+((constant)*(2*(Vx*Vxx+Vy*Vyx+Vz*Vzx))) \\ v+((constant)*(2*(Vx*Vxy+Vy*Vyy+Vz*Vzy))) \\ w+((constant)*(2*(Vx*Vxz+Vy*Vyz+Vz*Vzz))) \end{matrix} \qquad (4.2)$$

for DEP force applications, where *u*, *v* and *w* are the medium velocities in *x*, *y* and *z* directions, and constant is expressed as:

$$constant = \frac{\varepsilon_m}{\mu}\frac{r^2}{3}\, Re(F_{CM}) \tag{4.3}$$

Constant values were calculated according to Eqn. 4.3 for RBCs, K562s and MCF7s in different frequency levels. Table 4.4 shows the constant values for different cell types.

Table 4.4 Cell parameters and constants with different frequencies utilized for the 1st & 2nd generation devices.

	RBCs	**K562s**	**MCF7s**
Radius (μm)	3.2	8.7	10.9
Medium Permittivity	78	78	78
Medium Viscosity	8.92×10^{-4}	8.92×10^{-4}	8.92×10^{-4}
Constant @ 5 kHz	-1.188×10^{-18}	-7.043×10^{-18}	-8.653×10^{-18}
Constant @ 26.3 kHz	-9.464×10^{-19}	2.595×10^{-21}	N/A
Constant @ 12.7 kHz	-1.135×10^{-18}	N/A	5.61×10^{-21}

According to the Table 4.5, RBCs have negative constants and nDEP is dominant for RBCs in 5 kHz, 26.3 kHz and 12.7 kHz. K562 cells have two constants and the constant at 26.3 kHz is about thousand fold lower than the constant at 5 kHz, which cannot manipulate K562 cells. Thus 26.3 kHz can be assumed as crossover frequency for K562 cells. The same ratio is calculated for MCF7 cells at 5 kHz and 12.7 kHz, thus 12.7 kHz can be assumed as crossover frequency for MCF7 cells. Theoretically, constants should be exactly zero at 26.3 kHz and 12.7 kHz levels for K562 cells and MCF7 cells, respectively. Exact zero values for Re (f_{CM})

cannot be decided from applied MATLAB graphs, because of the limitation to 100000 data points in the written MATLAB code.

Starting velocities and entrance length for the microchannel inlets can be chosen individually. Starting velocity was initially chosen as 0.015 m/s, which is calculated as 18 μl/min according to the microchannel size and entrance length was chosen as 0.15 m, because of the applied inlet tubing length. No slip boundary conditions were utilized with incompressible Navier–Stokes equation. Outlet boundary conditions were chosen as zero pressure, because they are at atmospheric pressure.

4.2.1 Simulations of 1st Generation DEP Devices

Calculations of constant values and determination of signs for velocity expressions paved the way for 3D particle tracing simulations for 1st generation DEP devices. It is known that the gradient of electric field square should be greater than 10^{12} (kg^2m/s^6A^2) for the manipulation of biological cells. Hence, 3D electric field simulation of 1st generation devices and 3D particle tracing simulations were made by using parameters given in Table 4.5.

Table 4.5 Given parameters for 1st generation devices in COMSOL.

Electric field gradient simulations (Electrostatics, generalized module)	Boundary conditions	subdomain 1 (microchannel)	Electric insulation
		subdomain 2 (planar electrodes)	Electric potential
	Fluidic properties	subdomain 1 (microchannel)	$\sigma=1x10^{-2}$ S/m; $\varepsilon=78$
		subdomain 2 (planar electrodes)	$\sigma=45.6x10^{6}$ S/m; $\varepsilon=1$
	Solution part	solved equation	Laplace
		time interval for 5 kHz	$0:5x10^{-5}:2x10^{-4}$
		time interval for 26.3 kHz	$0:9.5x10^{-6}:3.8x10^{-5}$
		time interval for 12.7 kHz	$0:1.97x10^{-5}:7.88x10^{-5}$

Table 4.5 (continued).

Particle tracing simulations (Incompressible Navier-Stokes module)	Boundary conditions	subdomain 1 (microchannel)	Inlet: laminar inflow; average velocity= 0.015 m/s; entrance length= 0.15m, walls : no slip outlet: pressure, no viscous stress, 0 Pa
		subdomain 2 (planar electrodes)	Not active
	Fluidic properties	subdomain 1 (microchannel)	density= 10^3 kg/m^3; dynamic viscosity=8.92×10^{-4} Pa.s
		subdomain 2 (planar electrodes)	Not active
	Solution part	solved equation	Incompressible Navier-Stokes
		time interval	Stationary

In determining the design parameters on planar electrodes, straight-singular, straight-double and castellated electrodes were simulated with 30° angles and the DEP forces created were compared. Figure 4.4, 4.5, and 4.6 show the electric field gradient square along straight-singular, straight-double, and castellated planar electrodes, respectively.

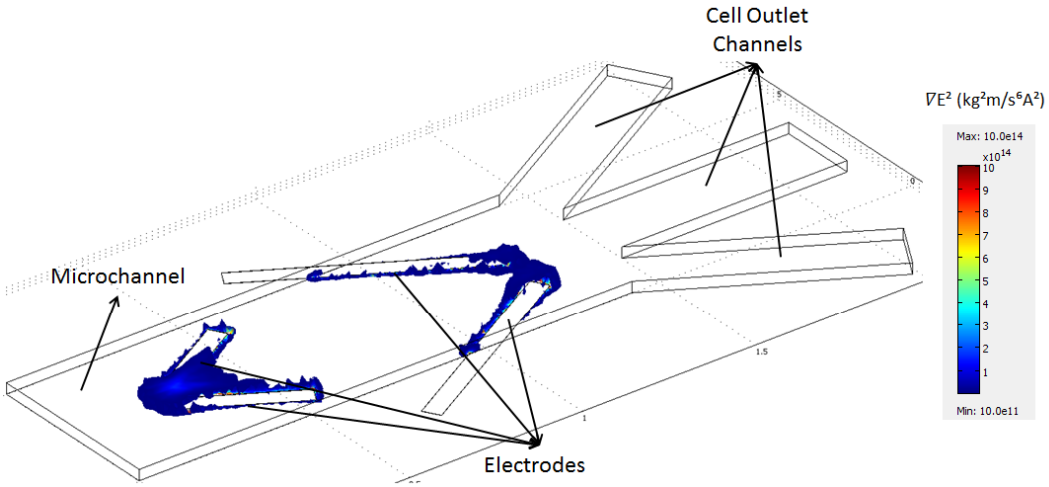

Figure 4.4 3D electric field gradient simulation of simplified design – straight electrodes.

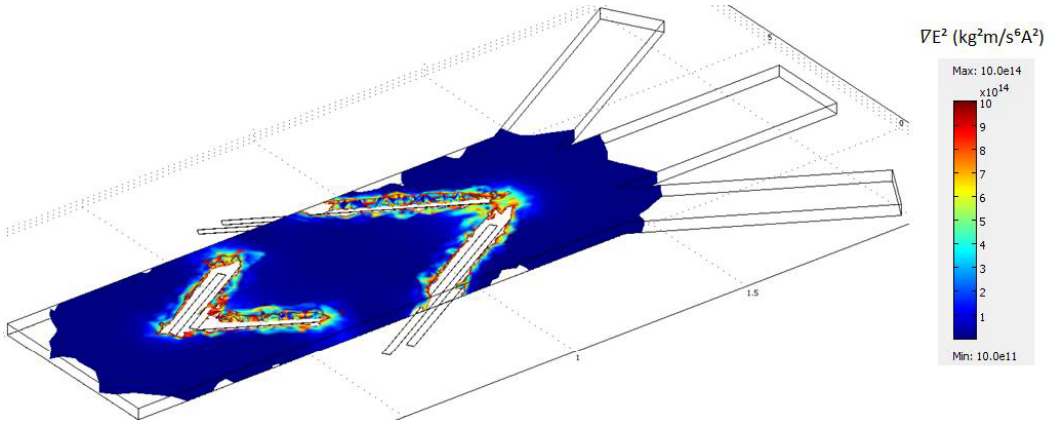

Figure 4.5 3D electric field gradient simulation of simplified design – straight-double electrodes.

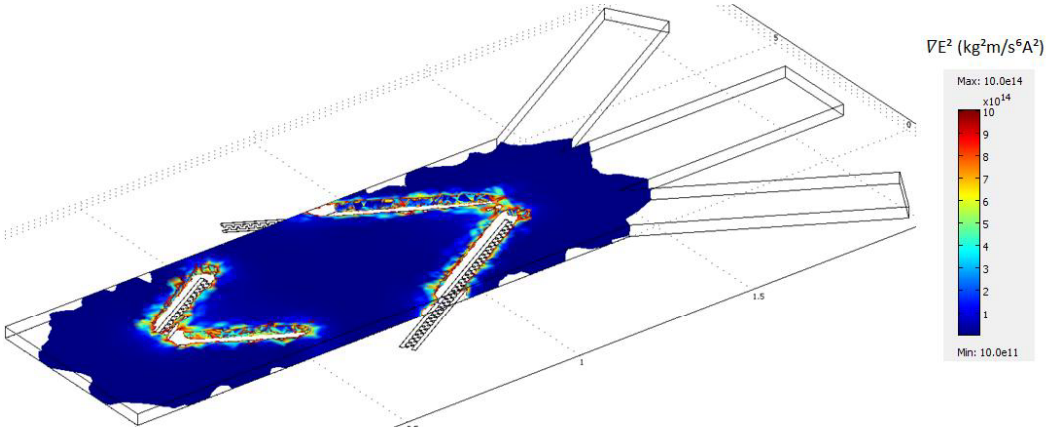

Figure 4.6 3D electric field gradient simulation of simplified design – castellated electrodes.

When the DEP forces are checked from the figures, it can be seen that 50 μm wide straight-singular electrode shape cannot create enough electric field gradient to manipulate cells around electrodes, but it can be easily understood from other figures that, 20 μm wide straight-double electrodes and castellated electrodes create required electric field gradient to manipulate cells around electrodes. Because of the high manipulation power of straight-double electrode structure, it was decided to continue to improve design with this kind of electrode type. Figure 4.7, 4.8 and 4.9 show modified versions of straight-double electrodes in the microchannel.

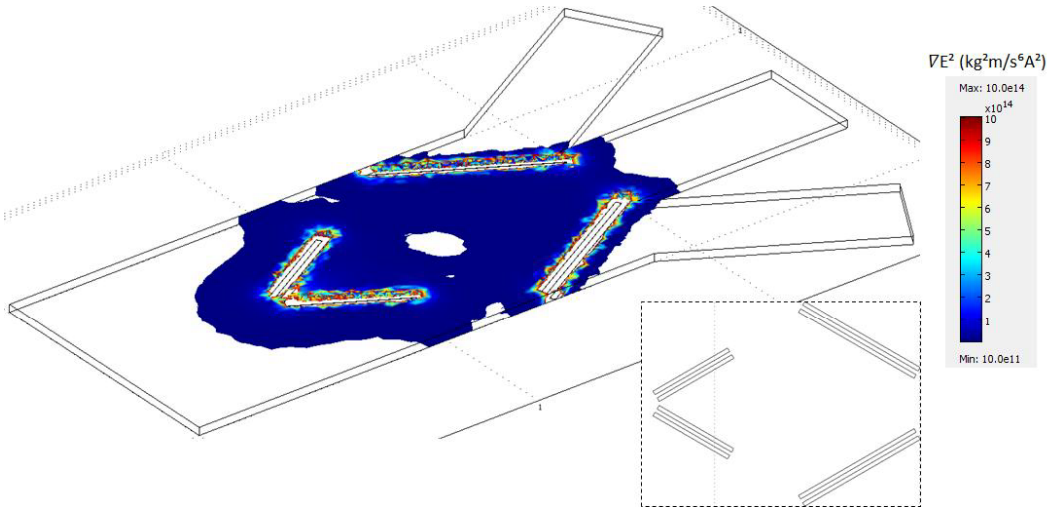

Figure 4.7 3D electric field gradient simulation of simplified design – 30° straight-double electrodes.

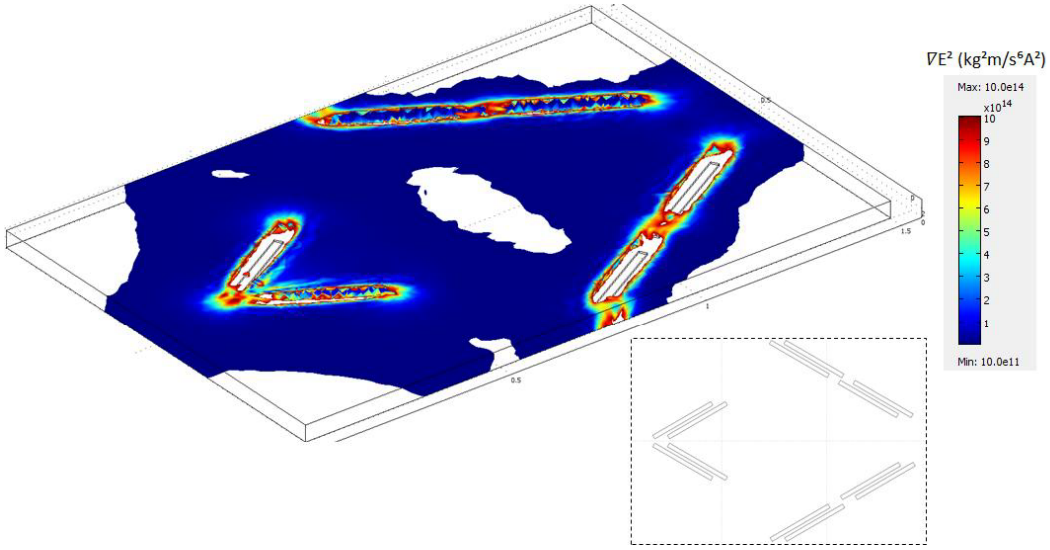

Figure 4.8 3D electric field gradient simulation of simplified design – 30° straight-double electrodes, diagonally divided.

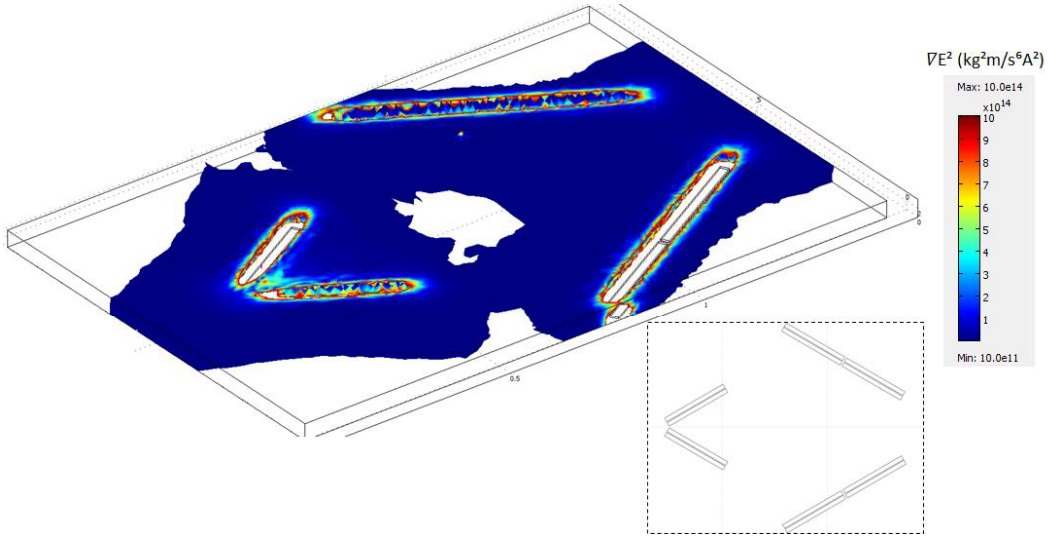

Figure 4.9 3D electric field gradient simulation of simplified design – 30° straight-double electrodes, linearly divided.

To increase the nonuniformities in the electric field, long electrodes were divided into two parts with two different ways. Although diagonal division caused a decrease around the electrodes, linear division protected the electric field, while creating extra nonuniformity. Thus, linear division was chosen for modification.

After proper electrode modifications, 3D particle tracing simulations were made for straight-double electrodes to see proper cell manipulations. 30° and 15° electrode angles were compared and because of inaccurate results in 30° electrode structures, it was decided to apply 15° angle for electrode locations to get a proper cell manipulation in the microchannel. Figure 4.10 shows the 3D electric field gradient simulation for 15° straight-double electrodes.

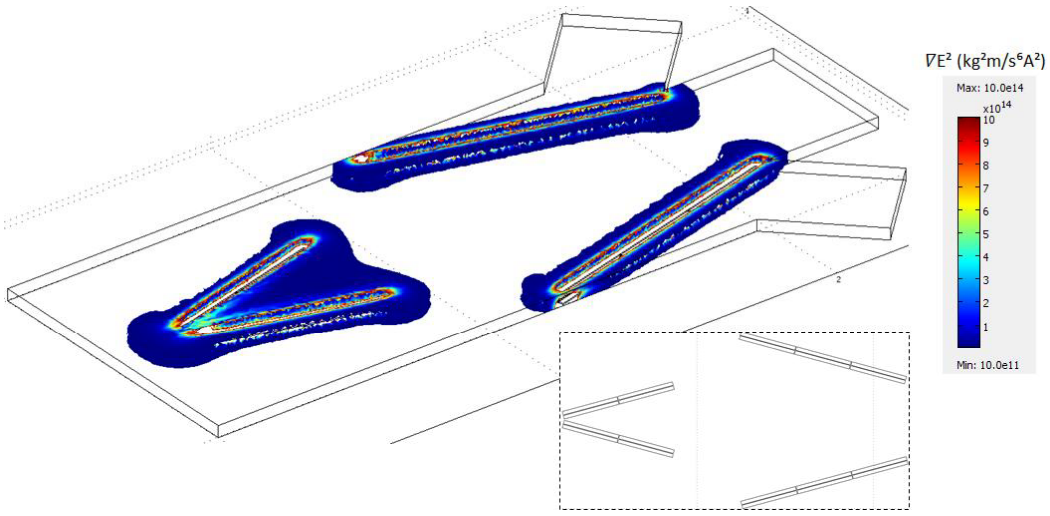

Figure 4.10 3D electric field gradient simulation of simplified design – 15° straight-double electrodes, divided.

According to the parameters given in Table 4.4, streamlines of RBCs, K562 cells and MCF7 cells were simulated. Considering RBC and K562 cell mixture, 5 kHz and 26.3 kHz frequencies were applied for both cell types. It is known that only one omega parameter can be given as an input datum in Comsol Multiphysics® 3.4, thus only one frequency domain is solved for every simulation. Simulation results for both cells in 5 kHz and 26.3 kHz can be found in Appendix A. After obtaining simulation images, new merged images were created from 5 kHz and 26.3 kHz particle tracing simulations for RBCs and K562 cells. Figure 4.11 and 4.12 show merged images of the 3D particle tracing simulations for these cells due to their dielectric properties at two different frequencies.

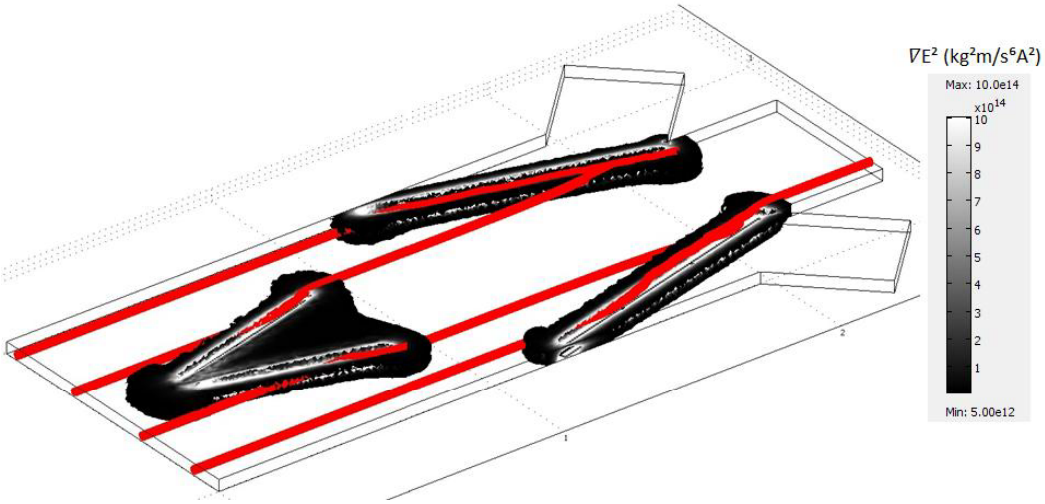

Figure 4.11 3D particle tracing simulation for RBCs at 5 kHz activation for 1st DEP region & 26.3 kHz activation for 2nd DEP region.

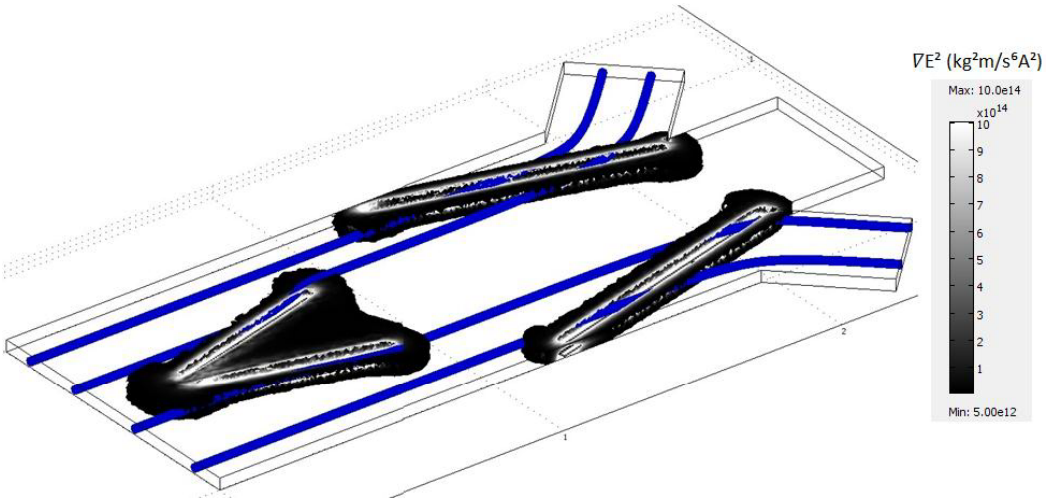

Figure 4.12 3D particle tracing simulation for K562 cells at 5 kHz activation for 1st DEP region & 26.3 kHz activation for 2nd DEP region.

Dielectric modeling of RBCs and K562 cells shows that both cell types are exposed to nDEP in 5 kHz and they can be focused towards microchannel walls due to first DEP region electrode locations. On the other hand, crossover frequency of K562 cells was calculated as 26.3 kHz, when this frequency is applied to the second DEP region in the microchannel K562 cells cannot be manipulated and they will continue to their flow without any direction change, but

it is not the same for RBCs and they are exposed to nDEP in 26.3 kHz and manipulated towards the center of the microchannel.

Considering RBC and MCF7 cell mixture, 5 kHz and 12.7 kHz frequencies were applied for both cell types. Simulation results for both cells in 5 kHz and 12.7 kHz can be found in Appendix A. After obtaining simulation images, new merged images were created from 5 kHz and 12.7 kHz particle tracing simulations for RBCs and MCF7 cells. Figure 4.13 and 4.14 show merged images of the 3D particle tracing simulations for these cells due to their dielectric properties at two different frequencies.

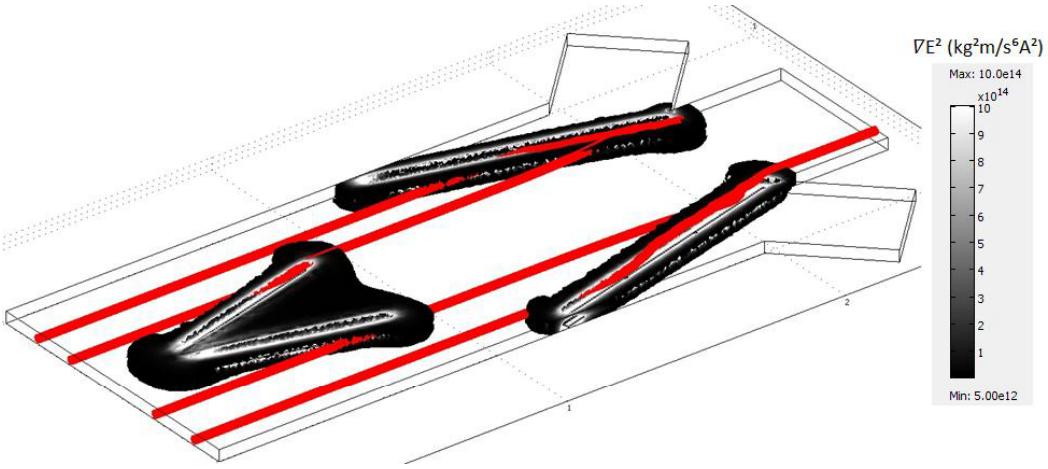

Figure 4.13 3D particle tracing simulation for RBCs at 5 kHz activation for 1st DEP region & 12.7 kHz activation for 2nd DEP region.

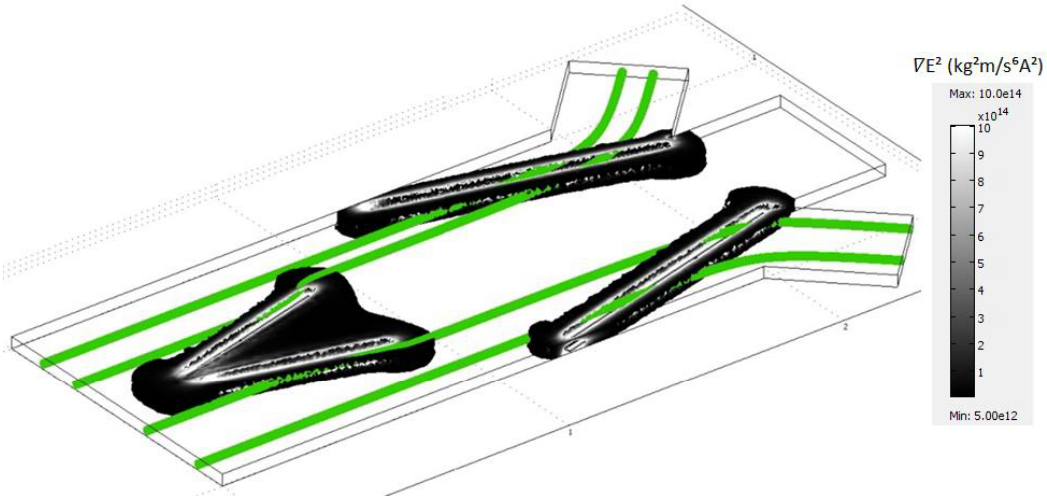

Figure 4.14 3D particle tracing simulation for MCF7 cells at 5 kHz activation for 1st DEP region & 12.7 kHz activation for 2nd DEP region.

4.2.2 Simulations of 2nd Generation DEP Devices

Coating the electrodes with 0.5 μm thick Parylene-C to prevent electrolysis necessitates to make simulations to compare the electric field gradients in 1st and 2nd generation devices. Table 4.6 presents the parameters used for the 2nd generation devices in COMSOL.

Table 4.6 Given parameters for 2nd generation devices in COMSOL.

Electric field gradient simulations (Electrostatics, generalized module)	Boundary conditions	subdomain 1 (microchannel)	Electric insulation
		subdomain 2 (planar electrodes)	Electric potential
		subdomain 3 (insulating layer)	Electric insulation
	Fluidic properties	subdomain 1 (microchannel)	$\sigma=1x10^{-2}$ S/m; $\varepsilon=78$
		subdomain 2 (planar electrodes)	$\sigma=45.6x10^{6}$ S/m; $\varepsilon=1$
		subdomain 3 (insulating layer)	$\sigma=1x10^{-16}$ S/m; $\varepsilon=2.95$
	Solution part	solved equation	Laplace
		time interval for 5 kHz	$0:5x10^{-5}:2x10^{-4}$
		time interval for 26.3 kHz	$0:9.5x10^{-6}:3.8x10^{-5}$
		time interval for 12.7 kHz	$0:1.97x10^{-5}:7.88x10^{-5}$

2D electric field gradient simulations of 1st and 2nd generation device electrodes were made and results were compared. Figure 4.15 and 4.16 show the electric field gradient differences in naked and 0.5 µm Parylene-C coated electrodes.

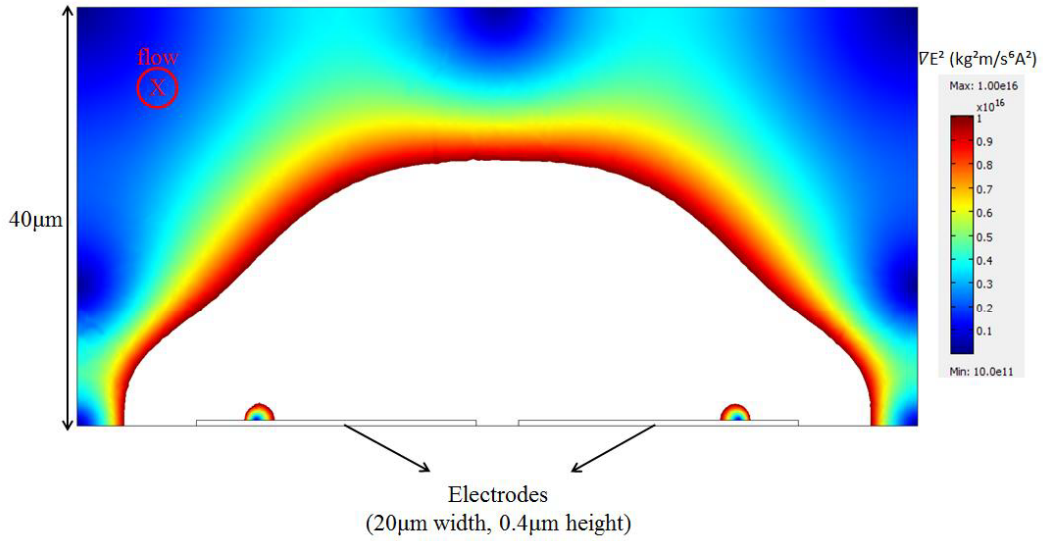

Figure 4.15 2D electric field gradient simulation for 1st generation device electrodes.

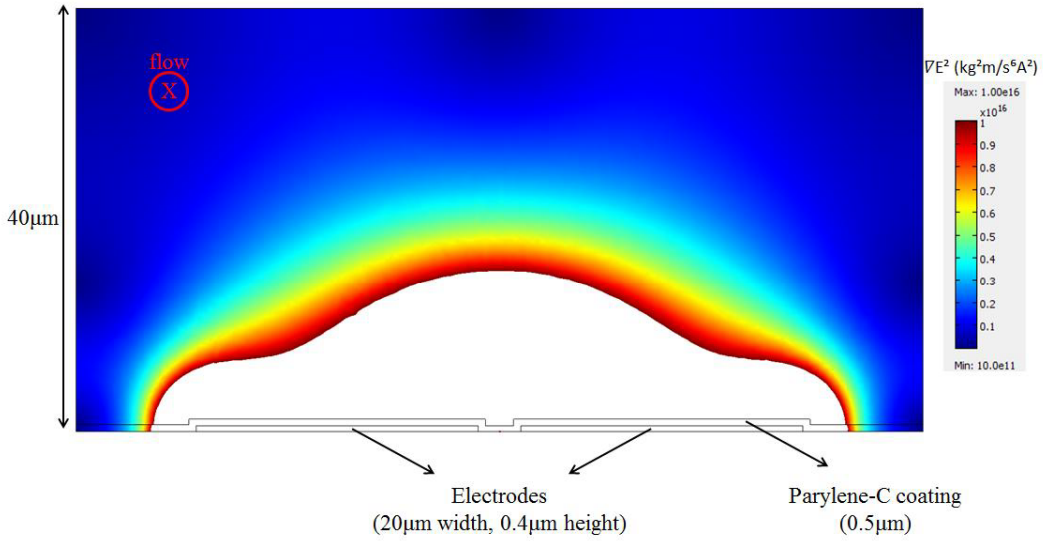

Figure 4.16 2D electric field gradient simulation for 2nd generation device electrodes.

When the DEP fields were compared, a decrease in the DEP force due to the 0.5 μm coating can be seen. To understand the level of decrease, two graphs were made and analyzed. Figure 4.17 and 4.18 show the amounts of electric field gradients of naked and Parylene-C coated devices, respectively.

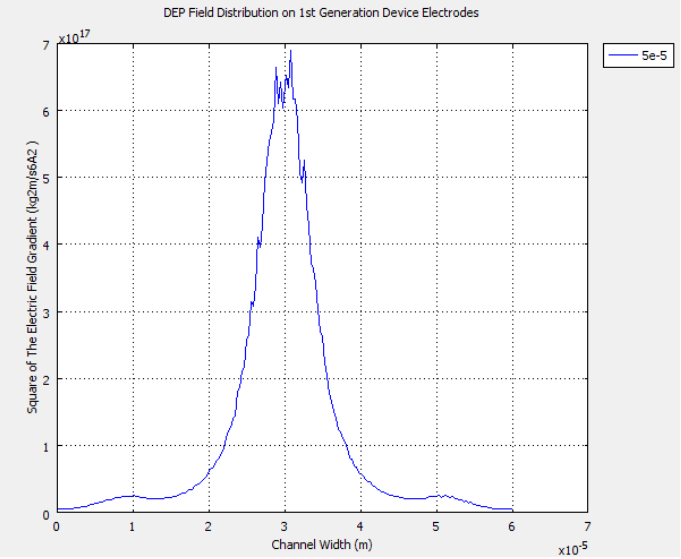

Figure 4.17 Electric field gradient-Channel width graph for 1st generation device electrodes.

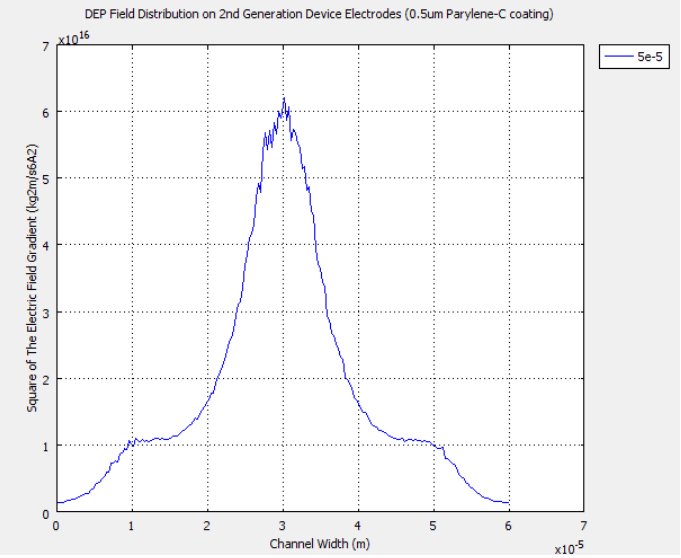

Figure 4.18 Electric field gradient-Channel width graph for 2nd generation device electrodes.

The graphs show that there is a ten-fold decrease in the DEP force. It is obvious that decrease will cause an efficiency lost in testing the devices, but preventing electrolysis is essential for getting proper results from the devices during cell tests.

4.2.3 Simulations of 3rd Generation DEP Devices

3rd generation devices were designed for applying pDEP for slithering and manipulating of cells on the planar electrodes. Application of pDEP brings the idea of cell slither on the electrodes, when a sensitive balance is made between hydrodynamic force and DEP force in the microchannel. Table 4.7 presents the applied parameters of 3rd generation devices in COMSOL.

Table 4.7 Given parameters for 3rd generation devices in COMSOL.

Electric field gradient simulations (Electrostatics, generalized module)	Boundary conditions	subdomain 1 (microchannel)	Electric insulation
		subdomain 2 (planar electrodes)	Electric potential
	Fluidic properties	subdomain 1 (microchannel)	$\sigma=1x10^{-2}$ S/m; $\varepsilon=78$
		subdomain 2 (planar electrodes)	$\sigma=45.6x10^{6}$ S/m; $\varepsilon=1$
	Solution part	solved equation	Laplace
		time interval for 1 MHz	$0:2.5x10^{-7}:1x10^{-6}$
Particle tracing simulations (Incompressible Navier-Stokes module)	Boundary conditions	subdomain 1 (microchannel)	Inlet: laminar inflow; average velocity= 0.012 m/s; entrance length= 0.15m, walls : no slip outlet: pressure, no viscous stress, 0 Pa
		subdomain 2 (planar electrodes)	Not active
	Fluidic properties	subdomain 1 (microchannel)	density= 10^3 kg/m^3; dynamic viscosity=$8.92x10^{-4}$ Pa.s
		subdomain 2 (planar electrodes)	Not active
	Solution part	solved equation	Incompressible Navier-Stokes
		time interval	Stationary

During the cell tests of the 1st and 2nd generation devices, some cell escapes from DEP region were observed due to empty region between arms of V-shaped electrodes. To prevent cell escapes, electrodes were extended and combined. A closed V-shaped electrode structure was designed and simulated. Figure 4.19 shows the electric field gradient distributions of new closed V-shaped electrodes.

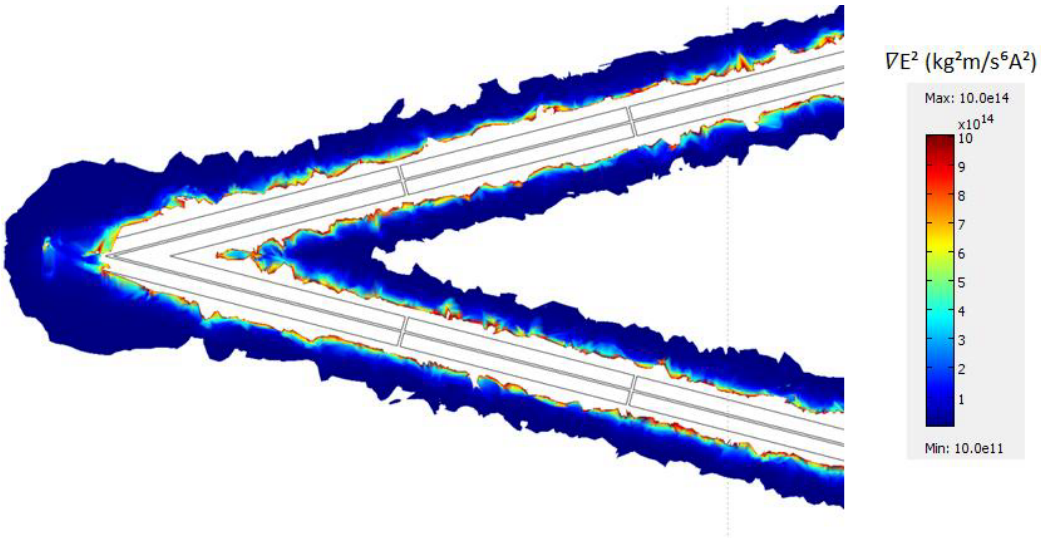

Figure 4.19 Top view of electric field gradient simulation around closed electrodes.

For the simulations of grounded version of 3rd generation devices, capacity of ground electrodes to prevent crosstalk between electrodes activated with different frequencies, were studied. 3D voltage distributions with and without ground electrodes were simulated. Ground electrodes separate the voltage distribution regions and thus crosstalk between electrodes can be prevented. Figure 4.20 shows the voltage distribution simulation results in the microchannel with and without ground electrodes.

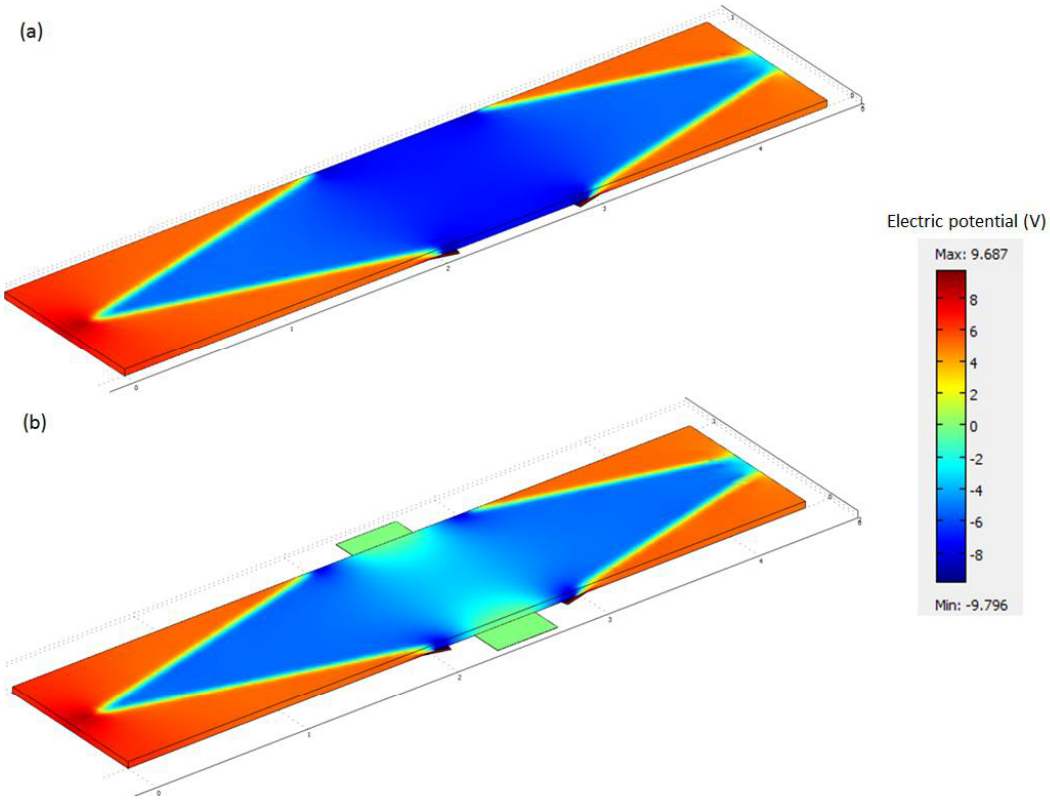

Figure 4.20 Voltage distributions in the microchannel (a) without and (b) with ground electrodes.

After voltage distribution simulations, 3D electric field gradient simulations were performed with the grounded versions of 3rd generation device designs. For the first DEP region, an extra electrode pairs was added and the electric field gradient amount between these two neighboring electrode pairs was checked and no abnormalities in the electric field gradient were observed. Results proved that DEP field was above the cell manipulation level next to the V-shaped electrodes and ground electrodes. Figure 4.21 presents the electric field gradient distribution for grounded version of 3rd generation devices.

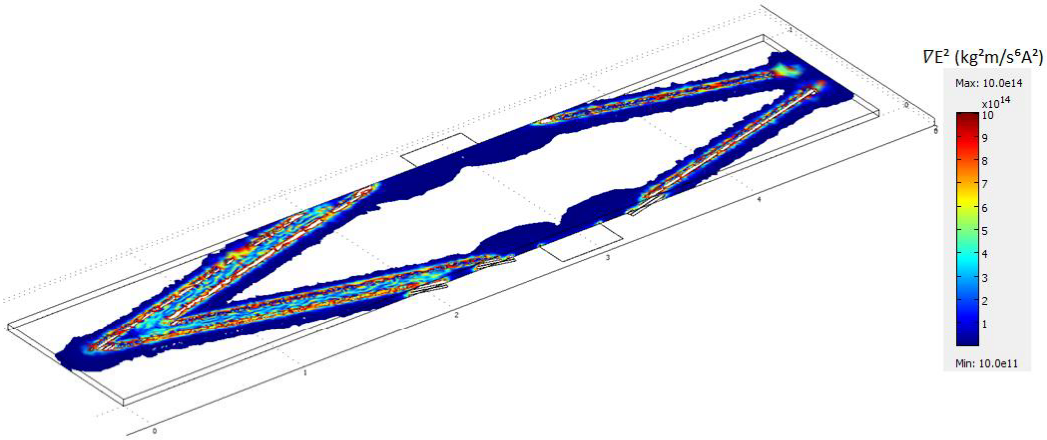

Figure 4.21 The electric field gradient distribution for grounded version of 3rd generation devices.

Then, 3D electric field gradient simulations were made with new types of electrodes in the gapped version of 3rd generation device designs. Different types of side channel gaps were tried and DEP force distribution was checked. Figure 4.22 and 4.23 show DEP force distribution around two different gap types.

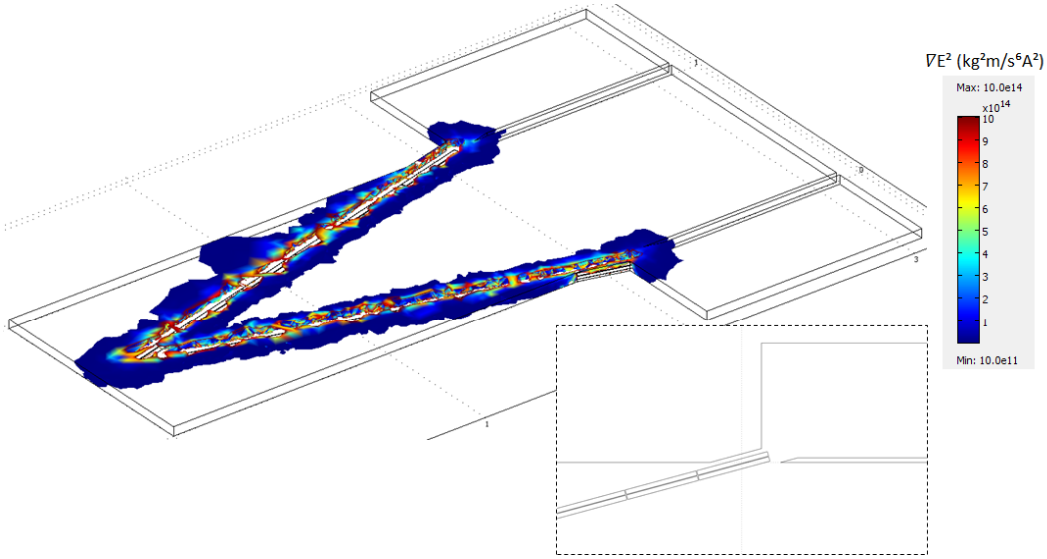

Figure 4.22 3D electric field gradient simulation of simplified gap design version 1.

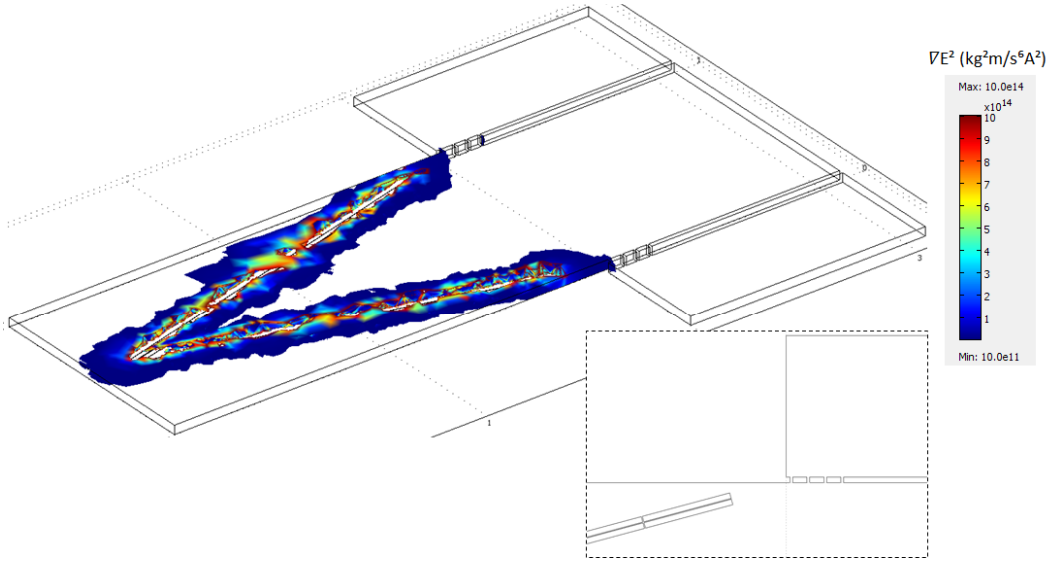

Figure 4.23 3D electric field gradient simulation of simplified gap design version 2.

Because of the importance of the gap size adjustments on the walls, 2D hydrodynamic simulations were made without electric field gradient simulations. Various alternatives were tried on main channel width, gap angle, wall length and wall depth, respectively. Gap vertical width was held constant at 10 μm because it is a key parameter for filtration of cells with different sizes.

Table 4.8 shows the parameters tried for gap regions in 2D hydrodynamic simulations.

Table 4.8 Parameters which were tried for gap regions in 2D hydrodynamic simulations.

	1st alternative	**2nd alternative**	**3rd alternative**	**4th alternative**
Gap angle	45°	15°	30°	90°
Gap vertical width	10 μm	10 μm	10 μm	10 μm

Table 4.8 (continued).

Gap entrance width	14.1 µm	38.6 µm	20 µm	10 µm
Main channel width	1000 µm, 500 µm	-	-	-
Wall length	20 µm , 50 µm, 100 µm	-	-	-
Wall depth	20 µm, 100 µm	-	-	-

Firstly, the effect of main microchannel size on the pressure and velocity of the medium was observed. Figure 4.24 and 4.25 show the 1000 µm and 500 µm width effects on velocity and pressure differences.

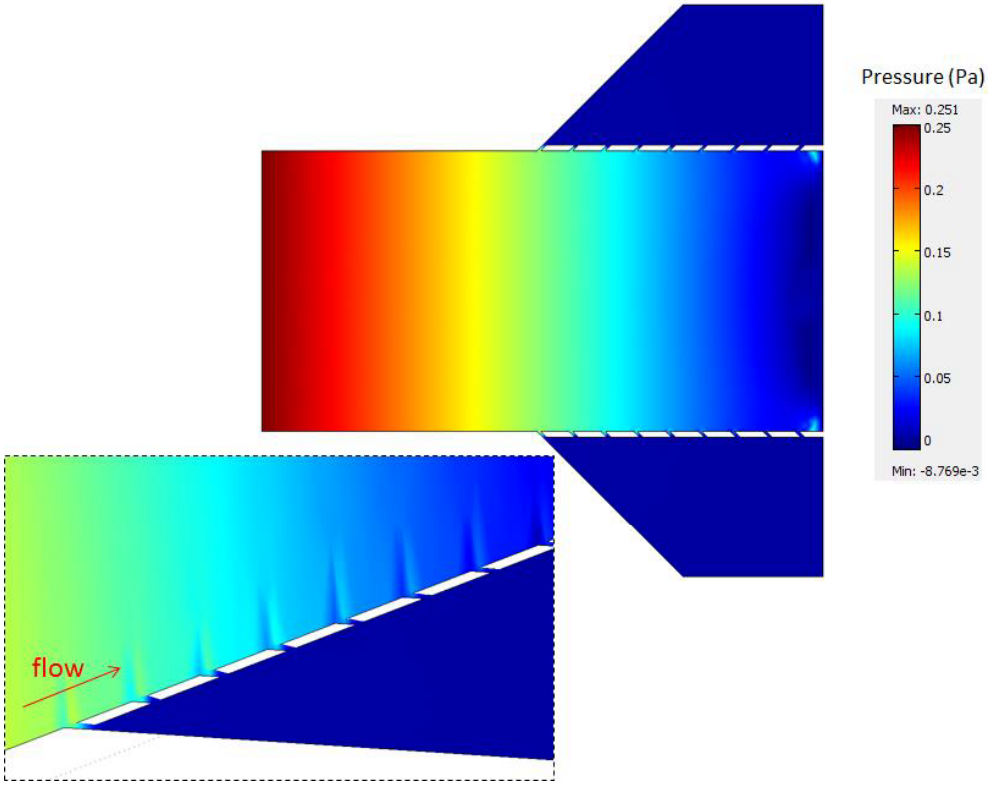

Figure 4.24 2D hydrodynamic flow simulation – 1000 µm main channel width, 45° gap angle, 100 µm wall length, 20 µm wall depth.

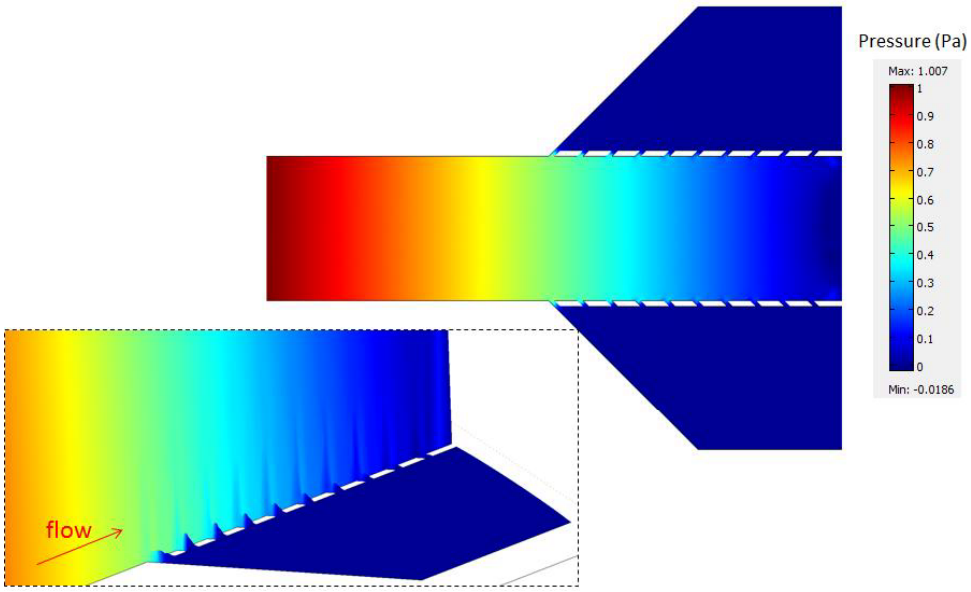

Figure 4.25 2D hydrodynamic flow simulation – 500 µm main channel width, 45° gap angle, 100 µm wall length, 20 µm wall depth.

In the 500 µm width main channel, the pressure drop is higher than 1000 µm width main channel when same inlet velocities are applied for both channels. Narrowing main channel can be thought as a better choice for increasing mechanical filtration due to relatively high pressure drops on the gaps, but it can also increase the vacuuming effect on the gaps and the cells which are thought to be filtered and traveled only in the main channel can pass to the side channels through gaps. On the other hand, because of the need for applying high amounts of cells in the main microchannel, 1000 µm width is a better option than 500 µm width. Hence, 1000 µm was again chosen for 3rd generation device design.

When it is checked carefully, pressure and velocity drops from first gaps to the last one can be distinguished. Every peak should be adjusted equal to each other for a proper filtration through all gaps. Because of the need for velocity peak equalities, three different gap angles were tried in addition to 45° gap angle for comparison. Figure 4.26, 4.27 and 4.28 show the 15°, 30° and 90° gap angle effects on velocity and pressure differences, respectively.

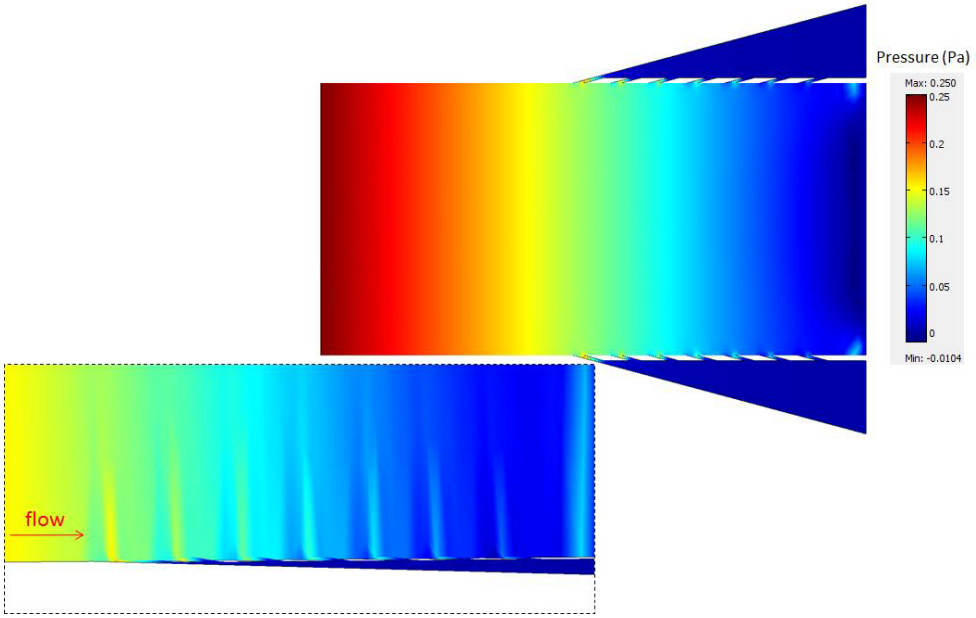

Figure 4.26 2D hydrodynamic flow simulation – 1000 μm main channel width, 15° gap angle, 100 μm wall length, 20 μm wall depth.

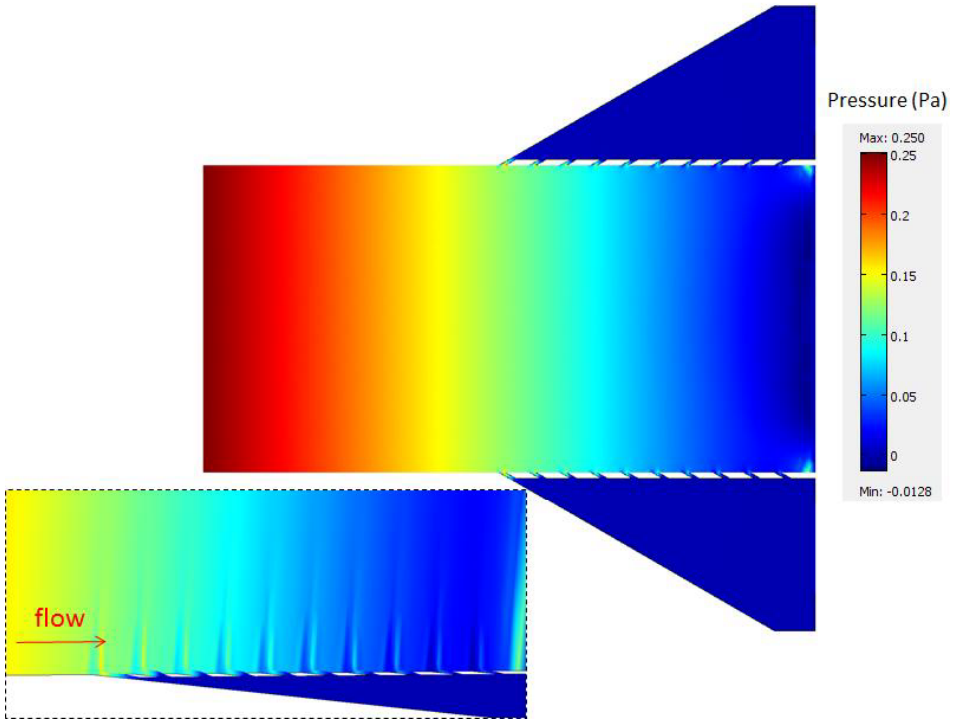

Figure 4.27 2D hydrodynamic flow simulation – 1000 μm main channel width, 30° gap angle, 100 μm wall length, 20 μm wall depth.

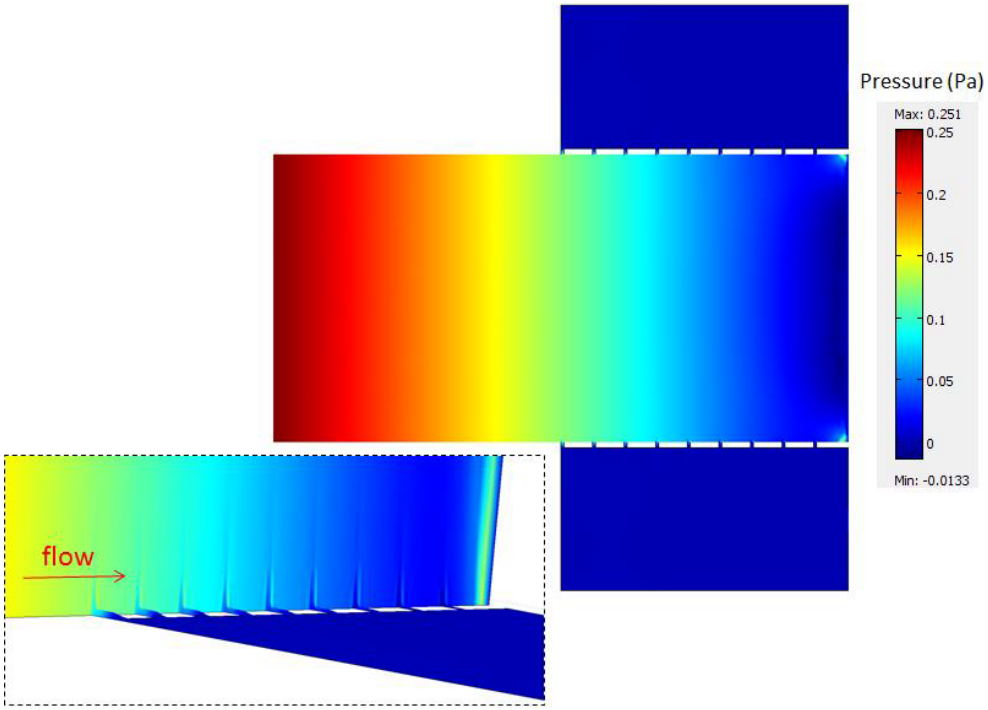

Figure 4.28 2D hydrodynamic flow simulation – 1000 μm main channel width, 90° gap angle, 100 μm wall length, 20 μm wall depth.

When the gaps in alternative angles were checked, it can be seen that at 90° angle, the filters lose permeability (nearly no pressure and no velocity field after 5th gap). 15° angle has the same angle with electrodes and better to use, but gap numbers should be decreased due to the narrow angle. However the number of gaps plays a key role on efficiency of filtering mechanism. Relatively better velocity field distribution results of 30° gap angle makes it the best alternative when compared with 45° gap angle, based on these simulations.

Gap angle adjustments raised a new problem, size expansion at the gap entrance. Hence, gap angles and gap entrances sizes should be considered at the same time with velocity drops on gaps.

The aim of utilizing a filtration mechanism in the 3rd generation devices is to get rid of most of the RBCs using their small sizes. While doing so, the gap entrances should not be plugged up with K562 cells or other cancer cells. However,

decreasing the gap angle 15º or 30º increases gap entrance size to 20 µm and 38.6 µm, allowing all sizes of cells to enter and clog the gaps. 10 µm gap entrance is perfect for filtering idea, but the high velocity drop causes the loss of permeability. Hence, it was decided to draw the gaps at 45° gap angles.

After the decision of gap angles and main channel width, wall length and wall depth could be determined. While the wall depth is decided by the durability of Parylene-C, the wall length is decided both by durability of Parylene-C and gap numbers.

20 µm wall length seems very advantageous in comparison to 100 µm and 50 µm lengths, because more gaps can be made due to short wall length and it increases the filtration efficiency in the microchannel. Hence, 20 µm wall length was chosen for 3rd generation device design. Figure 4.29 and 4.30 show relatively, the 50 µm and 20 µm wall length effects on velocities of medium in the microchannel as alternatives to 100 µm wall length between gaps.

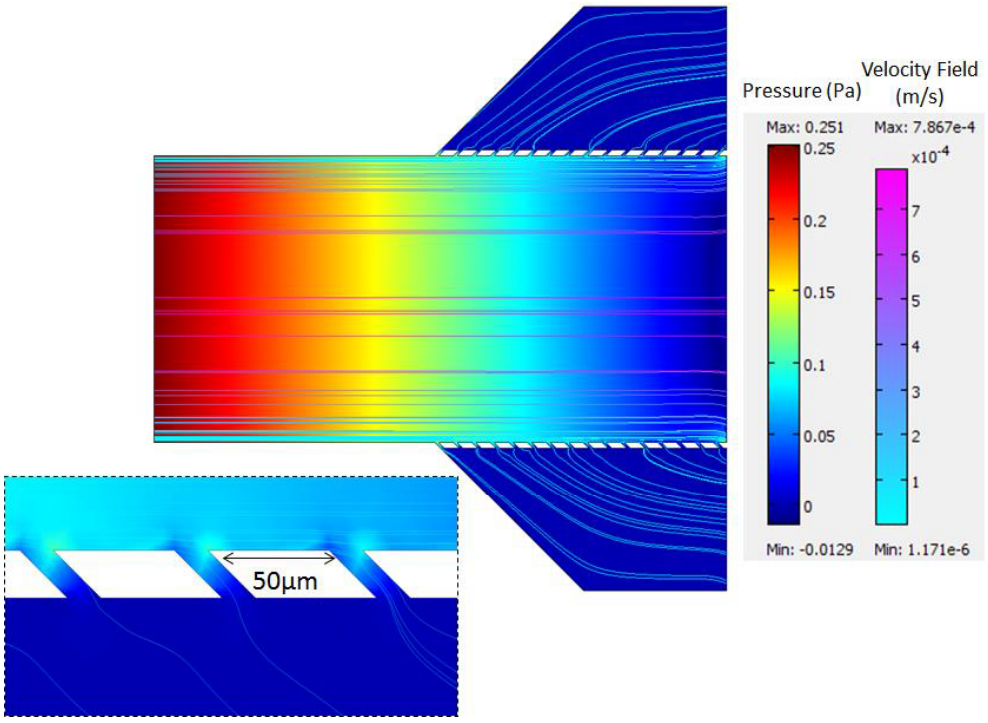

Figure 4.29 2D hydrodynamic flow simulation – 1000 µm main channel width, 45° gap angle, 50 µm wall length, 20 µm wall depth.

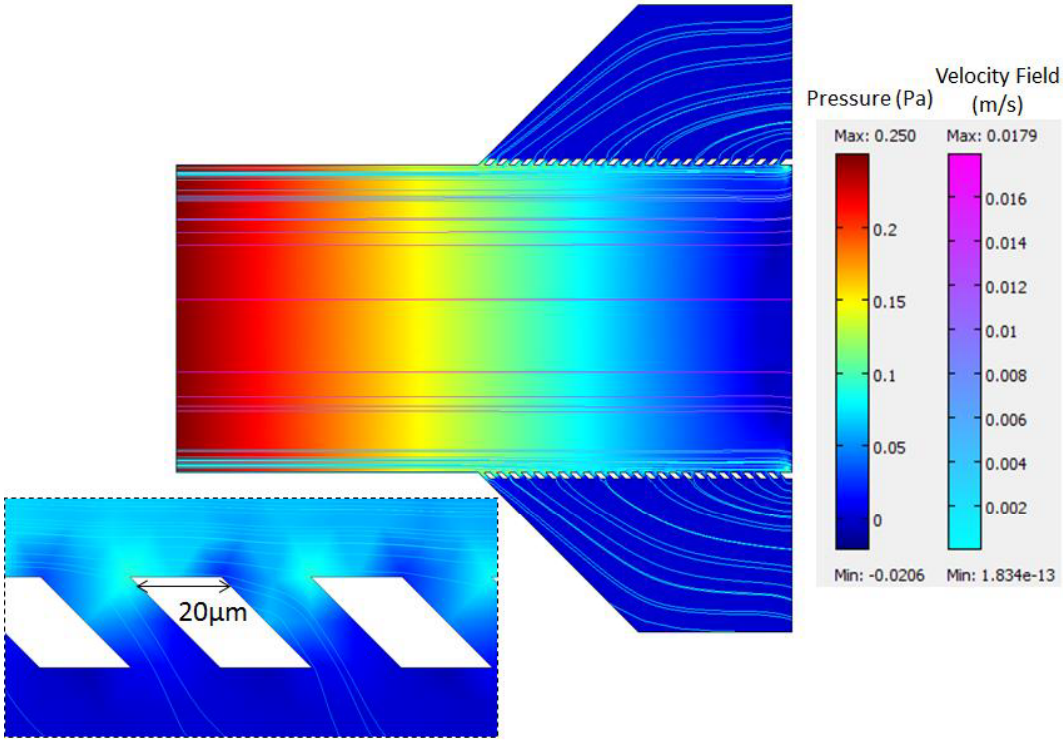

Figure 4.30 2D hydrodynamic flow simulation – 1000 µm main channel width, 45° gap angle, 20 µm wall length, 20 µm wall depth.

Lastly, as an alternative to 20 µm wall depth, 100 µm wall depth was simulated and velocity field drops were compared. Figure 4.31 shows the 100 µm wall depth simulation.

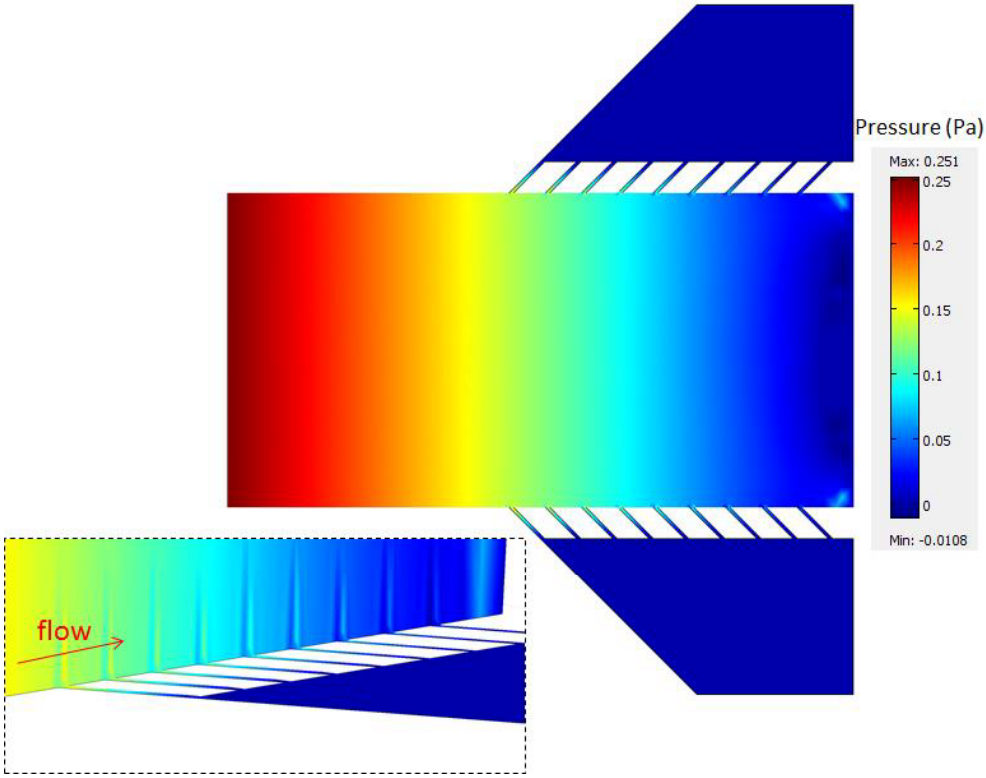

Figure 4.31 2D hydrodynamic flow simulation – 1000 µm main channel width, 45° gap angle, 20 µm wall length, 100 µm wall depth.

Due to the increase in the depth, velocity field decreases much more than 20 µm wall depth simulation. Hence, it was decided to fabricate 20 µm wall depth instead of the 100 µm.

CHAPTER 5

FABRICATION

This chapter presents fabrication steps of the all three generations of DEP microchannel devices, including fabrication flows, mask drawings in the Cadence Layout Editor, and fabricated device images.

The devices were fabricated with surface micromachining techniques. All microchannels were made of Parylene-C and all electrodes were made of gold. The designs of 1st and 2nd generation devices were fabricated on 4" wafers and the 3rd generation device designs were fabricated on 6" wafers for the first time in our research group.

5.1 Fabrication of the 1st Generation Devices

1st generation device fabrication is a three mask process and it consists of metal sputtering, wet and dry etching, photolithography, and Parylene-C coating steps. Fabrication steps in details are given in Appendix B as Table B.1. Figure 5.1 presents the whole fabrication process for the 1st generation devices.

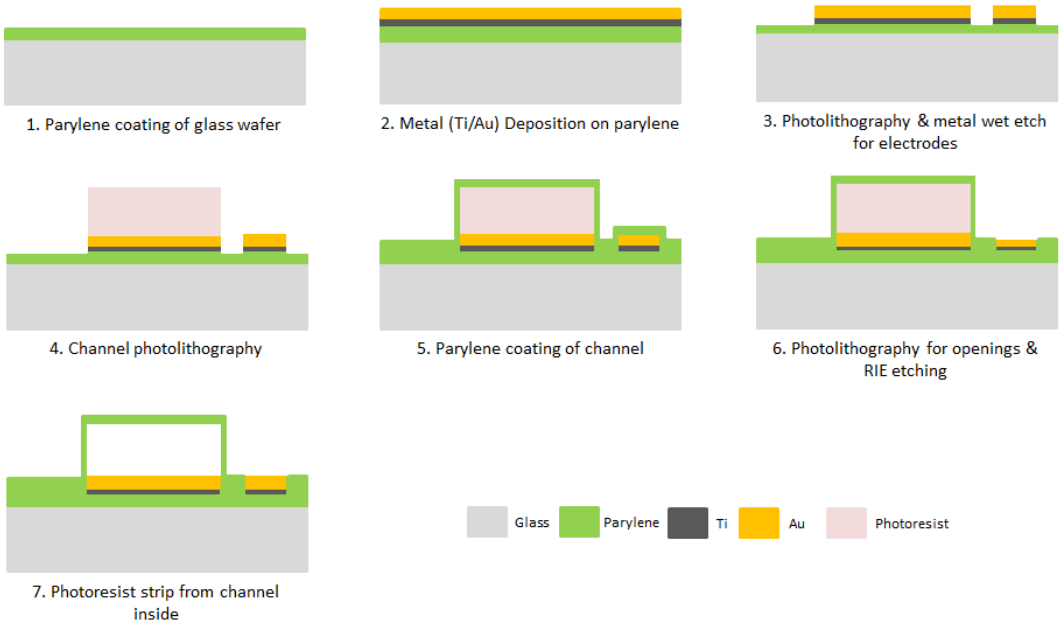

Figure 5.1 The fabrication flow of 1st generation devices.

Fabrication was started with dehydration of the 4" glass wafers which were precleaned with piranha and etched with BHF. After that, parylene coating (5 µm) was made with silane. To get a 5 µm parylene coating thickness, 10g Parylene-C was used in SCS PDS2010 Labcoter device (the amount of Parylene-C to be used is optimized as two times the desired thickness, in g).

After parylene coating step, Ti (30 nm) & Au (400 nm) were sputtered on the wafer. Ti is used as an adhesive layer for Au. Then, these metal layers were patterned by 1st mask (clear field) shown in Figure 5.2, utilizing S220-3 positive photoresist. The aim of using S220-3 positive photoresist is not to lose sharpness of electrode edges during wet etching of metals. Wet etching of Ti & Au layers were made with Ti etchant, consisting of Hydrofluoric acid (HF), Hydrogen peroxide (H_2O_2) and DI water (H_2O), and Aqua Regia, consisting of Hydrogen chloride (HCl) and HNO_3 (Nitric oxide). Figure 5.3 presents the planar electrode structures.

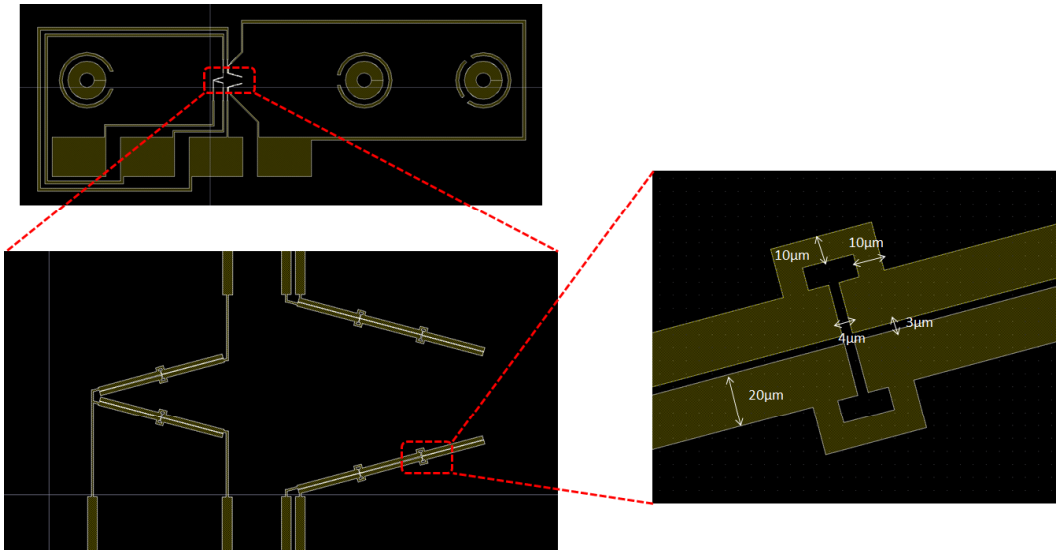

Figure 5.2 1st mask layer of the 1st generation devices.

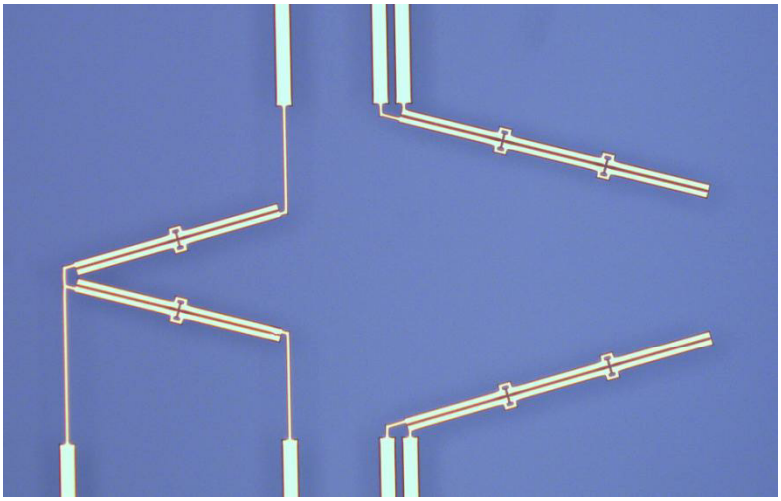

Figure 5.3 The image of planar electrodes after wet metal etching step.

The microchannel, inlets, and outlets were patterned with 2nd mask (clear field), utilizing AZ9260 positive photoresist (as double spin). Double spin process of AZ9260 is applied because of the need for reaching 40 µm height for the microchannel. Then, for the wall formation of microchannel, a second Parylene-C coating which has 20 µm thickness was done (Figure 5.4).

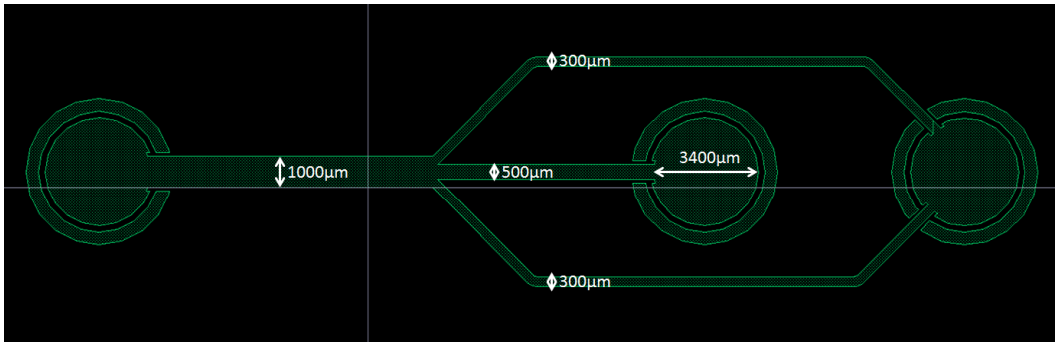

Figure 5.4 2nd mask layer of the 1st generation devices.

After microchannel structure fabrication, openings for contact pads, inlet and outlet reservoirs were formed with reactive ion etching (RIE). Figure 5.5 shows the 3rd mask layer (dark field) applied for RIE. For a proper parylene RIE process for 20 µm depth, 3x20 min RIE application is needed. Finally, each wafer was diced and 10 devices were obtained per one 4" wafer.

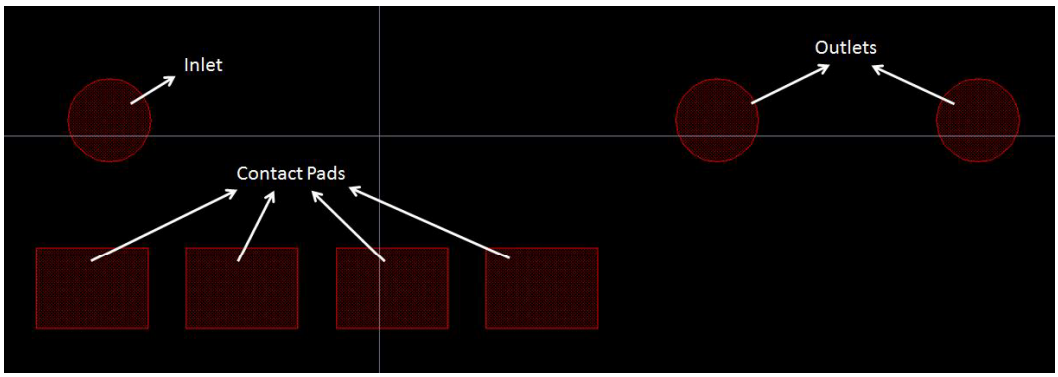

Figure 5.5 3rd mask layer of the 1st generation devices.

After dicing, each device was inserted into acetone for 2-3 days to strip the photoresist, used as sacrificial layer. Figure 5.6 presents the fabricated device.

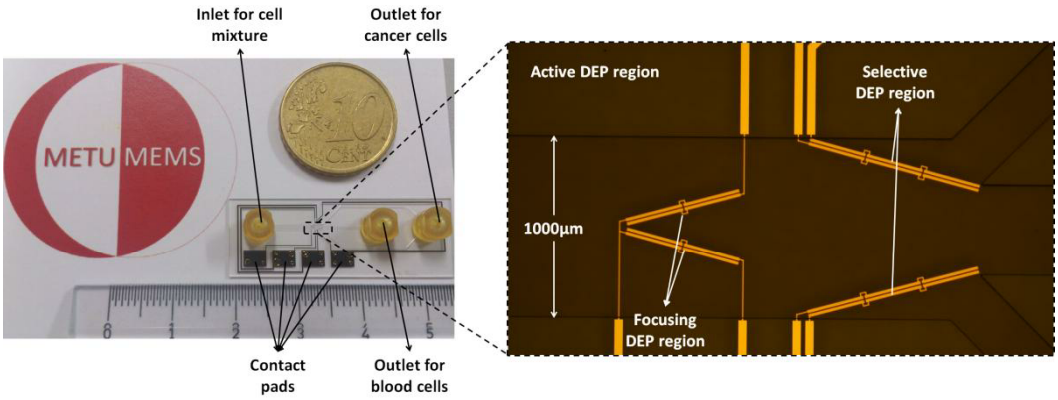

Figure 5.6 Fabricated device for the 1st generation.

5.2 Fabrication of the 2nd Generation Devices

2nd generation device fabrication is similar to the 1st generation device fabrication. It has the same three masks and consists of metal sputtering, wet and dry etching, photolithography and Parylene-C coating steps. Only difference is adding one more step after wet etch of electrodes in the fabrication process. This step is 0.5 µm Parylene-C coating of the electrodes to prevent electrolysis. All related parameters are given in Appendix B as Table B.2. Figure 5.7 presents the whole fabrication process and Figure 5.8 shows electrodes after 0.5 µm Parylene-C coating.

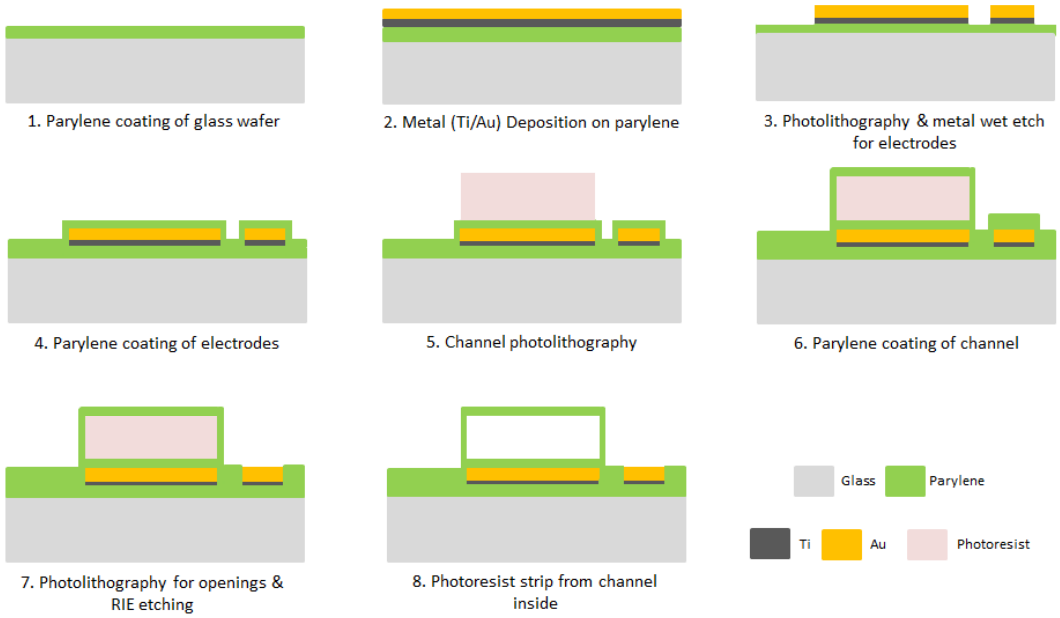

Figure 5.7 Fabrication flow of the 2nd generation devices.

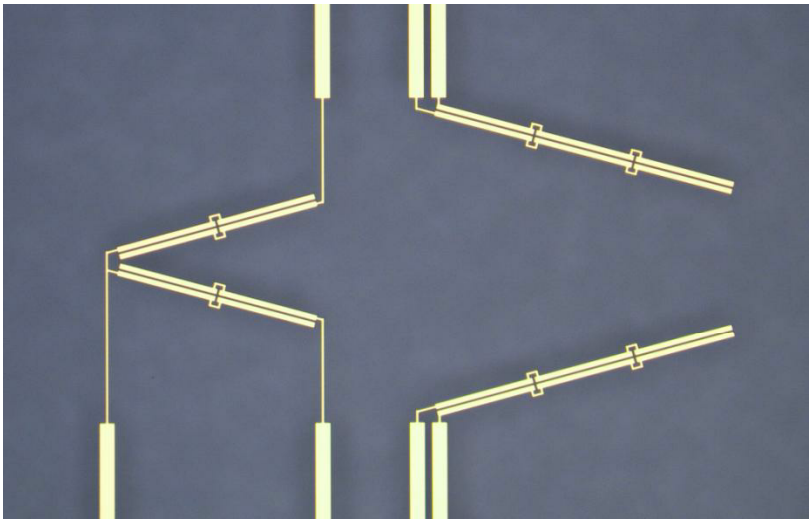

Figure 5.8 Electrodes of the 2nd generation devices after 0.5 μm Parylene-C coating.

5.3 Fabrication of the 3rd Generation Devices

3rd generation device fabrication differs from the previous fabrications due to new design idea of filtration through microchannel walls and 6" wafer sizes. New 7" masks were designed to fabricate 3rd generation devices. Fabrication processes including metal sputtering, wet and dry etching, photolithography and Parylene-C coating steps were applied similar to the 2nd generation device fabrication. Fabrication steps in details are given in Appendix B as Table B.3.

3rd generation includes two different alternative designs, but these alternatives have similar fabrication flows. Figure 5.9 presents the fabrication processes for 3rd generation devices.

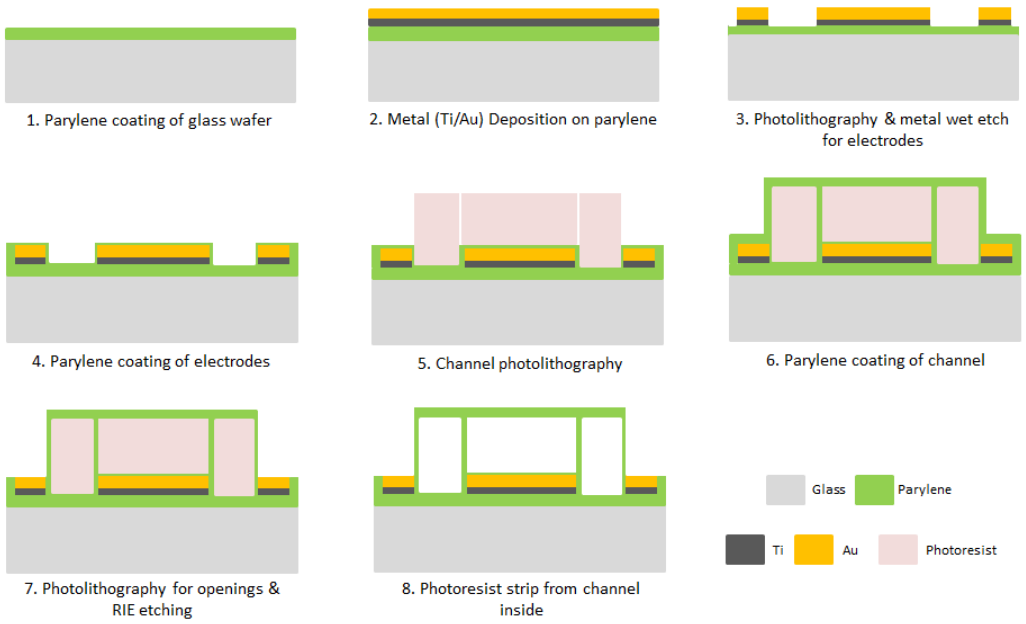

Figure 5.9 Fabrication flow of the 3rd generation devices.

3rd generation device fabrication was started with dehydration of the 6" glass wafers which were precleaned with piranha and etched with BHF. After that, parylene coating (5 μm) was made with silane. Then, Ti (30 nm) & Au (400 nm) metal coatings were applied. Later, these metal layers were patterned by 1st mask (clear field) shown in Figure 5.10 and Figure 5.11, utilizing S220-3 positive

photoresist. Wet etching of Ti & Au layers were again made with Ti etchant and Aqua Regia. Figure 5.12 presents the planar electrode structures of 3rd generation devices.

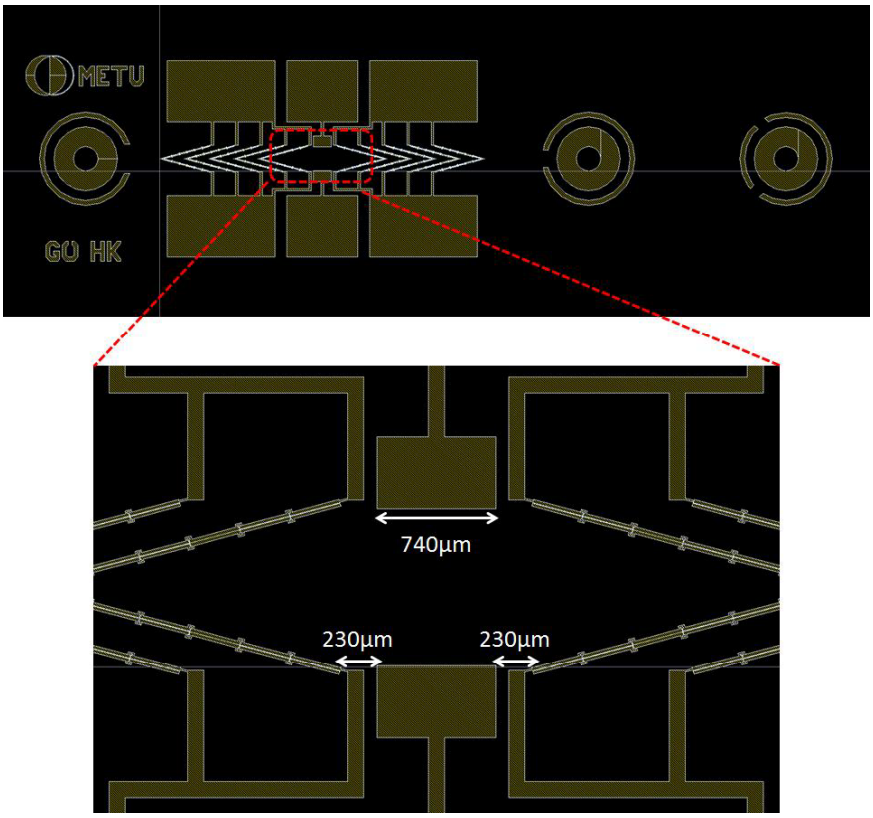

Figure 5.10 1st mask layer of the 3rd generation devices – grounded version.

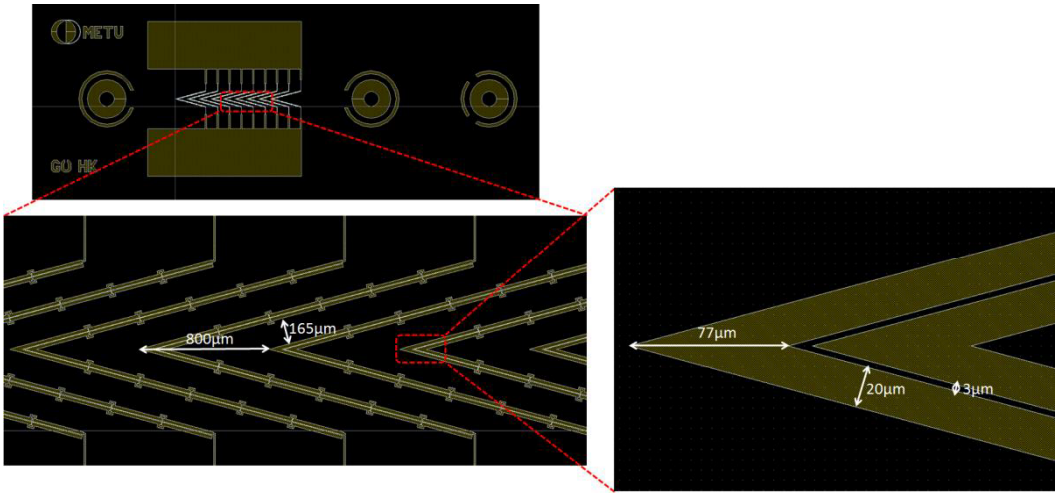

Figure 5.11 1st mask layer of the 3rd generation devices – gapped version.

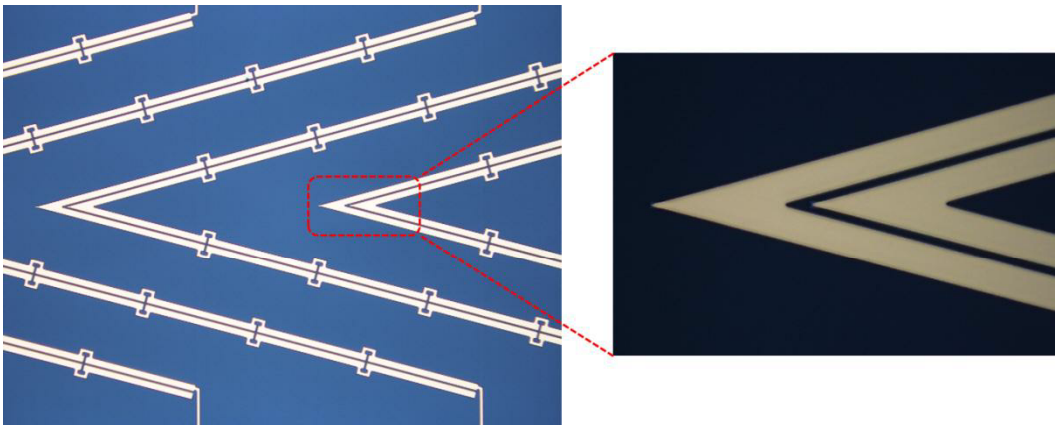

Figure 5.12 The image of planar electrodes after wet metal etching step.

Some of the devices in the 1st mask of the 3rd generation (both grounded and gapped) were drawn by means of having asymmetrical electrodes for increasing the cell manipulation efficiency. Asymmetry was created by shifting the electrode pairs (beginning from the second pair) +20 µm and -20 µm on 500 µm level (microchannel center) in y direction, respectively. Figure 5.13 shows these asymmetrical electrode shapes in the 1st mask including distances.

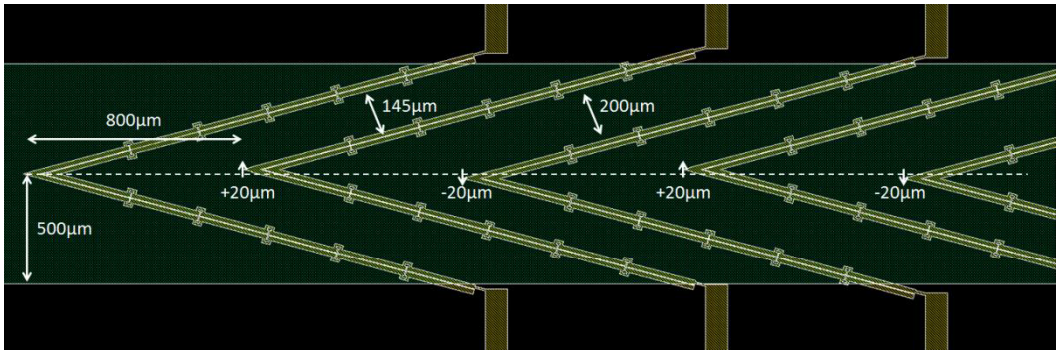

Figure 5.13 Asymmetrical electrodes drawn for 3rd generation devices.

The microchannel, inlets and outlets were patterned with 2nd mask (clear field), utilizing AZ9260 positive photoresist (as single spin) shown in Figure 5.14 and 5.15. Single spin process of AZ9260 is applied because of the need for reaching 20 µm height for the microchannel. Then, for the wall formation of microchannel, a second Parylene-C coating which has 20 µm thickness was done.

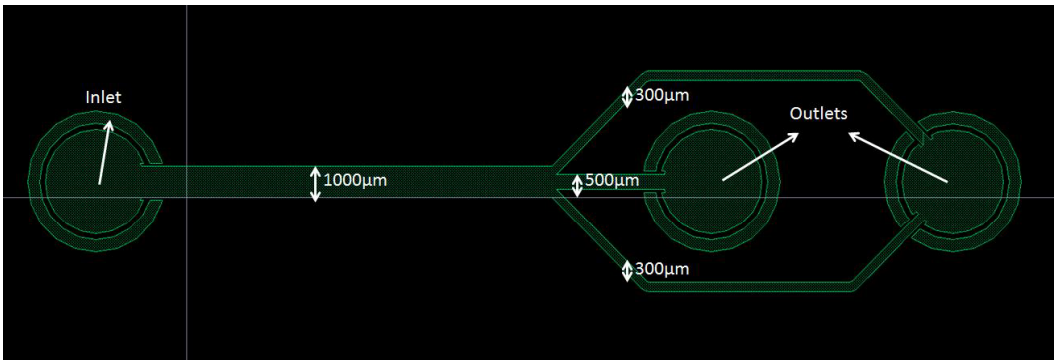

Figure 5.14 2nd mask layer of the 3rd generation devices – grounded version.

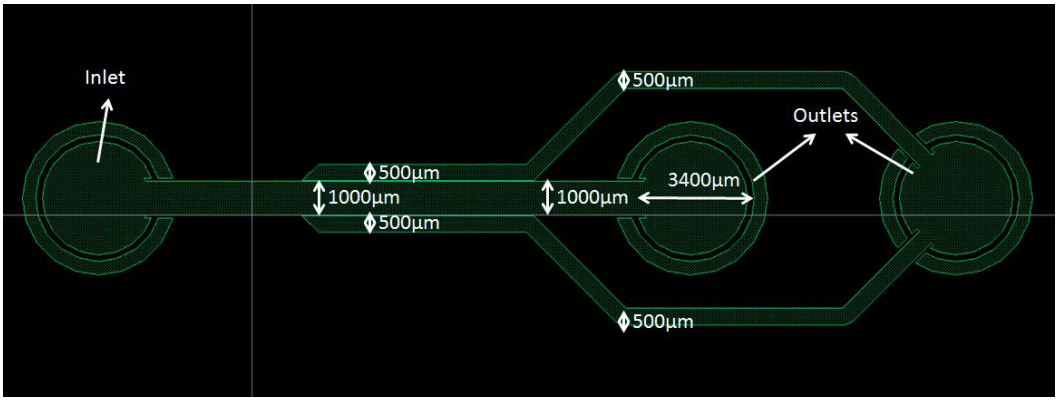

Figure 5.15 2nd mask layer of the 3rd generation devices – gapped version.

After microchannel structure fabrication, openings for contact pads, inlet and outlet reservoirs were formed with reactive ion etching (RIE). Figure 5.16 and 5.17 show the 3rd mask layer (dark field) applied for RIE. Finally, each wafer was diced and 32 devices were obtained per one 6" wafer.

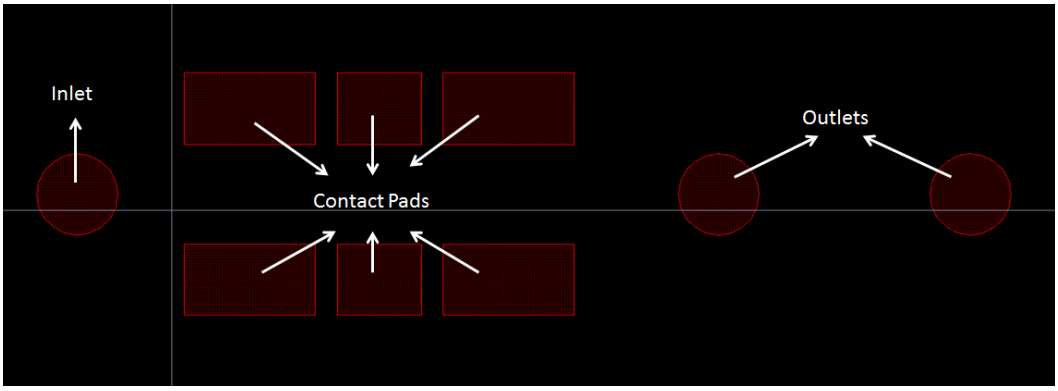

Figure 5.16 3rd mask layer of the 3rd generation devices – grounded version.

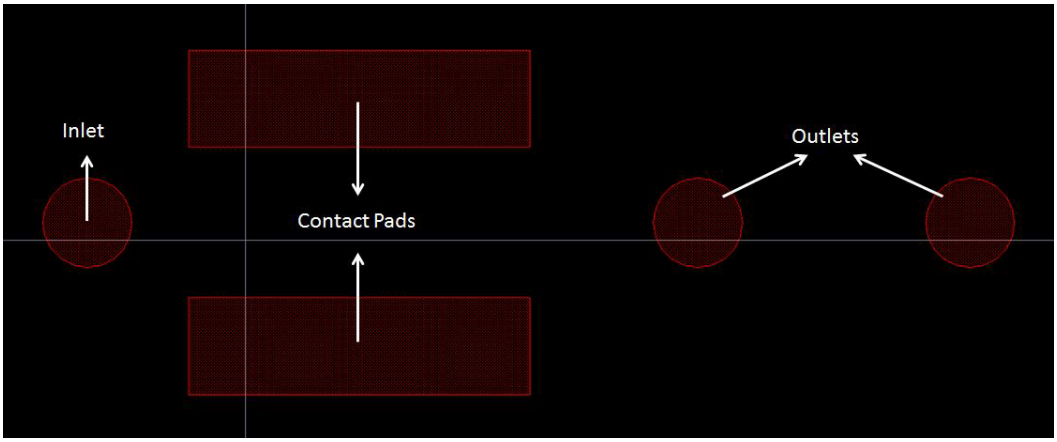

Figure 5.17 3rd mask layer of the 3rd generation devices – gapped version.

After dicing, each device was inserted into acetone for 2-3 days to strip the photoresist, used as sacrificial layer. Figure 5.18 and 5.19 present the fabricated devices.

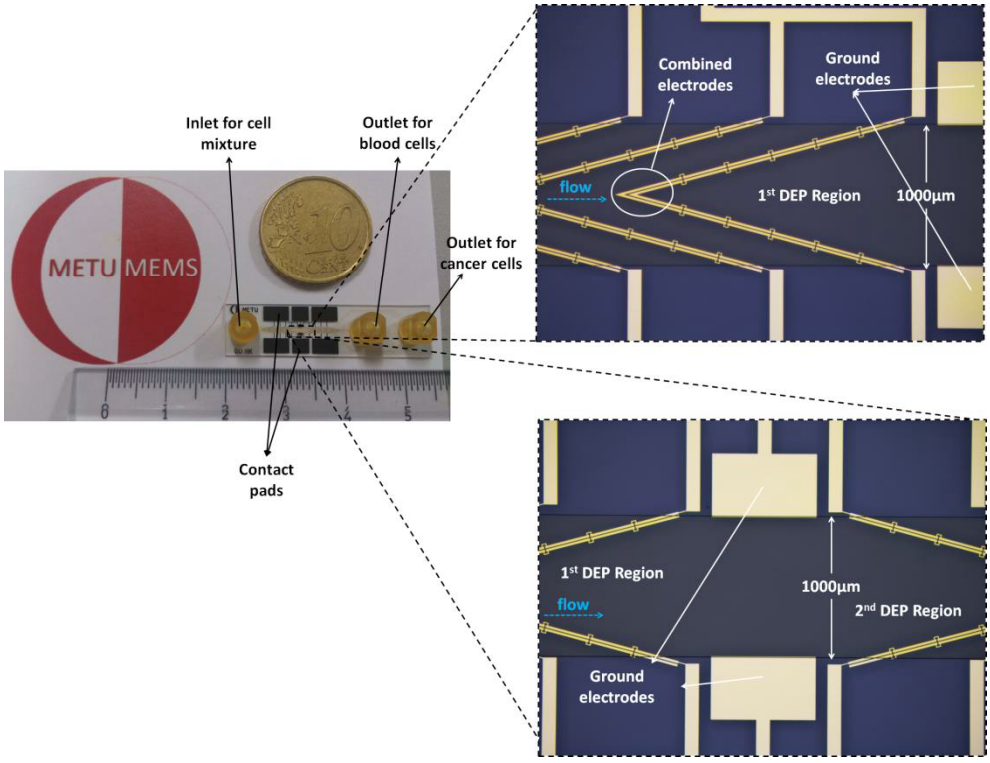

Figure 5.18 Fabricated device for the 3rd generation – grounded version.

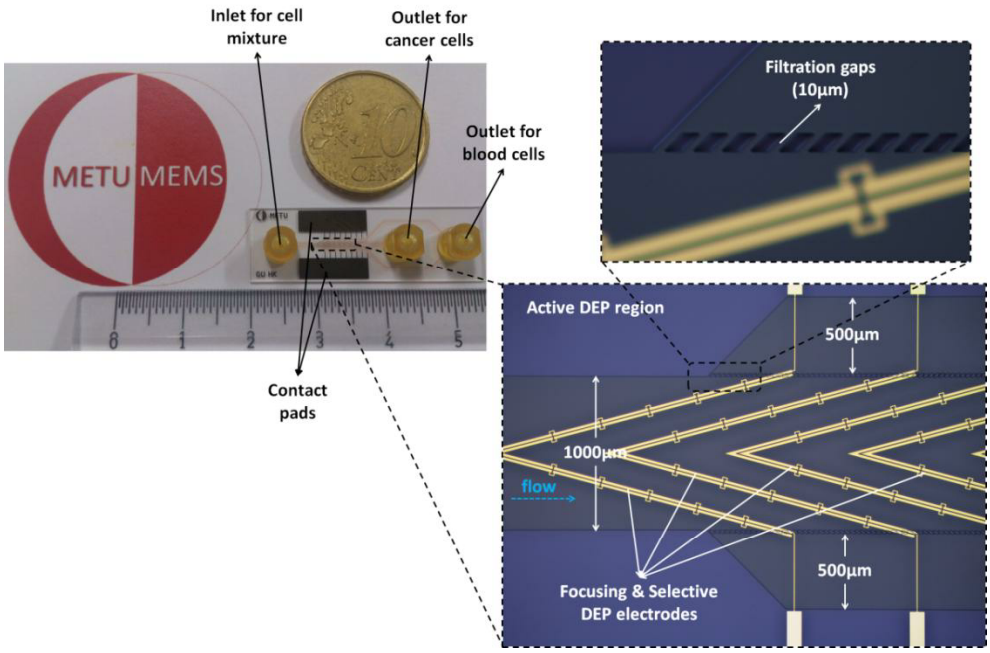

Figure 5.19 Fabricated device for the 3rd generation – gapped version.

CHAPTER 6

RESULTS AND DISCUSSION

This chapter includes the experimental results on the DEP devices. In the first part, preparation steps for the cells were presented. Second part includes experimental setup. Test results of the 1st generation devices were presented in the third part. Then, test results of the 2nd and 3rd generation devices were explained in the fourth and fifth parts, respectively.

6.1 Preparation of the Cells

For the testing of DEP devices, RBCs, K562 cells and MCF7 cells were prepared, applied to the microchannels and then results were obtained.

Whole blood samples were collected in 3 ml tubes including 3.6 mg K_3EDTA from the peripheral blood vessels of healthy volunteers in Medical Center, METU. To extract RBCs, centrifugation was done with Sigma 4-96KS centrifuge at 600g RCF for 10 min. After centrifugation, different ratios of dilutions were done on RBCs to get the required amounts for testing.

For the monitoring purposes of RBCs inside the microchannel, no staining was used for the single cell type tests because of the natural red colors of RBCs under bright field, but when cell mixture tests were done, RBCs were stained with CellTracker™ Red to observe them under fluorescent microscope equipped with 31002 TRITC, Chroma filter.

K562 cells were cultured in RPMI 1640 medium containing 10% (w/v) fetal bovine serum (FBS) and 0.2% (w/v) gentamicin, at 37 °C with 5% CO_2 in humidified incubator in the Department of Biology, METU. Before each tests,

cells were washed twice with the DEP medium which has a conductivity of 10 mS/m. This medium contained 8.5% (w/v) sucrose and 0.3% (w/v) dextrose to adjust osmotic pressure inside the cell. Besides, cells were counted using hemocytometer and the cell concentrations were adjusted accordingly.

For the monitoring purposes of K562 cells inside the microchannel, fluorescein diacetate (FDA), a fluorescent dye used to stain live cells, was applied. FDA was dissolved in DMSO (10 μg/ml) and 2.5 μl of it was used to stain 10^6 cells. After staining procedure, cells were observed as green under fluorescent microscope with GFP filter.

The same procedure was applied to MCF7 cells to observe MCF7 movements under fluorescent microscope.

6.2 Experimental Setup

For the enrichment of rare cells (K562s and MCF7s) from RBCs, continuous flow analyses were carried out in Class 10.000 Clean Room, in Electrical and Electronics Engineering Department, METU. The test setup is shown in Figure 6.1. To adjust the flow rate, a programmable syringe pump (Lab Smith) and its software (μProcess Scanner) were used with 80 μl syringe. Observations were carried out under 8x magnification with a fluorescent microscope (Olympus SZX12). A monochromatic high-speed camera (Photometrix Evolve 128) was utilized to observe the cell movements inside microchannel under continuous flow and low fluorescence intensity. Real-time processing of screenshots was carried out with the computer software, Winfluor to get green and red images. DEP force was generated by energizing the electrodes with a signal generator (Agilent, 81150A). All of its four outputs were utilized with 180° phase difference (two by two) for 1^{st}, 2^{nd} and 3^{rd} generation (grounded) DEP devices and two of four outputs were utilized with 180° phase difference for the 3^{rd} generation (gapped) DEP devices.

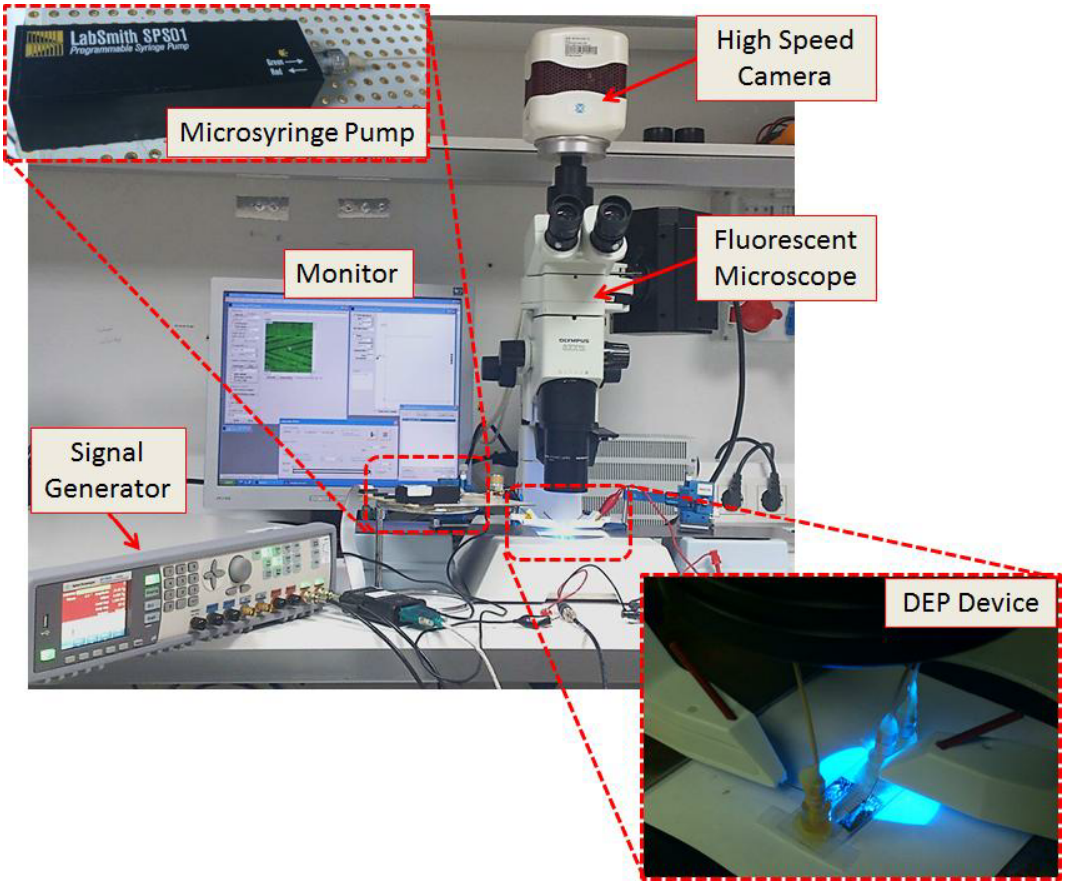

Figure 6.1 Experimental setup used for testing the DEP devices.

6.3 Test Results

6.3.1 Test Results for the 1st Generation DEP Devices

1st generation devices were tested after fabrication for the proof of nDEP manipulation idea with the frequencies which were decided by MATLAB graph in Figure 3.5. Initial tests were done by application of 5 kHz to first DEP region and 26.3 kHz to second DEP region. Figure 6.2 shows the microchannel and electrodes before activation of electrodes.

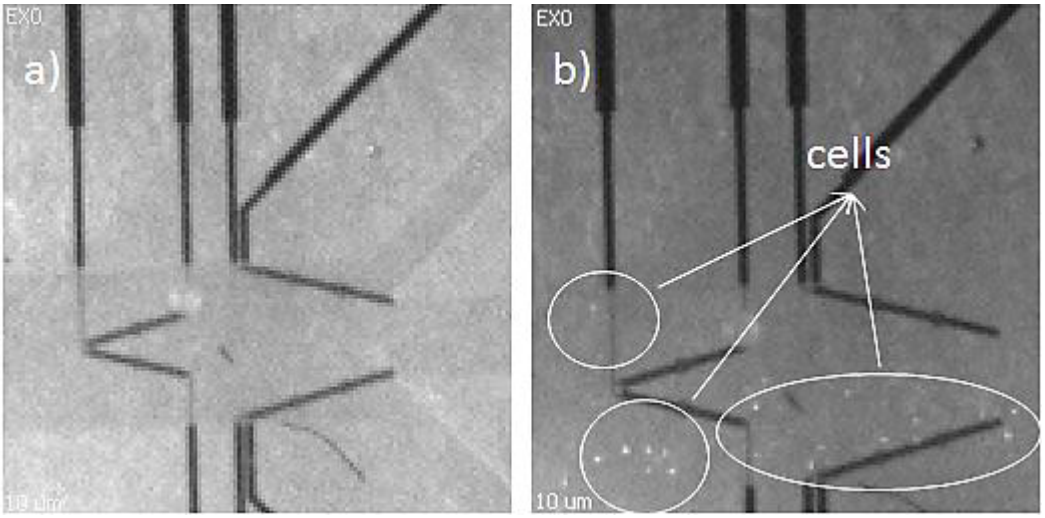

Figure 6.2 1st generation device microchannel and electrodes a) without cells and b) with cells (no flow).

In addition to nDEP frequencies, pDEP frequencies were also tested on these 1st generation devices. Figure 6.3 shows the K562 movements in the microchannel due to nDEP and pDEP.

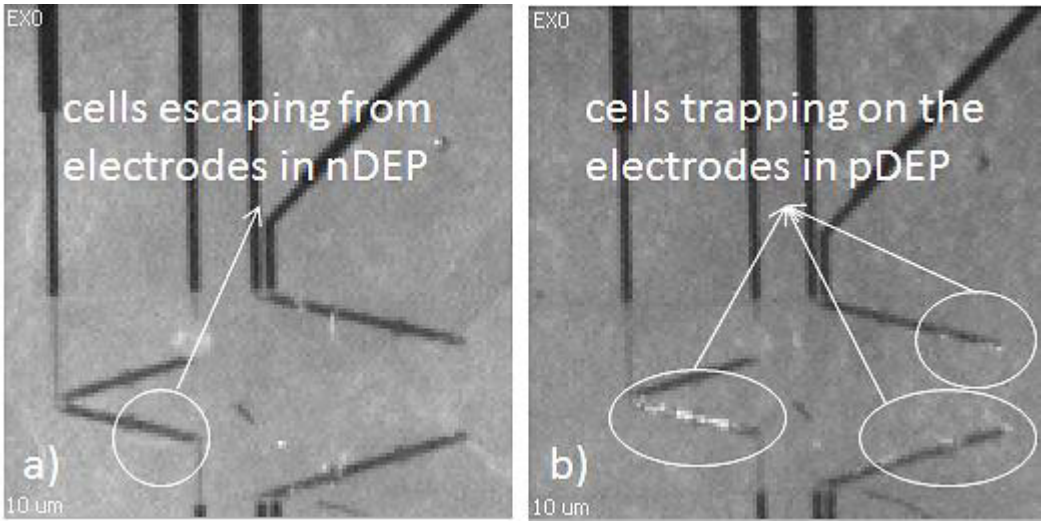

Figure 6.3 K562 cancer cell movements in the microchannel (flow = 1 µl/min, voltage = 20 V_{pp}, frequency = 5 kHz & 1 MHz) a) nDEP effect on K562 cancer cells (escaping) b) pDEP effect on K562 cancer cells (trapping).

During tests, air bubble formations on the electrodes were observed. Air bubble formation speeds changed depending on the applied frequency. Frequencies at kHz levels, which are nDEP frequencies, caused air bubble formations on the electrodes slowly. In comparison to this, frequencies at MHz levels which are pDEP frequencies, caused rapid air bubble formations around electrodes. Because of the air bubble formations on the electrodes, cells could not flow properly in the microchannel and DEP operations were prevented. Figure 6.4 shows the air bubble formation in the microchannel due to activation of electrodes.

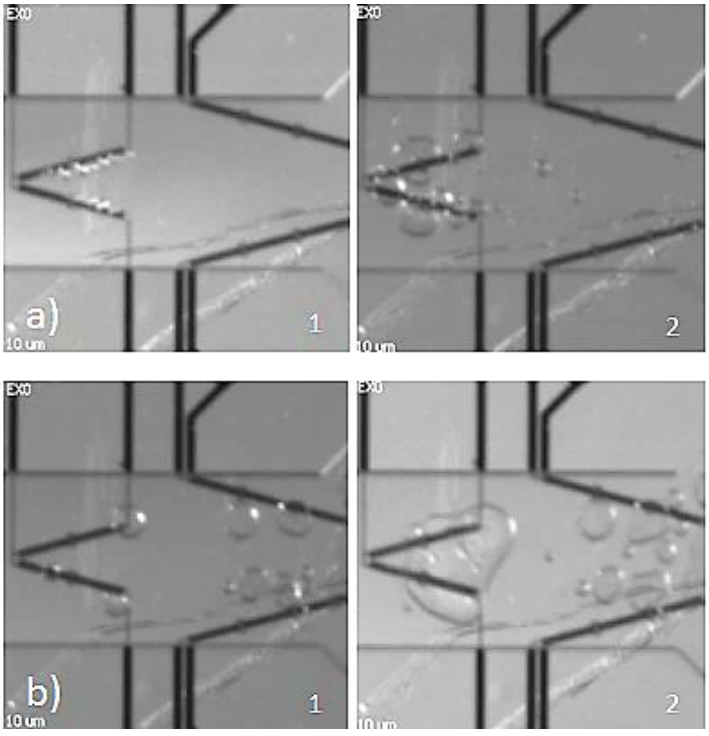

Figure 6.4 Air bubble formation on the electrodes (no flow, voltage = 10 V_{pp}, frequency = 5 kHz) a) only first electrode region is active b) both electrode regions are active.

The air bubbles form due to electrolysis. Planar gold electrodes are directly in contact with the liquid medium in the microchannel. There is no insulation layer between electrodes and medium. When the images from metal etching step were checked carefully, it was seen that Aqua Regia, which was used as Au etchant during fabrication of the devices overetched the gold parts of electrodes and Ti

parts, which lie under the Au as an adhesive layer were directly in contact with the medium. Electrocatalytic oxidation of Ti occurred and this reaction caused bubbles on the contacting areas of Ti.

6.3.2 Test Results for the 2nd Generation DEP Devices

In order to prevent air bubble formations in the microchannels of the 1st generation DEP devices, a thin (0.5 μm) insulating Parylene-C layer coating on the electrodes was added to the fabrication of the 2nd generation DEP devices. As shown in Figure 6.5, this has prevented the air bubble formation around the activated electrodes.

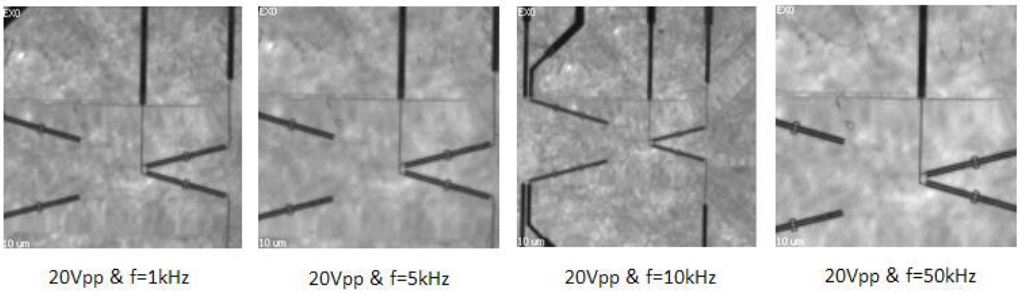

Figure 6.5 No air bubble formation on thin Parylene-C coated electrodes activated with different frequencies at 20 V_{pp}.

After preventing air bubble formations on the electrodes, tests were continued for the manipulation of the cells via nDEP force. RBCs and K562s were tested individually.

Figure 6.6 and 6.7 presents the RBC manipulations via the nDEP force at 20V_{pp}, at 5 kHz and 26.3 kHz, respectively. Flow rates were adjusted between 0.1 – 1 μl/min. At both frequencies, RBCs observe nDEP force. Some air bubbles are seen in the images because of pumping of the syringe. These air bubbles which are formed during cell mixture suction to the syringe reservoir, were firstly located at the inlets of the microchannels, flowed through the microchannel and remained stable at some regions because of low flow rates.

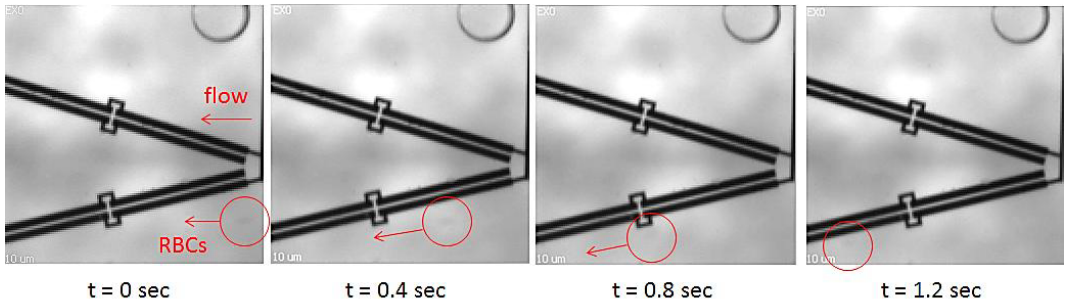

Figure 6.6 RBC manipulation with nDEP at $20V_{pp}$ & 5 kHz at 0.5 µl/min flow rate.

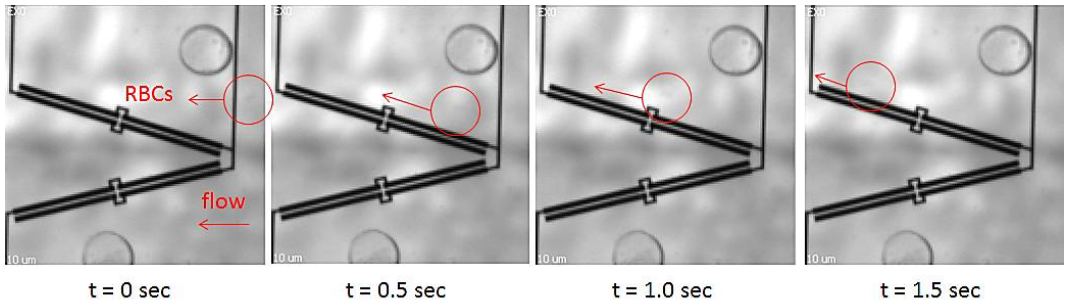

Figure 6.7 RBC manipulation with nDEP at $20V_{pp}$ & 26.3 kHz at 0.5 µl/min flow rate.

Figure 6.8 and 6.9 presents the K562 manipulations due to the nDEP force at $20V_{pp}$, at 5 kHz and 26.3 kHz, respectively. Flow rates were adjusted between 0.1 – 1 µl/min. Manipulation of K562s occurs at 5 kHz frequency (can be seen in Figure 6.8 as three individual cells), but 26.3 kHz is the crossover frequency of K562 cells, at which they onbserve no DEP force as seen in Figure 6.9.

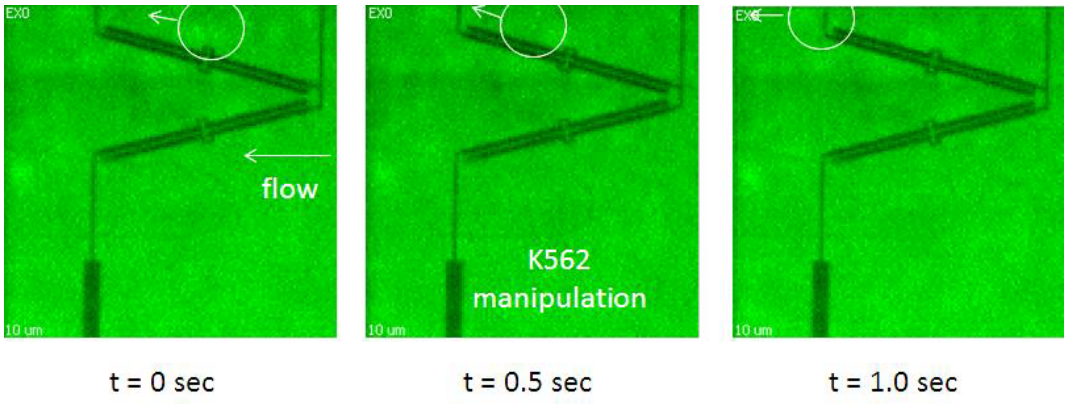

Figure 6.8 K562 manipulation with nDEP at $20V_{pp}$ & 5 kHz at 0.5 µl/min flow rate.

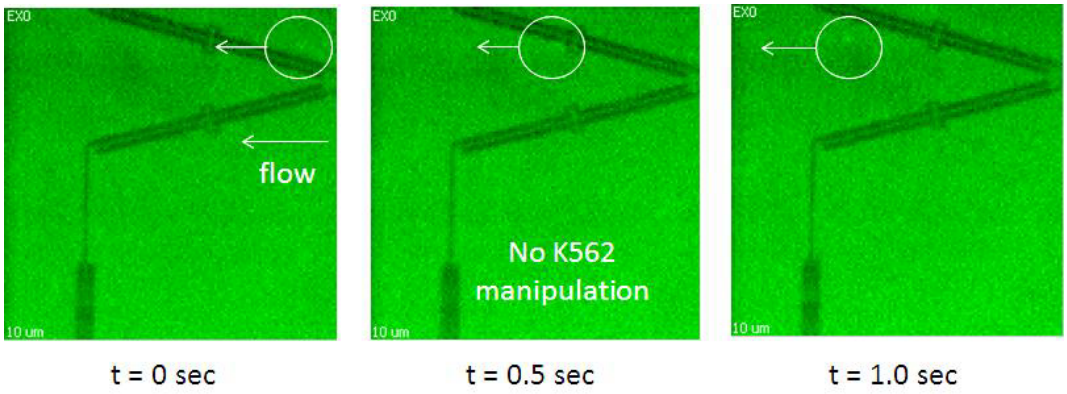

Figure 6.9 K562 manipulation with nDEP at $20V_{pp}$ & 26.3 kHz at 0.5 µl/min flow rate.

Although simulations present nDEP force can manipulate cells with 18 µl/min flow rate, experiments has shown that cells cannot be manipulated over 1 µl/min flow rates in these microchannels. Low flow rates increase the process duration, which is undesirable.

After the trials of nDEP frequencies, pDEP frequencies such as 1 MHz were applied to the cells in 20 V_{pp} to check the cell trapping on the planar electrodes. Cell reactions were astonishing at high flow rates such as 20 µl/min and 30 µl/min. Instead of trapping on the electrodes, cells started to slide on the electrodes over 20 µl/min flow rates. Figures 6.10 and 6.11 represent K562 cells tested with 20 µl/min and 30 µl/min flow rates, respectively.

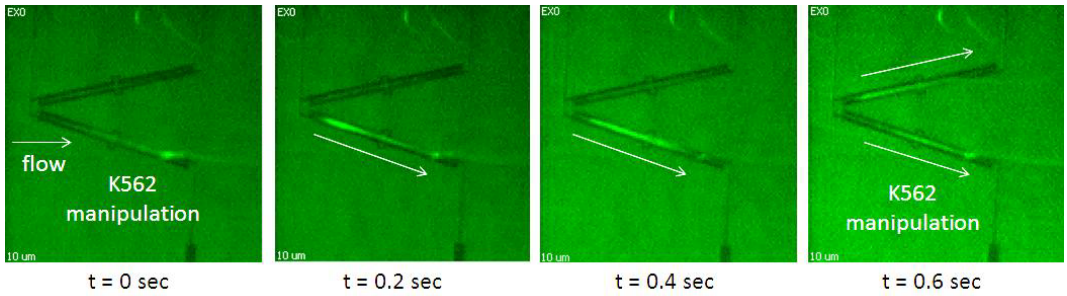

Figure 6.10 K562 manipulation with pDEP at 20V_{pp} & 1 MHz at 20 µl/min flow rate.

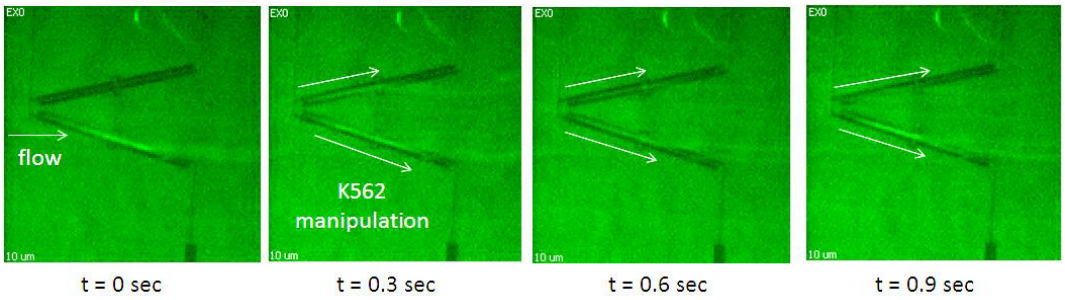

Figure 6.11 K562 manipulation with pDEP at 20V_{pp} & 1 MHz at 30 µl/min flow rate.

Due to the successful cell movements on the planar electrodes by applying high flow rates (20 – 30 µl/min) in comparison to nDEP flow rates (0.1 – 1 µl/min), pDEP application was chosen for the manipulation of the cells and enrichment of rare cells from blood.

During 2nd generation DEP device tests, many cell escapes from the open parts of V-shaped electrodes, decreasing the device efficiency. Besides, 2nd generation DEP devices were designed for applying nDEP forces for the cell manipulations

and collateral electrode numbers were not enough to manipulate the cells to the desired regions in pDEP. For these reasons, 3rd generation devices were designed and fabricated.

6.3.3 Test Results for the 3rd Generation DEP Devices

3rd generation devices were designed, simulated, fabricated and tested by taking drawbacks of 2nd generation DEP devices into consideration.

Two alternatives, named as grounded and gapped devices were tested for cell manipulation capacities under pDEP forces. For the testing of grounded version, two different frequencies were applied to the focusing and selective DEP microelectrode pairs. 1 MHz frequency was applied for the first DEP region, where all cells were focused towards the walls of the microchannels. Due to ground electrodes between DEP regions, which are activated at different frequencies, crosstalk was prevented. In the second part, which is named as selective DEP region, the crossover frequency of K562 cells was applied. Hence, only RBCs were manipulated to move towards the microchannel center by sliding over the planar electrodes. K562 cells were continued to their undisturbed flow by applying crossover frequencies at the selective DEP region.

For the first tests, K562 cells were applied to the grounded version of the 3rd generation DEP devices and both DEP regions were activated at 1 MHz to observe the cell slide and cell jumps from one electrode pair to another at 20 V_{pp} and 30 μl/min flow rate throughout all electrodes. Figure 6.12 presents the slide and jumps of K562 cells on the electrodes. As it can be seen in the Figure 6.12, some K562 cells were trapped on the electrodes.

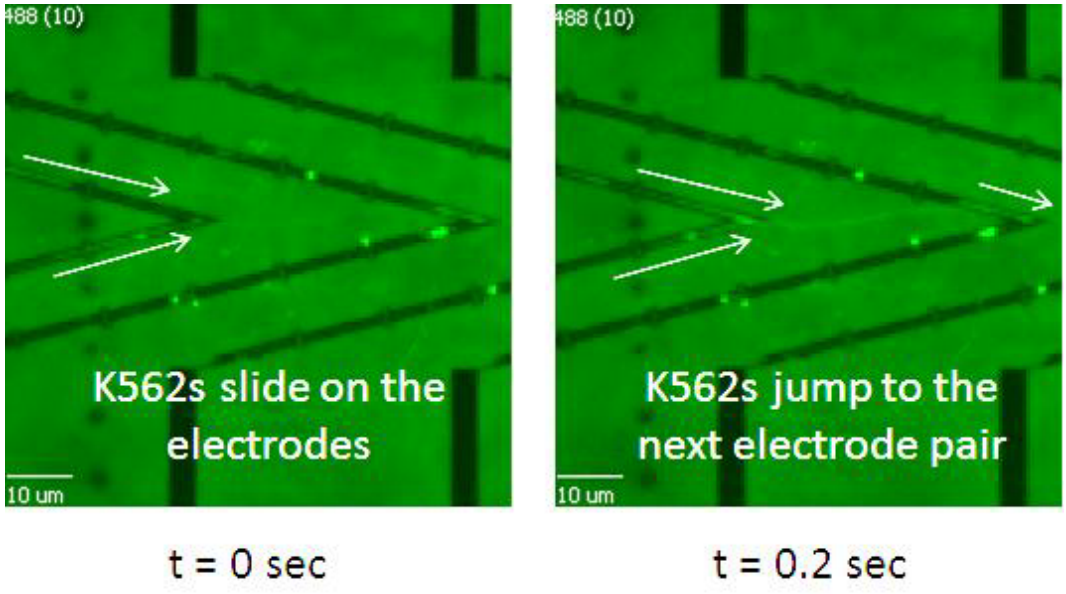

Figure 6.12 K562 cell movements in grounded version of 3rd generation devices at $20V_{pp}$ and 30 µl/min flow rate (1 MHz for both DEP regions).

Trapped rare cells decrease the efficiency of the devices, but this issue can be solved by decreasing the applied electrical potential. Figure 6.13 and 6.14 present K562 cells and RBC manipulations, respectively, at $18V_{pp}$ and 10 µl/min flow rate.

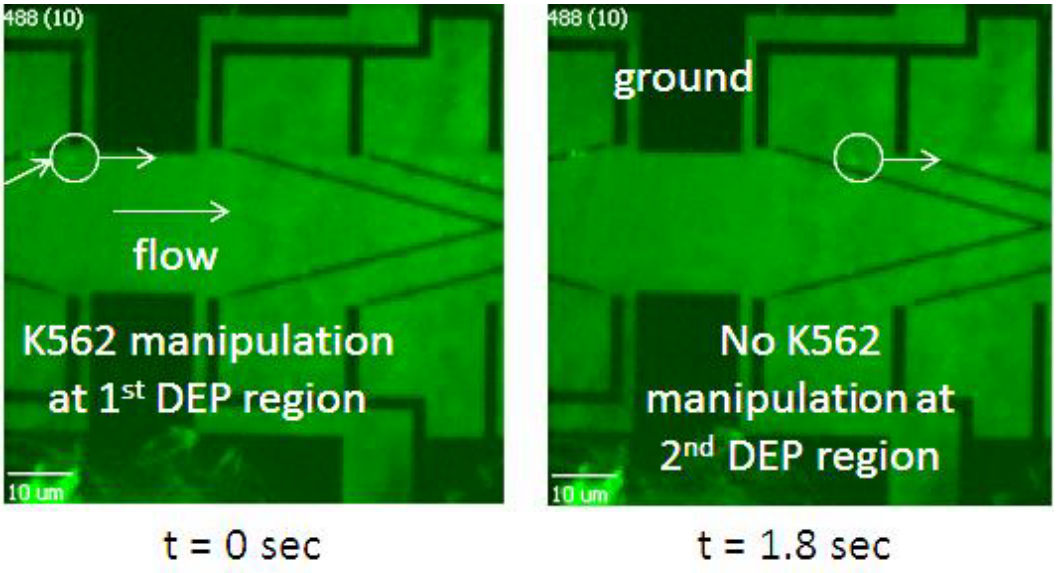

Figure 6.13 K562 cell movements in grounded version of 3rd generation devices at 18V_{pp} and 10 µl/min flow rate (1 MHz for 1st DEP region and 51 MHz for 2nd DEP region).

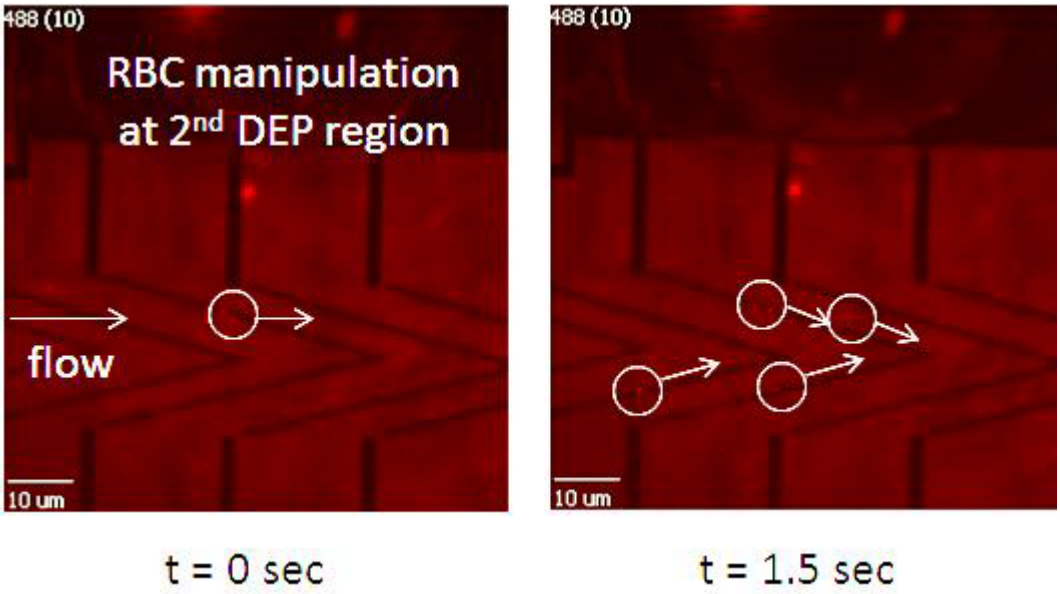

Figure 6.14 RBC movements in grounded version of 3rd generation devices at 18Vpp and 10 µl/min flow rate (1 MHz for 1st DEP region and 51 MHz for 2nd DEP region).

Second alternative of 3rd generation devices, which has filtering gaps on the walls of the main microchannel, were tested with K562 cells. This time, testing procedure became easier because of applying only one frequency to the microelectrodes (1 MHz for pDEP). All planar electrodes function as focusing electrodes and manipulate all cells towards the gaps, K562 cells which have larger sizes, were filtered, while RBCs, which have smaller sizes, pass through the gaps to the side channels, at 20 V_{pp} and 30 µl/min flow rate. Figure 6.15 presents the K562 cell movements on the symmetrical electrodes of gapped version of the 3rd generation devices.

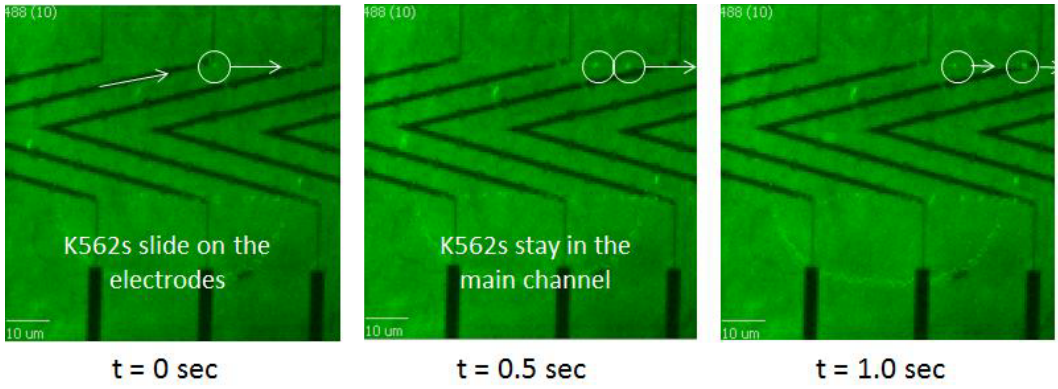

Figure 6.15 K562 cell movements in gapped version of 3rd generation devices with symmetric electrodes at 20Vpp & 1 MHz at 30 µl/min flow rate.

Asymmetric electrodes were then tested with K562 cells & RBCs mixture with 6-million cells/ml concentration (K562 cells / RBCs ratio was 1:5). Figure 6.16 and 6.17 present the RBCs and K562 cells manipulations on the asymmetric electrodes for the gapped version of the 3rd generation DEP devices.

Figure 6.16 RBC movements in the gapped version of 3rd generation devices with asymmetric electrodes, at 20Vpp & 1 MHz at 30 µl/min flow rate.

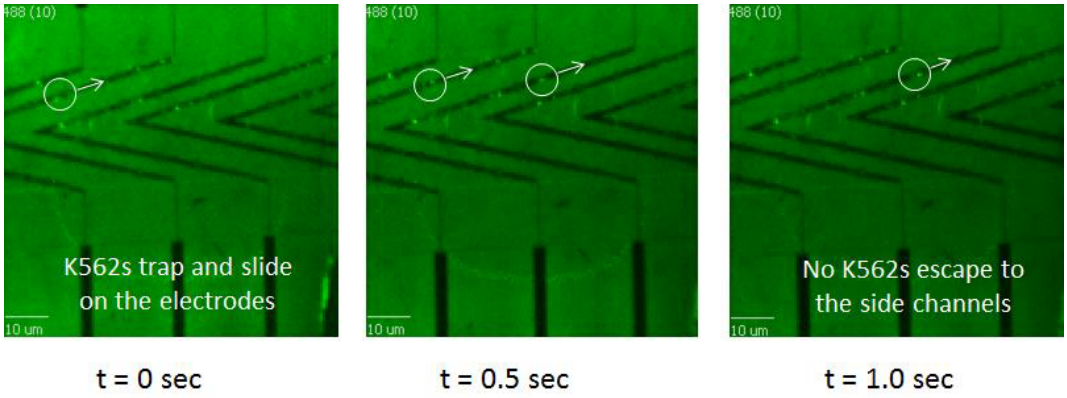

Figure 6.17 K562 cell movements in gapped version of 3rd generation devices with asymmetric electrodes, at 20Vpp & 1 MHz at 30 µl/min flow rate.

6.4 Cell Enrichment Calculations

For the quantification of the efficiency of devices, cell enrichment factor has been calculated by dividing the ratio of cancer cells and RBCs in the cancer cell outlet by that in the inlet (Equation 6.1) [111]:

$$c.e.f._{(cell_1)} = \frac{(cell_1 count/cell_2 count)_{cell_1 outlet}}{(cell_1 count/cell_2 count)_{cell\ mixture\ inlet}} \quad (6.1)$$

Thus, a two-fold enrichment at the cell outlet indicates that the desired cell percentage is doubled at the output relative to the input. For calculation of the cell enrichment factor of the devices, cells were counted in the hemocytometer before

applying to the microchannel and then counted again after taken from cancer outlet.

In addition to cell enrichment factor calculations, recovery rate calculations were done by dividing the amount of cancer cells in the cancer cell outlet by that in the inlet (Equation 6.2) [112]:

$$Recovery\ rate_{(cell_1)} = \frac{(cell_1 count)_{cell_1 outlet}}{(cell_1 count)_{cell\ mixture\ inlet}} \tag{6.2}$$

Firstly K562 cell enrichment is realized in K562 cells & RBCs mixture. Figure 6.18 presents the K562 and RBC counts in cell mixture, measured before injection to the microchannel. To count the cells, 10 µl samples were taken from the cell mixture and counted under fluorescent microscope (Olympus SZX12). For the cell mixture before enrichment, five individual samples were taken and an average value was calculated.

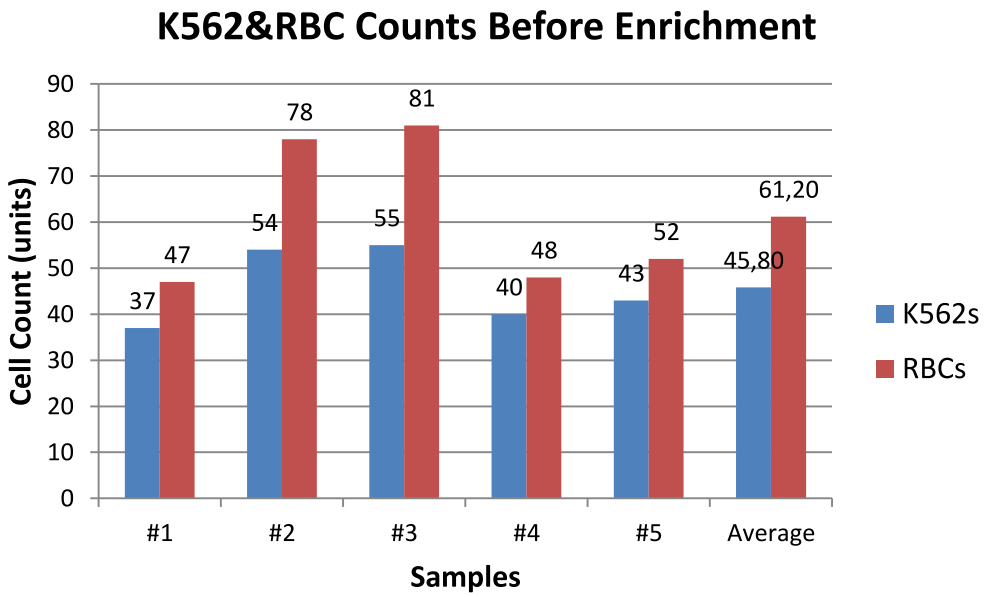

Figure 6.18 K562 and RBC counts from five individual samples before enrichment.

Table 6.1 presents the K562 and RBC ratios in cell mixture before applying to the microchannel.

Table 6.1 K562 & RBC ratios in the cell mixture before enrichment.

	1st sample	**2nd sample**	**3rd sample**	**4th sample**	**5th sample**	**Average**
Ratio of K562 cells to RBCs	0.79	0.69	0.68	0.83	0.83	0.75
Normalized Ratio of K562 cells to RBCs	1:1.27	1:1.44	1:1.47	1:1.20	1:1.20	1:1.33

Figure 6.19 presents the K562 and RBC counts from cancer cell outlet of the device, after enrichment. To count the cells, same steps with previous part were applied. For the cell mixture taken from cancer cell outlet after enrichment, again five individual samples were taken and another average value was calculated. Table 6.2 presents the K562 and RBC ratios in cell mixture taken from cancer cell outlet.

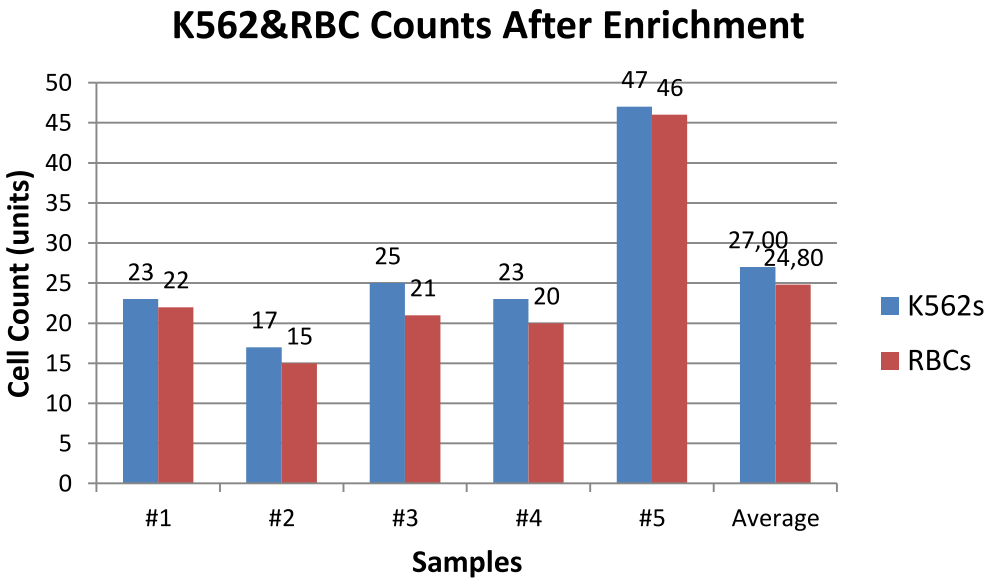

Figure 6.19 K562 and RBC counts from five individual samples after enrichment.

Table 6.2 K562 & RBC counts in the cell mixture taken from cancer cell outlet.

	1st sample	2nd sample	3rd sample	4th sample	5th sample	Average
Ratio of K562 cells to RBCs	1.05	1.13	1.19	1.15	1.02	1.09
Normalized Ratio of K562 cells to RBCs	1:0.96	1:0.88	1:0.84	1:0.87	1:0.98	1:0.92

According to the average values for the Table 6.1 and 6.2, cell enrichment factor for K562s were calculated as 1.45 from Eqn. 6.1. That means a 1.45 fold increase is realized for K562 percentage at the output relative to the input. The percent of reduction in RBC numbers at the cancer cell output relative to the input was calculated as 60%. The recovery rate for the K562 cells were calculated as 59% in the cancer cell outlet. Table 6.3 presents the summary of the calculated values of cell enrichment factor and recovery rate of K562 cells.

Table 6.3 Calculated values of cell enrichment factor and recovery rate of K562 cells (c.e.f.: cell enrichment factor).

	K562 cells / RBCs	# of K562 cells (units)	c.e.f.	Recovery Rate
Before enrichment	0.75	45.80	1.45	59%
After enrichment	1.09	27.00		

Secondly MCF7 cell enrichment was realized in MCF7 cells & RBCs mixture. Figure 6.20 presents the MCF7 and RBC counts in cell mixture before enrichment. To count MCF7 cells and RBCs, same steps with K562 counting part were applied. For the cell mixture before enrichment, five individual samples were taken and an average value was calculated. Table 6.4 presents the MCF7 and RBC ratios in cell mixture before enrichment.

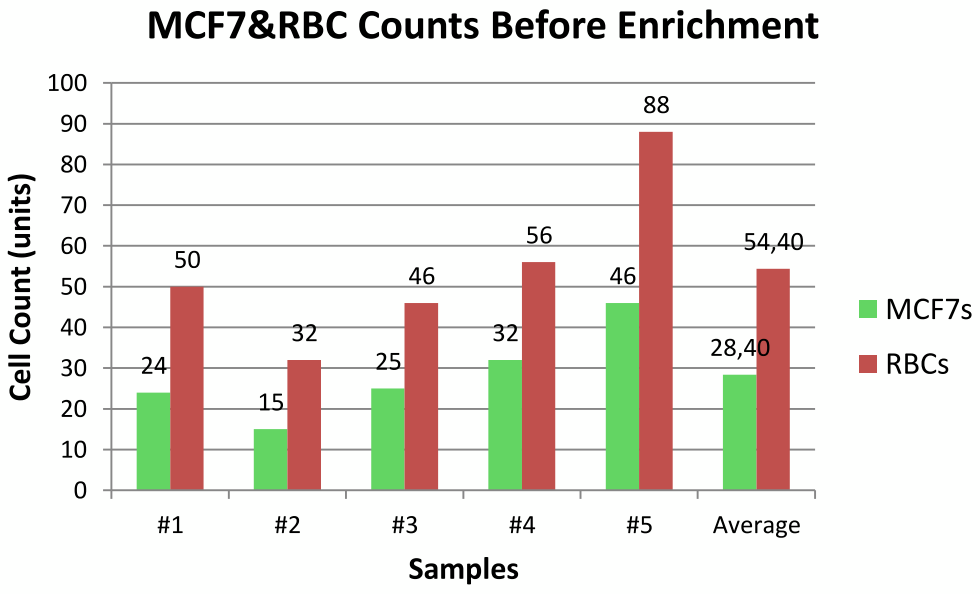

Figure 6.20 MCF7 and RBC counts from five individual samples before enrichment.

Table 6.4 MCF7 & RBC counts in the cell mixture before enrichment.

	1st sample	2nd sample	3rd sample	4th sample	5th sample	Average
Ratio of MCF7 cells to RBCs	0.48	0.47	0.54	0.57	0.52	0.52
Normalized Ratio of MCF7 cells to RBCs	1:2.08	1:2.13	1:1.85	1:1.75	1:1.92	1:1.92

Figure 6.21 preents the MCF7 and RBC counts in cell mixture taken from cancer cell outlet, after enrichment. To count the cells, same steps with previous part were applied. For the cell mixture taken from cancer outlet after enrichment, again five individual samples were taken and another average value was calculated. Table 6.5 presents the MCF7 and RBC ratios in cell mixture after enrichment.

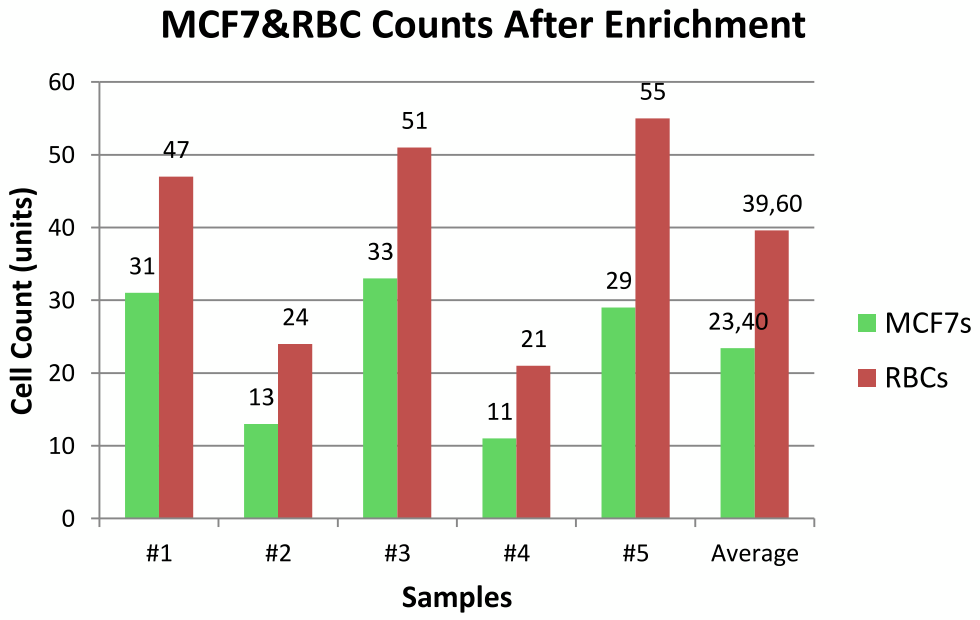

Figure 6.21 MCF7 and RBC counts from five individual samples after enrichment.

Table 6.5 MCF7 & RBC counts in the cell mixture taken from cancer cell outlet.

	1st sample	2nd sample	3rd sample	4th sample	5th sample	Average
Ratio of MCF7 cells to RBCs	0.66	0.54	0.65	0.52	0.53	0.59
Normalized Ratio of MCF7 cells to RBCs	1:1.52	1:1.85	1:1.54	1:1.92	1:1.89	1:1.69

According to the average values for the Table 6.4 and 6.5, cell enrichment factor for MCF7 cells were calculated as 1.13 from Eqn. 6.1. That means a 1.13 fold increase is realized for MCF7 cells percentage at the output relative to the input. The reduction percentage of the RBCs at the cancer output relative to the input was realized as 27%. The recovery rate for the MCF7 cells were calculated as 82% in the cancer cell outlet. Table 6.6 presents the summary of the calculated values of cell enrichment factor and recovery rate of K562 cells.

Table 6.6 Calculated values of cell enrichment factor and recovery rate of MCF7 cells (c.e.f.: cell enrichment factor).

	MCF7 cells / RBCs	# of MCF7 cells (units)	c.e.f.	Recovery Rate
Before enrichment	0.52	28.40	1.13	82%
After enrichment	0.59	23.40		

When the two enrichment factor values are compared, the cell enrichment factor calculated for MCF7 cells is lower than the factor calculated for K562 cells. According to the literature data, MCF7 cells are larger than K562 cells. Thus,

MCF7 cell enrichment factor should be higher than the K562 cell enrichment factor in normal conditions.

Although the tests showed that most of the RBCs were eliminated through the filtering gaps in the microchannels by escaping to the side channels or by sticking to the filters, after some time, RBCs started not to escape to the side channels. Sticking of RBCs caused clogging in the filters. Hence, newly coming RBCs could not traverse the gaps, and move toward cancer cell outlet, decreasing the enrichment factor. Besides, some rare cell escapes from the gaps were observed during the tests. The filter gap sizes were designed according to given cell sizes in the literature data. However, cancer cell sizes are not uniform, and some smaller cancer cells could pass through the gaps. This has further decreased the enrichment factor.

The results are combined for getting a rare cell enrichment factor in these DEP devices. The combined rare cell enrichment factor is 1.3, which means that rare cell percentages increase 1.3 fold in the rare cell outlet compared to the inlets of the DEP devices. An average 1.3 fold increase in the rare cell outlet compared to the inlets of the DEP devices, is still comparable with the other cell enrichment studies in the literature, although there are a few studies.

Gonghao *et al.* designed four different microchannels based on the viscoelastic properties of the cells and one of these devices have a minimum enrichment factor for K562 cells as 1.15 and an average enrichment factor as 3.2 [111]. Table 6.7 presents the cell enrichment factors of K562 cells for Gonghao *et al.* and this study as a comparison.

Table 6.7 Average and minimum cell enrichment factors of K562 cells (c.e.f.: cell enrichment factor).

c.e.f. (average)	c.e.f. (minimum)	Reference
3.20	1.15	[111]
1.45	1.23	-

Cheng *et al.* reported a DEP-based microfluidic device for separation of AS2-GFP cells. They reported recovery rates, defined as the collected cell amounts from target outlet divided by cell amounts given from inlet, for the applied cells in different flow rates. The recovery rate results for AS2-GFP cells (applying 30 µl/min flow rate) are calculated as ~60% [112]. These values were calculated as 59% for K562 cells and 82% for MCF7 cells at the same flow rate in this thesis study. Table 6.8 presents the recovery rates of the rare cells for Cheng *et al.* and this study as a comparison.

Table 6.8 Recovery rates of the rare cells at 30 µl/min flow rate.

AS2-GFP cells	K562 cells	MCF7 cells	Reference
~60%	N/A	N/A	[112]
N/A	59%	82%	-

According to the comparisons of enrichment factors and recovery rates, 3rd generation devices are promising for the future improvements on this study.

CHAPTER 7

CONCLUSION AND FUTURE WORK

In this thesis, the primary goal was to develop a MEMS-based DEP device for rare cell enrichment from blood. To achieve this goal, design, simulations, fabrication and experimental tests were performed.

Due to the various advantages, such as the low-cost fabrication, no harmfulness to the cells, no labeling needs, and ease of application in cell manipulation; DEP has been selected as the most suitable method among other cell manipulation techniques. The most challenging issue in rare cell enrichment from blood is the very high cell density of blood cells. Also, the volume of blood that should be processed is relatively high (>7.5 mL). These issues should be considered carefully in the design of electrode and microchannel geometries for DEP based cell enrichment. Microchannel width was designed as 1000 μm (the highest limit of parylene-C microchannel fabrication) to have a high throughput and to perform manipulation with high amount of cells in a continuous flow. Because of having a wide microchannel, 15° angular planar electrodes were designed parallel to each other with 3μm gaps in between and fabricated at the bottom of the microchannel.

In the 1st and 2nd generation devices, cell enrichment was done based on the nDEP principle, where cells are kept out of the strong electric fields generated by microelectrodes inside the microchannel.

In the 1st generation devices, problem of bubble formation was observed, which is caused by direct contact of the electrodes with the liquid medium. This has been solved in 2nd generation devices, where electrodes were coated with a thin parylene-C insulating layer. These devices included two consecutive DEP regions (focusing and selective), to which different frequencies at $20V_{pp}$ electric potential were applied based on the dielectric properties of K562 human leukemia cells, MCF7 human breast adenocarcinoma cells and RBCs from literature. Cell manipulations were observed at 0.1-1 μl/min flow rates, compatible with the simulations. Although cell manipulations were observed in the microchannels, some inabilities and limitations of these two generations such as cell escapes in the middle of the microchannels due to the microelectrode locations, crosstalk between different DEP regions due to applying different frequencies and low flow rates operation decreased the working capacity of these generations. To overcome these limitations, a novel design has been developed where pDEP force and the hydrodynamic forces have been used to fine-tune the cell movement over the electrodes under a high flow rate (up to 30 μl/min). Sliding of the cells on the planar electrodes idea necessitates a critical balance between drag force and DEP force. In the literature, there are many pDEP studies on cell manipulations, but these studies are based on cell trapping.

3rd generation devices bring some novelties to the study. Cell sliding on the planar electrodes is the primary finding with application of positive DEP frequencies (1 MHz). Electrode structures and locations were revised for optimum cell sliding. Asymmetric allocations and merging the tips of the planar electrodes prevented cell escapes. In addition, gaps were put to the walls of the main channel and a size-based separation was added to the devices. While smaller sized RBCs passed through the gaps and were directed to the waste channels, large sized rare cells (K562 and MCF7 cells) were filtered and manipulated to the cancer cell outlet.

Cell enrichment factor was calculated for both cell mixtures and satisfactory results were achieved with the 3rd generation devices.

Up to now, the design optimizations and experimental achievements were introduced. When the results were investigated carefully, some future studies should be done for improving the enrichment efficiency, such as:

- Increasing the throughput by adding parallel microchannels, so the device can be utilized for high sample volumes.
- Optimizing the filtering gap sizes to prevent RBC clogging and cancer cell escapes. The size of cancer cells and RBCs may vary depending on the sex, age, race, genetic factors, and different disease phases. Also, the mechanical properties of cells, like elasticity and shapes, may vary depending on the carrier fluid properties. These challenges make it difficult to decide on the optimal gap size for filtration-based separation.
- Optimizing the microchannel and filter gap sizes within the boundaries of MEMS fabrication techniques, to deal with coagulation and clogging issues.

REFERENCES

[1] "The American Cancer Society." [Online]. Available: www.cancer.org. [Accessed: 01-Aug-2015].

[2] S. Yan, J. Zhang, M. Li, G. Alici, H. Du, R. Sluyter, and W. Li, "On-chip high-throughput manipulation of particles in a dielectrophoresis-active hydrophoretic focuser.," *Sci. Rep.*, vol. 4, p. 5060, Jan. 2014.

[3] E. K. Sackmann, A. L. Fulton, and D. J. Beebe, "The present and future role of microfluidics in biomedical research.," *Nature*, vol. 507, no. 7491, pp. 181–9, Mar. 2014.

[4] D. Mark, S. Haeberle, G. Roth, F. von Stetten, and R. Zengerle, "Microfluidic lab-on-a-chip platforms: requirements, characteristics and applications.," *Chem. Soc. Rev.*, vol. 39, no. 3, pp. 1153–82, Mar. 2010.

[5] D. Li, *Electrokinetics in Microfluidics*, 1st Ed. London: Elsevier Ltd, 2004.

[6] I. Lazo, C. Peng, J. Xiang, S. V Shiyanovskii, and O. D. Lavrentovich, "Liquid crystal-enabled electro-osmosis through spatial charge separation in distorted regions as a novel mechanism of electrokinetics.," *Nat. Commun.*, vol. 5, no. May, p. 5033, Jan. 2014.

[7] "Cornell Micro/Nanofluidics Laboratory." [Online]. Available: www.kirbyresearch.com. [Accessed: 01-Aug-2015].

[8] C.-T. Kuo and C.-H. Liu, "A novel microfluidic driver via AC electrokinetics.," *Lab Chip*, vol. 8, no. 5, pp. 725–33, May 2008.

[9] A. Ajdari, "Electrokinetic 'ratchet' pumps for microfluidics," *Appl. Phys. A*, vol. 75, no. 2, pp. 271–274, Jan. 2002.

[10] K. Bengtsson, S. Nilsson, and N. D. Robinson, "Conducting polymer electrodes for gel electrophoresis.," *PLoS One*, vol. 9, no. 2, p. e89416, Jan. 2014.

[11] C. Dennison, *A Guide to Protein Isolation*. New York, Boston, Dordrecht, London, Moscow: Kluwer Academic Publishers, 2002.

[12] A. P. Lewis, A. Cranny, N. R. Harris, N. G. Green, J. A. Wharton, R. J. K. Wood, and K. R. Stokes, "Review on the development of truly portable and in-situ capillary electrophoresis systems," *Meas. Sci. Technol.*, vol. 24, no. 4, p. 042001, Apr. 2013.

[13] R. F. Renzi, J. Stamps, B. A. Horn, S. Ferko, V. A. Vandernoot, J. A. A. West, R. Crocker, B. Wiedenman, D. Yee, and J. A. Fruetel, "Hand-Held Microanalytical Instrument for Chip-Based Electrophoretic Separations of Proteins," *Anal. Chem.*, vol. 77, no. 2, pp. 435–441, 2005.

[14] J. Voldman, "Electrical Forces for Microscale Cell Manipulation," *Annu. Rev. Biomed. Eng.*, vol. 8, no. 1, pp. 425–454, Aug. 2006.

[15] D. Chen and H. Du, "A dielectrophoretic barrier-based microsystem for separation of microparticles," *Microfluid. Nanofluidics*, vol. 3, no. 5, pp. 603–610, Feb. 2007.

[16] S. Fiedler, S. G. Shirley, and T. Schnelle, "Dielectrophoretic Sorting of particles and Cells in a Microsystem," *Anal. Chem.*, vol. 70, no. 9, pp. 1909–1915, 1998.

[17] K. H. Kang, Y. Kang, X. Xuan, and D. Li, "Continuous separation of microparticles by size with direct current-dielectrophoresis.," *Electrophoresis*, vol. 27, no. 3, pp. 694–702, Feb. 2006.

[18] N. Lewpiriyawong, C. Yang, and Y. C. Lam, "Continuous sorting and separation of microparticles by size using AC dielectrophoresis in a PDMS microfluidic device with 3-D conducting PDMS composite electrodes.," *Electrophoresis*, vol. 31, no. 15, pp. 2622–31, Aug. 2010.

[19] N. A. M. Yunus, H. Nili, and N. G. Green, "Continuous separation of colloidal particles using dielectrophoresis.," *Electrophoresis*, vol. 34, no. 7, pp. 969–78, Apr. 2013.

[20] W. M. Arnold, "Dielectrophoretic Cell Separation : Some Hints and Kinks," *Proc. ESA Annu. Meet. Electrost.*, vol. 2, no. 1, pp. 1–11, 2010.

[21] M. Urdaneta and E. Smela, "Parasitic trap cancellation using multiple frequency dielectrophoresis, demonstrated by loading cells into cages.," *Lab Chip*, vol. 8, no. 4, pp. 550–6, Apr. 2008.

[22] B. H. Lapizco-encinas, B. A. Simmons, E. B. Cummings, Y. Fintschenko, S. N. Laboratories, and P. O. Box, "Dielectrophoretic Concentration and Separation of Live and Dead Bacteria in an Array of Insulators voltages

across a microchannel containing an array of," *Anal. Chem.*, vol. 76, no. 6, pp. 1571–1579, 2004.

[23] X. Hu, P. H. Bessette, J. Qian, C. D. Meinhart, P. S. Daugherty, and H. T. Soh, "Marker-specific sorting of rare cells using dielectrophoresis," *PNAS*, vol. 102, no. 44, pp. 15757–15761, 2005.

[24] M. P. Hughes, H. M. Y, F. J. Rixon, J. P. H. Burt, and R. Pethig, "Manipulation of herpes simplex virus type 1 by dielectrophoresis," *Biochem. Res. Int.*, vol. 1425, pp. 119–126, 1998.

[25] I. Ermolina, J. Milner, and H. Morgan, "Dielectrophoretic investigation of plant virus particles: Cow Pea Mosaic Virus and Tobacco Mosaic Virus.," *Electrophoresis*, vol. 27, no. 20, pp. 3939–48, Oct. 2006.

[26] A. R. Minerick, R. Zhou, P. Takhistov, and H.-C. Chang, "Manipulation and characterization of red blood cells with alternating current fields in microdevices.," *Electrophoresis*, vol. 24, no. 21, pp. 3703–17, Nov. 2003.

[27] J. E. Gordon, Z. Gagnon, and H.-C. Chang, "Dielectrophoretic discrimination of bovine red blood cell starvation age by buffer selection and membrane cross-linking.," *Biomicrofluidics*, vol. 1, no. 4, p. 44102, Jan. 2007.

[28] M.-W. Wang, K.-S. Jeng, M.-C. Yu, and J.-C. Su, "Using a Microfluidic–Microelectric Device to Directly Separate Serum/Blood Cells from a Continuous Whole Bloodstream Flow," *Jpn. J. Appl. Phys.*, vol. 51, p. 037002, Feb. 2012.

[29] M. Yamashita, S. Miyata, S. Takeuchi, and H. Inoue, "Separation method of Blood Constituents Using Dielectrophoresis and Flow-Induced Shear Force," in *35th Annual International Conference of the IEEE EMBS*, 2013, pp. 4462–4465.

[30] A. Salmanzadeh, "Isolation of Rare Cells through their Dielectrophoretic Signature," *J. Membr. Sci. Technol.*, vol. 03, no. 01, pp. 1–4, 2013.

[31] S. Chin, M. P. Hughes, and H. M. Coley, "Rapid assessment of early biophysical changes in K562 cells during apoptosis determined using dielectrophoresis," *Int. J. Nanomedicine*, vol. 1, no. 3, pp. 333–337, 2006.

[32] P. Vulto, G. Medoro, L. Altomare, G. a Urban, M. Tartagni, R. Guerrieri, and N. Manaresi, "Selective sample recovery of DEP-separated cells and particles by phaseguide-controlled laminar flow," *J. Micromechanics Microengineering*, vol. 16, no. 9, pp. 1847–1853, Sep. 2006.

[33] H. Shafiee, M. B. Sano, E. a Henslee, J. L. Caldwell, and R. V Davalos, “Selective isolation of live/dead cells using contactless dielectrophoresis (cDEP).,” *Lab Chip*, vol. 10, no. 4, pp. 438–45, Feb. 2010.

[34] Y. Demircan, A. Koyuncuoğlu, M. Erdem, E. Özgür, U. Gündüz, and H. Külah, “Label-free detection of multidrug resistance in K562 cells through isolated 3D-electrode dielectrophoresis.,” *Electrophoresis*, vol. 36, no. 9–10, pp. 1149–57, May 2015.

[35] A. Alazzam, I. Stiharu, R. Bhat, and A.-N. Meguerditchian, “Interdigitated comb-like electrodes for continuous separation of malignant cells from blood using dielectrophoresis.,” *Electrophoresis*, vol. 32, no. 11, pp. 1327–36, Jun. 2011.

[36] J. An, J. Lee, Y. Kim, B. Kim, and S. Lee, “Analysis of Cell Separation Efficiency in Sorter, Dielectrophoresis-activated Cell,” in *Proceedings of the 3rd IEEE Int. Conf. on Nano/Micro Engineered and Molecular Systems*, 2008, pp. 965–969.

[37] F. F. Becker, X. Wang, Y. Huang, R. Pethigt, J. Vykoukal, and P. R. C. Gascoyne, “Separation of human breast cancer cells from blood by differential dielectric affinity,” *Proc. Natl. Acad. Sci. USA*, vol. 92, no. January, pp. 860–864, 1995.

[38] H. M. Coley, F. H. Labeed, H. Thomas, and M. P. Hughes, “Biophysical characterization of MDR breast cancer cell lines reveals the cytoplasm is critical in determining drug sensitivity.,” *Biochim. Biophys. Acta*, vol. 1770, no. 4, pp. 601–8, Apr. 2007.

[39] U. Kim, C. Shu, K. Y. Dane, P. S. Daugherty, J. Y. J. Wang, and H. T. Soh, “Selection of mammalian cells based on their cell-cycle phase using dielectrophoresis,” *PNAS*, vol. 104, no. 52, pp. 20708–20712, 2007.

[40] A. Salmanzadeh, M. B. Sano, H. Shafiee, M. A. Stremler, and R. V Davalos, “Isolation of Rare Cancer Cells from Blood Cells Using Dielectrophoresis,” *34th Annu. Int. Conf. IEEE EMBS*, pp. 590–593, 2012.

[41] J. Yang, Y. Huang, X. Wang, F. F. Becker, and P. R. C. Gascoyne, “Cell Separation on Microfabricated Electrodes Using Dielectrophoretic / Gravitational Field-Flow Fractionation,” *Anal. Chem.*, vol. 71, no. 5, pp. 911–918, 1999.

[42] C. Huang, T. G. Amstislavskaya, Y. Chen, G. Chen, C. Jen, and H. Chang, “Selectively Concentrating Cervical Carcinoma Cells from Red Blood

Cells Utilizing Dielectrophoresis with Circular ITO Electrodes in Stepping Electric Fields," *J. Med. Biol. Eng.*, vol. 33, no. 1, pp. 51–58, 2012.

[43] L. M. Broche, N. Bhadal, M. P. Lewis, S. Porter, M. P. Hughes, and F. H. Labeed, "Early detection of oral cancer - Is dielectrophoresis the answer?," *Oral Oncol.*, vol. 43, no. 2, pp. 199–203, Feb. 2007.

[44] P. R. C. Gascoyne, X. Wang, Y. Huang, and F. F. Becker, "Dielectrophoretic Separation of Cancer Cells from Blood," *IEEE Trans. Ind. Appl.*, vol. 33, no. 3, pp. 670–678, 1997.

[45] L. Wu, L. L. Yung, and K. Lim, "Dielectrophoretic capture voltage spectrum for measurement of dielectric properties and separation of cancer cells," *Biomicrofluidics*, vol. 014113, pp. 1–10, 2012.

[46] F. Yang, X. Yang, H. Jiang, W. M. Butler, and G. Wang, "Dielectrophoretic separation of prostate cancer cells.," *Technol. Cancer Res. Treat.*, vol. 12, no. 1, pp. 61–70, Feb. 2013.

[47] P. Gascoyne, R. Pethig, J. Satavivad, F. F. Becker, and M. Ruchirawat, "Dielectrophoretic detection of changes in erythrocyte membranes following malarial infection," *Biochim. Biophys. Acta*, vol. 1323, pp. 240–252, 1997.

[48] E. Du, M. Dao, and S. Suresh, "Quantitative biomechanics of healthy and diseased human red blood cells using dielectrophoresis in a microfluidic system," *Extrem. Mech. Lett.*, vol. 1, no. 2014, pp. 35–41, 2014.

[49] H. Song, J. M. Rosano, Y. Wang, C. J. Garson, B. Prabhakarpandian, K. Pant, G. J. Klarmann, A. Perantoni, L. M. Alvarez, and E. Lai, "Continuous-flow sorting of stem cells and differentiation products based on dielectrophoresis.," *Lab Chip*, vol. 15, pp. 1320–1328, 2015.

[50] S. Hardt and F. Schönfeld, Eds., *Microfluidic Technologies for Miniaturized Analysis Systems*. New York: Springer Science+Business Media, LLC, 2007.

[51] M. Toner and D. Irimia, "Blood-on-a-chip," *Annu Rev Biomed Eng.*, vol. 7, no. 1, pp. 77–103, 2005.

[52] R. Pethig, "Review article-dielectrophoresis: status of the theory, technology, and applications.," *Biomicrofluidics*, vol. 4, no. 2, pp. 1–35, Jan. 2010.

[53] H. A. Pohl, “The Motion and Precipitation of Suspensoids,” *J. Appl. Phys.*, vol. 22, no. 7, pp. 869–871, 1950.

[54] R. Pethig, *Dielectric and electronic properties of biological materials*. New York: John Wiley & Sons, 1979.

[55] R. Pethig and G. H. Markx, “Applications of dielectrophoresis in biotechnology,” *Tibtech*, vol. 15, no. October, pp. 426–432, 1997.

[56] A. Lenshof and T. Laurell, “Continuous separation of cells and particles in microfluidic systems.,” *Chem. Soc. Rev.*, vol. 39, no. 3, pp. 1203–1217, 2010.

[57] X. Xing and L. Yobas, “Dielectrophoretic (DEP) separation of live / dead cells on a glass slide functionalized with interdigitated 3D silicon ring microelectrodes,” pp. 951–954, 2014.

[58] N. Demierre, T. Braschler, P. Linderholm, U. Seger, H. van Lintel, and P. Renaud, “Characterization and optimization of liquid electrodes for lateral dielectrophoresis.,” *Lab Chip*, vol. 7, no. 3, pp. 355–65, Mar. 2007.

[59] A. W. Maijenburg, M. G. Maas, E. J. B. Rodijk, W. Ahmed, E. S. Kooij, E. T. Carlen, D. H. a Blank, and J. E. ten Elshof, “Dielectrophoretic alignment of metal and metal oxide nanowires and nanotubes: a universal set of parameters for bridging prepatterned microelectrodes.,” *J. Colloid Interface Sci.*, vol. 355, no. 2, pp. 486–93, Mar. 2011.

[60] S. Zeinali, B. Çetin, S. N. B. Oliaei, and Y. Karpat, “Fabrication of continuous flow microfluidics device with 3D electrode structures for high throughput DEP applications using mechanical machining.,” *Electrophoresis*, vol. 36, no. 13, pp. 1432–42, Jul. 2015.

[61] S. Bunthawin, J. Kongklaew, A. Tuantranont, K. Jaruwongrangsri, and T. Maturos, “Microchip Electrode Development for Traveling wave Dielectrophoresis of Non-Spherical Cell Suspensions,” *Engineering*, vol. 04, no. 10, pp. 88–93, 2012.

[62] M. Nasabi, K. Khoshmanesh, F. J. Tovar-Lopez, K. Kalantar-Zadeh, and A. Mitchell, “Dielectrophoresis with 3D microelectrodes fabricated by surface tension assisted lithography.,” *Electrophoresis*, vol. 34, no. 22–23, pp. 3150–4, Dec. 2013.

[63] C. Yu, J. Vykoukal, D. M. Vykoukal, J. A. Schwartz, L. Shi, P. R. C. Gascoyne, and I. T. Cytometry, “A Three-Dimensional Dielectrophoretic

Particle Focusing Channel for Microcytometry Applications," vol. 14, no. 3, pp. 480–487, 2005.

[64] S. Schuerle, M. K. Tiwari, K. Shou, D. Poulikakos, and B. J. Nelson, "Fabricating devices with dielectrophoretically assembled, suspended single walled carbon nanotubes for improved nanoelectronic device characterization," *Microelectron. Eng.*, vol. 88, no. 8, pp. 2740–2743, Aug. 2011.

[65] D. S. Gray, J. L. Tan, J. Voldman, and C. S. Chen, "Dielectrophoretic registration of living cells to a microelectrode array," *Biosens. Bioelectron.*, vol. 19, no. 7, pp. 771–780, Feb. 2003.

[66] S. H. Lee, G. Yun, Y. Koh, S. Lee, and Y. Kim, "Fabrication of a 3 dimensional dielectrophoresis electrode by a metal inkjet printing method," pp. 1–7, 2013.

[67] Y. Kim, X. Ren, J. W. Kim, and H. Noh, "Direct inkjet printing of micro-scale silver electrodes on polydimethylsiloxane (PDMS) microchip," *J. Micromechanics Microengineering*, vol. 24, no. 11, p. 115010, Nov. 2014.

[68] Z. Zhao, X. Zheng, J. Yang, X. Wu, X. Hei, and Y. Cao, "Dielectrophoretic Manipulation of Cells by Using Interdigitated Microelectrodes," in *Proceedings of the 1st IEEE International Conference on Nano/Micro Engineered and Molecular Systems*, 2006, pp. 1021–1024.

[69] C. Iliescu, L. Yu, F. E. H. Tay, and B. Chen, "Bidirectional field-flow particle separation method in a dielectrophoretic chip with 3D electrodes," *Sensors Actuators B Chem.*, vol. 129, no. 1, pp. 491–496, Jan. 2008.

[70] V. H. Perez-Gonzalez, V. Ho, L. Kulinsky, M. Madou, and S. O. Martinez-Chapa, "PPyDEP: a new approach to microparticle manipulation employing polymer-based electrodes.," *Lab Chip*, vol. 13, no. 23, pp. 4642–52, Dec. 2013.

[71] R. Martinez-Duarte, "Microfabrication technologies in dielectrophoresis applications--a review.," *Electrophoresis*, vol. 33, no. 21, pp. 3110–32, Nov. 2012.

[72] R. Martinez-Duarte, P. Renaud, and M. J. Madou, "A novel approach to dielectrophoresis using carbon electrodes.," *Electrophoresis*, vol. 32, no. 17, pp. 2385–92, Sep. 2011.

[73] S. Tuukkanen, J. J. Toppari, A. Kuzyk, L. Hirviniemi, and V. P. Hyto, "Carbon Nanotubes as Electrodes for Dielectrophoresis of DNA," *Nano Lett.*, 2006.

[74] V. H. Perez-Gonzalez, V. Ho, L. Kulinsky, and S. O. Martinez-Chapa, "Dielectrophoresis-assisted electroconductive polymer-based fabrication of high surface area electrodes," vol. 9056, p. 905628, Mar. 2014.

[75] N. Lewpiriyawong and C. Yang, "AC-dielectrophoretic characterization and separation of submicron and micron particles using sidewall AgPDMS electrodes," *Biomicrofluidics*, vol. 6, no. 1, pp. 1–9, 2012.

[76] A. Valero, T. Braschler, and P. Renaud, "A unified approach to dielectric single cell analysis: impedance and dielectrophoretic force spectroscopy.," *Lab Chip*, vol. 10, no. 17, pp. 2216–25, Sep. 2010.

[77] H. R. Gwon, S. T. Chang, C. K. Choi, J. Y. Jung, J. M. Kim, and S. H. Lee, "Development of a new contactless dielectrophoresis system for active particle manipulation using movable liquid electrodes," *Electrophoresis*, vol. 35, no. 14, pp. 2014–2021, 2014.

[78] B. Yafouz, N. A. Kadri, and F. Ibrahim, "Dielectrophoretic manipulation and separation of microparticles using microarray dot electrodes.," *Sensors (Basel).*, vol. 14, no. 4, pp. 6356–69, Jan. 2014.

[79] H. Li and R. Bashir, "Dielectrophoretic separation and manipulation of live and heat-treated cells of Listeria on microfabricated devices with interdigitated electrodes," *Sensors Actuators, B Chem.*, vol. 86, no. 2–3, pp. 215–221, 2002.

[80] M. S. Pommer, Y. Zhang, N. Keerthi, D. Chen, J. a Thomson, C. D. Meinhart, and H. T. Soh, "Dielectrophoretic separation of platelets from diluted whole blood in microfluidic channels.," *Electrophoresis*, vol. 29, no. 6, pp. 1213–8, Mar. 2008.

[81] N. G. Green, a Ramos, and H. Morgan, "Ac electrokinetics: a survey of sub-micrometre particle dynamics," *J. Phys. D. Appl. Phys.*, vol. 33, no. 6, pp. 632–641, 2000.

[82] P. R. C. Gascoyne, "Review Particle separation by dielectrophoresis," *Electrophoresis*, pp. 1973–1983, 2002.

[83] L. Wang, L. a Flanagan, E. Monuki, N. L. Jeon, and A. P. Lee, "Dielectrophoresis switching with vertical sidewall electrodes for

microfluidic flow cytometry.," *Lab Chip*, vol. 7, no. 9, pp. 1114–1120, 2007.

[84] J. Voldman, M. Toner, M. L. Gray, and M. a. Schmidt, "Design and analysis of extruded quadrupolar dielectrophoretic traps," *J. Electrostat.*, vol. 57, no. 1, pp. 69–90, 2003.

[85] E. S. Elvington, A. Salmanzadeh, M. a Stremler, and R. V Davalos, "Label-free isolation and enrichment of cells through contactless dielectrophoresis.," *J. Vis. Exp.*, no. 79, pp. 1–12, 2013.

[86] J. K.-J. Li, *Dynamics of the Vascular System vol1*. Singapore: World Scientific Publishing Co. Re. Ltd., 2004.

[87] L. Waite and J. M. Fine, *Applied Biofluid Mechanics*. New York: McGraw-Hill Education, 2007.

[88] J. E. Smith, "Erythrocyte Membrane : Structure , Function , and Pathophysiology," *Vet. Pathol.*, vol. 24, pp. 471–476, 1987.

[89] T. Gordon-Smith, "Structure and function of red and white blood cells," *Medicine (Baltimore).*, vol. 41, no. 4, pp. 193–199, 2013.

[90] "The Histology Guide." [Online]. Available: wwww.histology.leeds.co.uk. [Accessed: 01-Aug-2015].

[91] L. Dean, *Blood Groups and Red Cell Antigens*. Bethesda, MD: National Center for Biotechnology Information, 2005.

[92] "UNSW Embryology." [Online]. Available: embryology.med.unsw.edu.au. [Accessed: 01-Aug-2015].

[93] D. Köhler, P. Bacher, A. Scheffold, M. Assenmacher, and M. Herber, "High-sensitivity detection and analysis of rare cells by integrated magnetic enrichment and flow cytometry using the MACSQuant ® Analyzer High-sensitivity detection and analysis of rare cells by integrated magnetic enrichment and flow cytometry using the ," vol. 14, 2012.

[94] M. Alunni-Fabbroni and M. T. Sandri, "Circulating tumour cells in clinical practice: Methods of detection and possible characterization.," *Methods*, vol. 50, no. 4, pp. 289–97, Apr. 2010.

[95] "Cellular Circuit." [Online]. Available: http://www.biotele.com/bioelectric.htm. [Accessed: 01-Aug-2015].

[96] X. Wang, F. F. Becker, and P. R. C. Gascoyne, “The fractal dimension of cell membrane correlates with its capacitance: a new fractal single-shell model.,” *Chaos*, vol. 20, no. 4, p. 043133, Dec. 2010.

[97] Z.-W. Zhang, J. Cheng, F. Xu, Y.-E. Chen, J.-B. Du, M. Yuan, F. Zhu, X.-C. Xu, and S. Yuan, “Red blood cell extrudes nucleus and mitochondria against oxidative stress.,” *IUBMB Life*, vol. 63, no. 7, pp. 560–5, Jul. 2011.

[98] G. K. and S. B. . Snyder, “Red Blood Cells : Centerpiece in the Evolution of the Vertebrate,” *Amer. Zool.*, vol. 198, pp. 189–198, 1999.

[99] R. Hober, “Messungen der inneren Leitfähigkeit von Zellen,” *Pflügers Arch. Eur. J. Physiol.*, vol. 150, no. 1–2, pp. 15–45, 1913.

[100] D. Walz, H. Berg, and G. Milazzo, *Biochemistry of Cells and Tissues*. 1995.

[101] M. B. Sano, E. a Henslee, E. Schmelz, and R. V Davalos, “Contactless dielectrophoretic spectroscopy: examination of the dielectric properties of cells found in blood.,” *Electrophoresis*, vol. 32, no. 22, pp. 3164–71, Nov. 2011.

[102] J. Gimsa, T. Schnelle, G. Zechel, and R. Glaser, “Dielectric Spectroscopy of Human Erythrocytes : Investigations Under the Influence of Nystatin,” *Biophys. J.*, vol. 66, no. April, 1994.

[103] R. S. Kuczenski, H.-C. Chang, and A. Revzin, “Dielectrophoretic microfluidic device for the continuous sorting of Escherichia coli from blood cells.,” *Biomicrofluidics*, vol. 5, no. 3, pp. 32005–3200515, Sep. 2011.

[104] J. Gimsa and D. Wachner, “A Unified Resistor-Capacitor Model for Impedance , Dielectrophoresis , Electrorotation , and Induced Transmembrane Potential,” *Biophys. J.*, vol. 75, no. August, pp. 1107–1116, 1998.

[105] Y. Demircan, “Detection of Imatinib and Doxorubicin Resistance In K562 Leukemia Cells by 3D-Electrode Contactless Dielectrophoresis.,” METU, 2013.

[106] F. H. Labeed, H. M. Coley, H. Thomas, and M. P. Hughes, “Assessment of Multidrug Resistance Reversal Using Dielectrophoresis and Flow Cytometry,” *Biophys. J.*, vol. 85, no. September, pp. 2028–2034, 2003.

[107] Y. A. Assef, A. E. Damiano, E. Zotta, C. Ibarra, B. A. Kotsias, and A. Yanina, “CFTR in K562 human leukemic cells,” *Am. J. Physiol. Cell Physiol.*, vol. 285, pp. 480–488, 2003.

[108] F. H. Labeed, H. M. Coley, and M. P. Hughes, “Differences in the biophysical properties of membrane and cytoplasm of apoptotic cells revealed using dielectrophoresis.,” *Biochim. Biophys. Acta*, vol. 1760, no. 6, pp. 922–9, Jun. 2006.

[109] D. L. Holliday and V. Speirs, “Choosing the right cell line for breast cancer research.,” *Breast Cancer Res.*, vol. 13, no. 4, p. 215, 2011.

[110] P. R. C. Gascoyne, S. Shim, J. Noshari, F. F. Becker, and K. Stemke-Hale, “Correlations between the dielectric properties and exterior morphology of cells revealed by dielectrophoretic field-flow fractionation,” *Electrophoresis*, vol. 34, no. 7, pp. 1042–1050, 2013.

[111] W. Gonghao, C. Kaci, T. Cory, L. Wilbur, A. Alexander, and S. Todd, “Microfluidic cellular enrichment and separation through differences in viscoelastic deformation.,” *Lab Chip*, vol. 15, no. 532, pp. 532–540, 2015.

[112] I.-F. Cheng, W.-L. Huang, T.-Y. Chen, C.-W. Liu, Y.-D. Lin, and W.-C. Su, “Antibody-Free Isolation of Rare Cancer Cells from Blood based on 3D Lateral Dielectrophoresis,” *Lab Chip*, vol. 15, pp. 2950–2959, 2015.

APPENDIX A

COMSOL SIMULATIONS

3D particle tracing simulation of RBCs for 5 kHz is presented in Figure A.1. 5 kHz was applied to both electrode regions at the same time and four individual streamlines were simulated under nDEP force. Top view simulation was also observed without visible DEP region on the electrodes, thus RBC manipulation can be seen clearly. First DEP region manipulates RBCs to the walls, then second region again manipulates RBCs into the center of the microchannel, thus they can be directed to the waste channel.

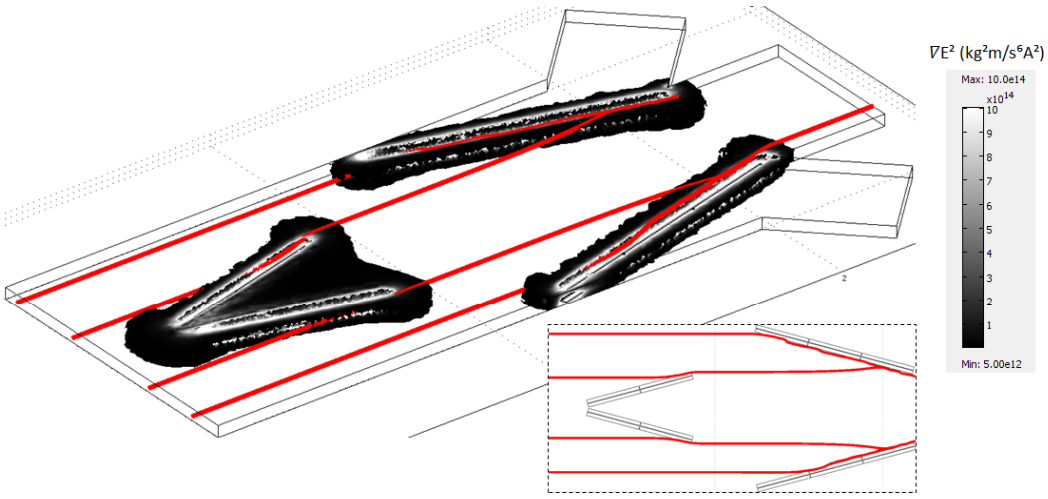

Figure A.1 3D particle tracing simulation for RBCs at 5 kHz.

3D particle tracing simulation of RBCs for 26.3 kHz is presented in Figure A.2. 26.3 kHz was applied to both electrode regions at the same time and four

individual streamlines were simulated under nDEP force. RBCs were manipulated into the waste channel because of having nDEP at 26.3 kHz.

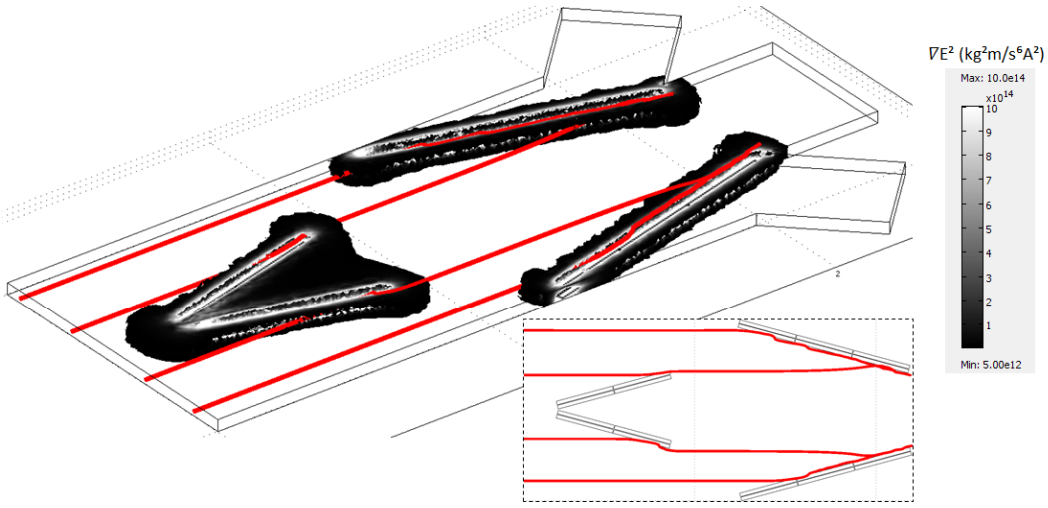

Figure A.2 3D particle tracing simulation for RBCs at 26.3 kHz.

3D particle tracing simulation of RBCs for 12.7 kHz is presented in Figure A.3. 12.7 kHz was applied to both electrode regions at the same time and four individual streamlines were simulated under nDEP force. 12.7 kHz can manipulate RBCs into the waste channel.

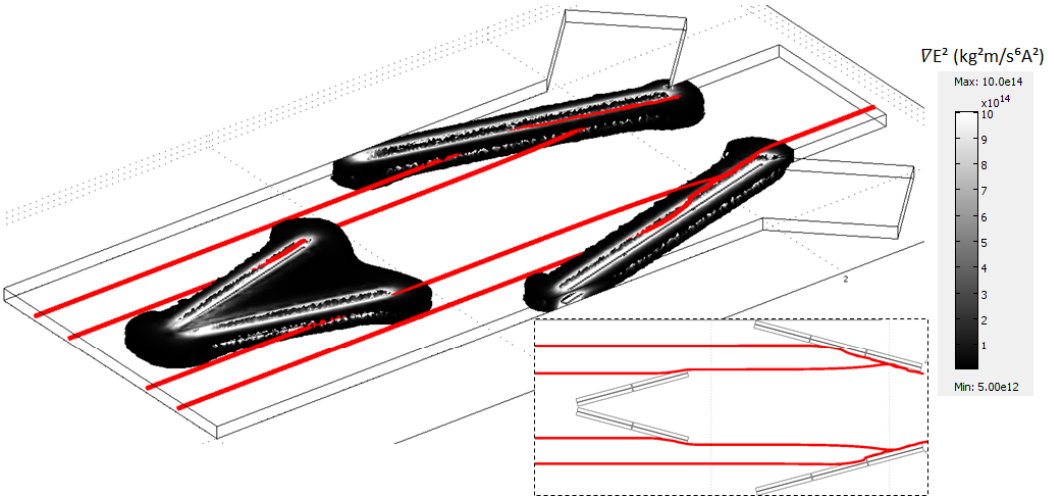

Figure A.3 3D particle tracing simulation for RBCs at 12.7 kHz.

3D particle tracing simulation of K562 cells for 5 kHz is presented in Figure A.4. 5 kHz was applied to both electrode regions at the same time and four individual streamlines were simulated. 5 kHz can be used to manipulate K562 cells by nDEP force.

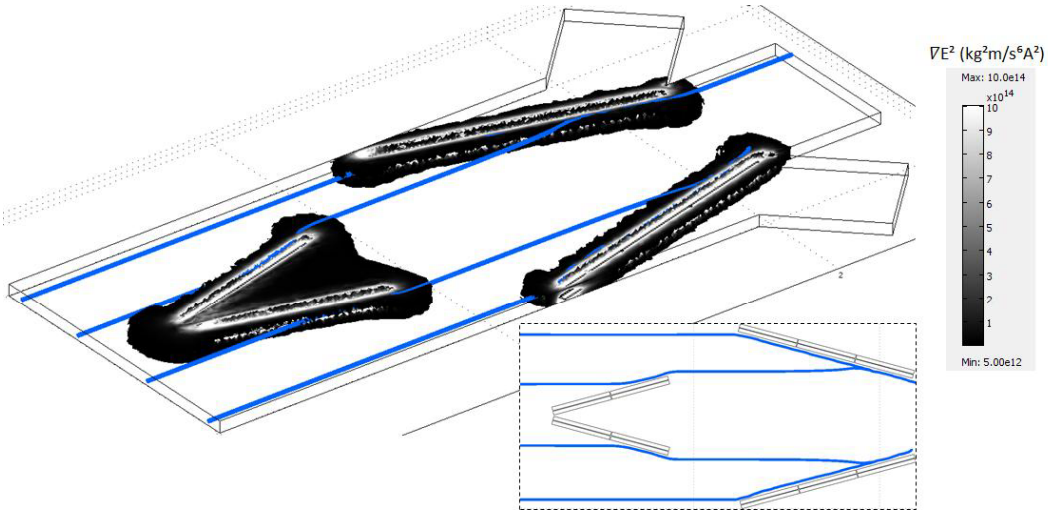

Figure A.4 3D particle tracing simulation for K562 cells at 5 kHz.

3D particle tracing simulation of K562 cells for 26.3 kHz is presented in Figure A.5. This frequency was applied to both electrode regions at the same time and four individual streamlines were simulated. 26.3 kHz is one of the crossover frequencies for K562s and these cells flow without any manipulation.

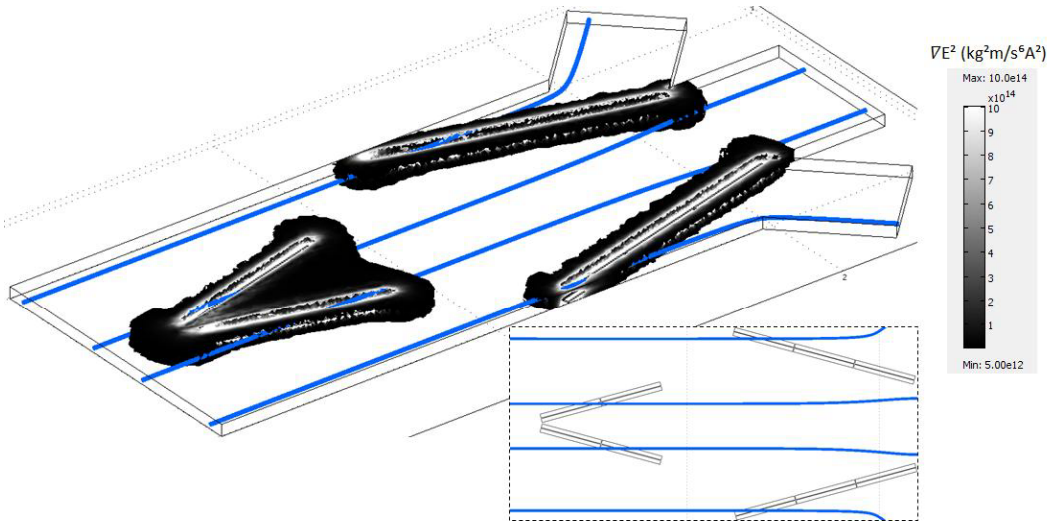

Figure A.5 3D particle tracing simulation for K562 cells at 26.3 kHz.

3D particle tracing simulation of MCF7 cells for 5 kHz is presented in Figure A.6. 5 kHz was applied to both electrode regions at the same time and four individual streamlines were simulated. At 5 kHz, MCF7 cells can be manipulated by nDEP force.

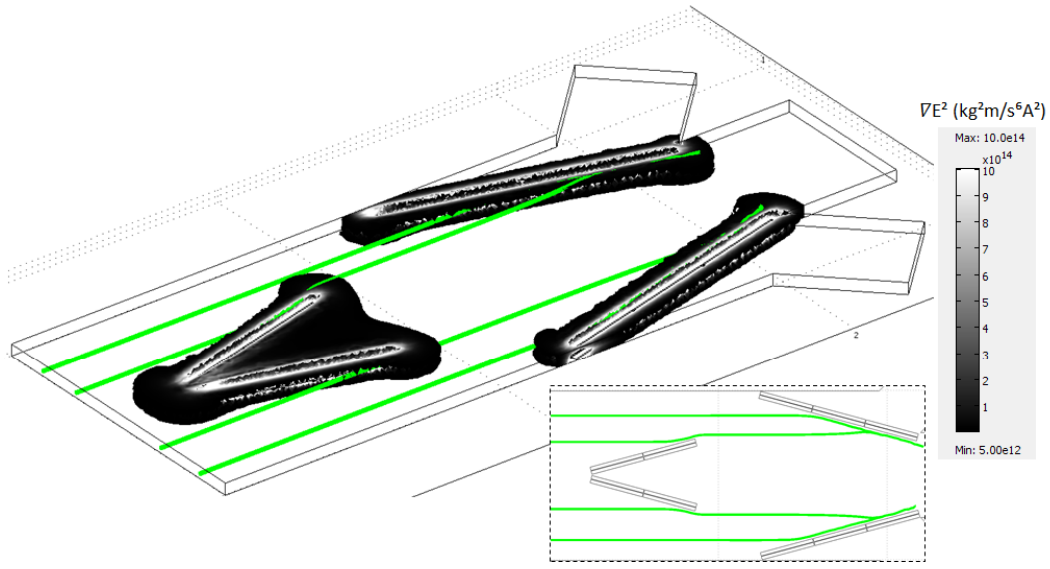

Figure A.6 3D particle tracing simulation for MCF7 cells at 5 kHz.

3D particle tracing simulation of MCF7s for 12.7 kHz is presented in Figure A.5. This frequency was applied to both electrode regions at the same time and four individual streamlines were simulated. 12.7 kHz is one of the crossover frequencies for MCF7 cells and these cells flow without any manipulation.

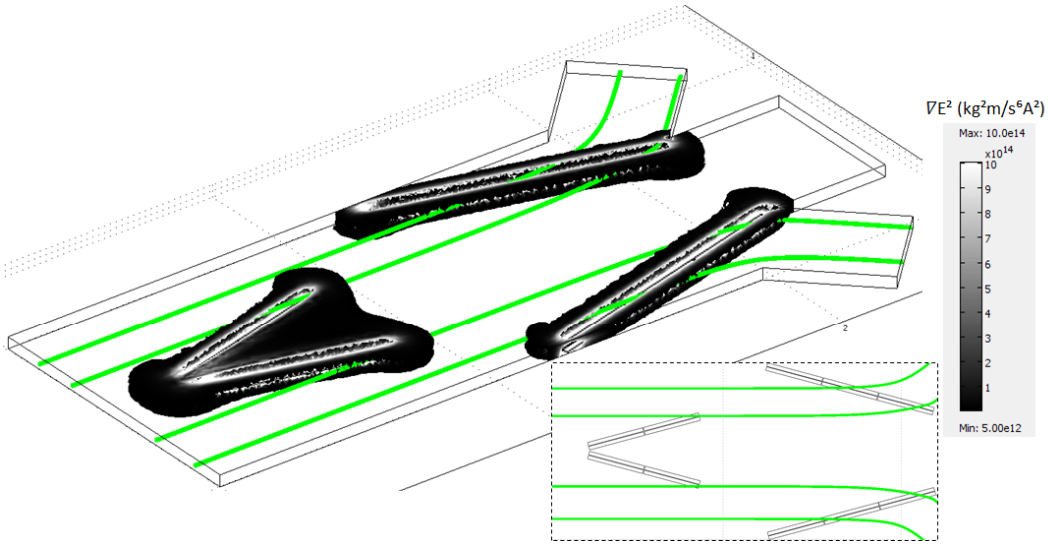

Figure A.7 3D particle tracing simulation for MCF7 cells at 12.7 kHz.

APPENDIX B

FABRICATION FLOWS

Fabrication flow of 1st generation devices is presented in Table B.1.

Table B.1: Detailed fabrication flow of the 1st generation devices.

	1st generation devices fabrication flow
1	***Glass wafer (4")***
2	***Piranha (30 min) + BHF (2 min) cleaning***
3	***Dehydration at oven at 110°C for 20 min***
4	***Parylene coating***
	with silane
	10 g for 5 μm parylene thickness
5	***Dehydration at oven at 95°C for 40 min***
6	***Ti sputtering as adhesion layer (AJA-1)***
	600 W 270 sec 30 nm
7	***Au sputtering layer (AJA-1)***
	350 W 680 sec 400 nm
8	***Dehydration at oven at 95°C for 40 min***
9	***Lithography for electrode formation***
Mask 1	HDMS coating 500 rpm 15 sec + 4000 rpm 40 sec
	S220-3 spin 500 rpm 15 sec + 4000 rpm 40 sec
	Softbake @ 95°C for 2 min hotplate
	Expose UV for 5 sec (vacuum contact)
	Develop in MF24A for 60 sec

Table B.1 (continued).

	DI water rinse 90 sec + 90 sec
	Dry by N_2
	Inspection
	Hardbake at oven @ 95°C for 40 min
	Desicator for 5 min
10	***Descum 2 min***
11	***Au etching***
	Aqua regia (600 ml HCl + 200 ml HNO_3) activation for 15 min
	Preparation of aqua regia solution (by adding 800 ml DI water)
	Etching for 80 sec
	DI water rinse 3 cycles
	Dry by N_2
	Inspection
12	***Ti etching***
	Ti etchant (25 ml HF + 25 ml H_2O_2 + 1550 ml DI water)
	Etching for 19 sec
	DI water rinse 3 cycles
	Dry by N_2
	Inspection
13	***PR strip***
	In acetone for 45 min
	In IPA for 10 min
	DI water rinse 3 cycles
	Dry by N_2
	Inspection
14	***Dehydration at oven at 95°C for 40 min***
15	***Lithography for microchannel formation***
Mask 2	HDMS coating 300 rpm 10 sec + 1000 rpm 30 sec

Table B.1 (continued).

	AZ9260 spin 300 rpm 10 sec + 1000 rpm 30 sec (first layer)
	Edge bead removal
	Wait for 15 min
	Prebake @ 95°C for 2 min at hotplate
	AZ9260 spin 300 rpm 10 sec + 1000 rpm 30 sec (second layer)
	Edge bead removal
	Wait for 15min
	Hardbake at oven from room temperature to 95°C and 50min @ 95°C
	Cooling at oven from 95°C to 70°C
	Rehydration (overnight)
	Expose UV for 40 sec (vacuum contact)
	Develop in AZ826MIF for 10 min
	DI water rinse 90 sec + 90 sec
	Dry by N_2
	Inspection
	Expose UV for 20 sec (vacuum contact)
	Develop in AZ826MIF for 10 min
	DI water rinse 90 sec + 90 sec
	Dry by N_2
	Inspection
16	***Microchannel thickness measurement (Dektak)***
17	***Parylene coating***
	without silane
	40 g for 20 μm parylene thickness
18	***Opening lithography***
Mask 3	HDMS coating 500 rpm 10 sec + 750 rpm 30 sec
	AZ9260 spin 500 rpm 10 sec + 750 rpm 30 sec (first layer)
	Edge bead removal

Table B.1 (continued).

	Wait for 15 min
	Prebake @ 95°C for 3 min at hotplate
	AZ9260 spin 500 rpm 10 sec + 750 rpm 30 sec (second layer)
	Edge bead removal
	Wait for 15min
	Hardbake at oven from room temperature to 95°C and 50min @ 95°C
	Cooling at oven from 95°C to 70°C
	Rehydration (overnight)
	Expose UV for 55 sec (vacuum contact)
	Develop in AZ826MIF for 20 min
	DI water rinse 90 sec + 90 sec
	Dry by N_2
	Inspection
	Expose UV for 55 sec (vacuum contact)
	Develop in AZ826MIF for 20 min
	DI water rinse 90 sec + 90 sec
	Dry by N_2
	Inspection
19	***Parylene etching with RIE***
	In RIE (3 x 20 min)
	Inspection
20	***Dicing***
21	***PR strip***
	In acetone for 2 days

Fabrication flow of 2nd generation devices is presented in Table B.2.

Table B.2: Detailed fabrication flow of the 2nd generation devices.

	2nd generation devices fabrication flow
1	***Glass wafer (4")***
2	***Piranha (30 min) + BHF (2 min) cleaning***
3	***Dehydration at oven at 110°C for 20 min***
4	***Parylene coating***
	with silane
	4 g for 2 μm parylene thickness
5	***Dehydration at oven at 95°C for 40 min***
6	***Ti sputtering as adhesion layer (AJA-1)***
	600 W 270 sec 30 nm
7	***Au sputtering layer (AJA-1)***
	350 W 680 sec 400 nm
8	***Dehydration at oven at 95°C for 40 min***
9	***Lithography for electrode formation***
Mask 1	HDMS coating 500 rpm 15 sec + 4000 rpm 40 sec
	S220-3 spin 500 rpm 15 sec + 4000 rpm 40 sec
	Softbake @ 95°C for 2 min hotplate
	Expose UV for 5 sec (vacuum contact)
	Develop in MF24A for 60 sec
	DI water rinse 90 sec + 90 sec
	Dry by N_2
	Inspection
	Hardbake at oven @ 95°C for 40 min
	Desicator for 5 min
10	***Descum 3 min***
11	***Au etching***
	Aqua regia (600 ml HCl + 200 ml HNO_3) activation for 15 min

Table B.2 (continued).

	Preparation of aqua regia solution (by adding 800 ml DI water)
	Etching for 120 sec
	DI water rinse 3 cycles
	Dry by N_2
	Inspection
12	***Ti etching***
	Ti etchant (20 ml HF + 20 ml H_2O_2 + 1560 ml DI water)
	Etching for 25 sec
	DI water rinse 3 cycles
	Dry by N_2
	Inspection
13	***PR strip***
	In acetone for 60 min
	In IPA for 10 min
	DI water rinse 3 cycles
	Dry by N_2
	Inspection
14	***Parylene coating (as insulating layer)***
	without silane
	1 g for 0.5 μm parylene thickness
	Inspection
15	***Dehydration at oven at 95°C for 40 min***
16	***Lithography for microchannel formation***
Mask 2	HDMS coating 500 rpm 15 sec + 1000 rpm 30 sec
	AZ9260 spin 500 rpm 15 sec + 1000 rpm 30 sec (first layer)
	Edge bead removal
	Wait for 15 min
	Prebake @ 95°C for 3 min at hotplate

Table B.2 (continued).

	AZ9260 spin 500 rpm 15 sec + 1000 rpm 30 sec (second layer)
	Edge bead removal
	Wait for 15min
	Hardbake at oven from room temperature to 95°C and 50min @ 95°C
	Cooling at oven from 95°C to 70°C
	Rehydration (overnight)
	Expose UV for 40 sec (vacuum contact)
	Develop in AZ 826MIF for 12 min
	DI water rinse 90 sec + 90 sec
	Dry by N_2
	Inspection
	Expose UV for 40 sec (vacuum contact)
	Develop in AZ 826MIF for 15 min
	DI water rinse 90 sec + 90 sec
	Dry by N_2
	Inspection
17	***Microchannel thickness measurement (Dektak)***
18	***Parylene coating***
	without silane
	40 g for 20 μm parylene thickness
19	***Opening lithography***
Mask 3	HDMS coating 500 rpm 10 sec + 750 rpm 30 sec
	AZ9260 spin 500 rpm 10 sec + 750 rpm 30 sec (first layer)
	Edge bead removal
	Wait for 15 min
	Prebake @ 95°C for 3 min at hotplate
	AZ9260 spin 500 rpm 10 sec + 750 rpm 30 sec (second layer)
	Edge bead removal

Table B.2 (continued).

	Wait for 15min
	Hardbake at oven from room temperature to 95°C and 50min @ 95°C
	Cooling at oven from 95°C to 70°C
	Rehydration (overnight)
	Expose UV for 55 sec (vacuum contact)
	Develop in AZ 826MIF for 20 min
	DI water rinse 90 sec + 90 sec
	Dry by N_2
	Inspection
	Expose UV for 55 sec (vacuum contact)
	Develop in AZ 826MIF for 20 min
	DI water rinse 90 sec + 90 sec
	Dry by N_2
	Inspection
20	***Parylene etching with RIE***
	In RIE (3 x 20 min)
	Inspection
21	***Dicing***
22	***PR strip***
	Acetone for 2 days

Fabrication flow of 3rd generation devices is presented in Table B.3.

Table B.3: Detailed fabrication flow of the 3rd generation devices.

	3rd generation devices fabrication flow
1	***Glass wafer (6")***
2	***Piranha (30 min) + BHF (2 min) cleaning***
3	***Dehydration at oven at 110°C for 20 min***
6	***Ti sputtering as adhesion layer (30 nm) (Bestec-1)***
	300 W T_1:120 sec T_2:165 sec Flow:2.5 sccm
7	***Au sputtering layer (400 nm) (Bestec-1)***
	300 W T_1:120 sec T_2:440 sec Flow:6.2 sccm
8	***Dehydration at oven at 110°C for 30 min***
9	***Lithography for electrode formation***
Mask 1	HDMS coating 500 rpm 10 sec + 4000 rpm 40 sec
	S1813 spin 500 rpm 10 sec + 4000 rpm 40 sec
	Softbake @ 115°C for 90 sec at hotplate
	Expose UV for 4.5 sec (vacuum contact)
	Develop in MF24A for 60 sec
	DI water rinse 90 sec + 90 sec
	Dry by N_2
	Inspection
	Hardbake at oven @ 110°C for 40 min
	Desicator for 5 min
	Inspection
10	***Descum 3 min***
11	***Au etching***
	Aqua regia (1200 ml HCl + 400 ml HNO_3) activation for 15 min
	Preparation of aqua regia solution (by adding 2400 ml DI water)
	Etching for 120 sec
	DI water rinse 3 cycles

Table B.3 (continued).

	Dry by N_2
	Inspection
12	***Ti etching***
	Ti etchant (50 ml HF + 50 ml H_2O_2 + 3900 ml DI water)
	Etching for 27 sec
	DI water rinse 3 cycles
	Dry by N_2
	Inspection
13	***PR strip***
	In SVC-175 for 30 min
	DI water rinse 10 cycles
	Dry by N_2
	Inspection
14	***Parylene coating (as insulating layer)***
	with silane
	1 g for 0.5 μm parylene thickness
	Inspection
15	***Dehydration at oven at 95°C for 40 min***
16	***Lithography for microchannel formation***
Mask 2	HDMS coating 400 rpm 15 sec + 700 rpm 30 sec
	AZ9260 spin 400 rpm 15 sec + 700 rpm 30 sec
	Edge bead removal
	Wait for 15 min
	Prebake @ 95°C for 3 min at hotplate
	Hardbake at oven from room temperature to 95°C and 50min @ 95°C
	Cooling at oven from 95°C to 70°C
	Rehydration (overnight)
	Expose UV for 50 sec (vacuum contact)

Table B.3 (continued).

	Develop in AZ 826MIF for 15 min
	DI water rinse 90 sec + 90 sec
	Dry by N_2
	Inspection
17	***Microchannel thickness measurement (Dektak)***
18	***Parylene coating***
	without silane
	40 g for 20 μm parylene thickness
19	***Opening lithography***
Mask 3	HDMS coating 500 rpm 10 sec + 750 rpm 30 sec
	AZ9260 spin 500 rpm 10 sec + 750 rpm 30 sec (first layer)
	Edge bead removal
	Wait for 15 min
	Prebake @ 95°C for 3 min at hotplate
	AZ9260 spin 500 rpm 10 sec + 750 rpm 30 sec (second layer)
	Edge bead removal
	Wait for 15min
	Hardbake at oven from room temperature to 95°C and 50min @ 95°C
	Cooling at oven from 95°C to 70°C
	Rehydration (overnight)
	Expose UV for 55 sec (vacuum contact)
	Develop in AZ 826MIF for 20 min
	DI water rinse 90 sec + 90 sec
	Dry by N_2
	Inspection
	Expose UV for 55 sec (vacuum contact)
	Develop in AZ 826MIF for 20 min
	DI water rinse 90 sec + 90 sec

Table B.3 (continued).

	Dry by N_2
	Inspection
20	***Parylene etching with RIE***
	In RIE (3 x 20 min)
	Inspection
21	***Dicing***
22	***PR strip***
	Acetone for 4 days